

Technisch-
Wissenschaftlicher-
Bericht



Martina Schwarz

Influence of Hydrogen Gas Environment
on Fatigue Short Crack Growth in
Austenitic and Martensitic Stainless Steel

**Influence of Hydrogen Gas Environment
on Fatigue Short Crack Growth in
Austenitic and Martensitic Stainless Steel**

vorgelegt von
M.Sc. Martina Schwarz
aus Stuttgart

Technisch-Wissenschaftlicher-Bericht

Band: 2022/02

Schwarz, Martina:

Influence of Hydrogen Gas Environment on Fatigue Short Crack Growth
in Austenitic and Martensitic Stainless Steel

Herausgeber:

© Materialprüfungsanstalt (MPA) Universität Stuttgart

Pfaffenwaldring 32

70569 Stuttgart

Internet: <http://www.mpa.uni-stuttgart.de>

Influence of Hydrogen Gas Environment on Fatigue Short Crack Growth in Austenitic and Martensitic Stainless Steel

Von der Fakultät Energie-, Verfahrens- und Biotechnik

der Universität Stuttgart

zur Erlangung der Würde eines Doktors

der Ingenieurwissenschaften (Dr.-Ing.) genehmigte Abhandlung

Vorgelegt von

Martina Manuela Schwarz

aus Stuttgart

Hauptberichter: Prof. Dr.-Ing. Stefan Weihe

Mitberichter: Prof. Dr. techn. Bernhard Sonderegger

Tag der mündlichen Prüfung: 15.09.2021

Materialprüfungsanstalt (MPA) Universität Stuttgart

2022


Declaration of Authorship

I hereby certify that the dissertation entitled

Influence of Hydrogen Gas Environment on the Short Crack Growth in Austenitic and Martensitic Stainless Steels

is entirely my own work except where otherwise indicated. Passages and ideas from other sources have been clearly quoted.

Name: Martina Schwarz

Date, Signature: 06.04.2021, 

Acknowledgments

The author acknowledges the support of Prof. Dr.-Ing. Stefan Weihe head of the Materials Testing Institute at the University of Stuttgart as well as Prof. Dr. techn. Bernhard Sonderegger at the Institute for metallic construction materials, University of Linz, for being part of the defense committee.

A special thanks to my supervisor and mentor Stefan Zickler and to my former and recent team members Arnd Nitschke, Erich Sattler, Chris Kohler, Dr. Karl Berreth, Werner Ottens, and Rolf Hahn of the hydrogen group at MPA. The help of the technologist Sebastian Hammer was highly appreciated for conducting some of the very time-consuming fatigue tests. In terms of microstructural discussions Dr. Magdalena Speicher, Dr. Ewa Soppa, and Dr. Christopher Kohler were always very supportive. Without the microscopy team around Rudi Scheck and the machine shop at MPA not a single specimen could have been tested. For analyzing the cracks, I would like to thank Dieter Willer operating the SEM several hours for me.

In the first years my way was accompanied by two other PhD candidates Sven Brück and Holger Schippl at the University of Siegen who worked on the same project. I highly acknowledge the lively discussions we had and their friendly hospitality each time I visited them. Georg Schauer was always supportive and open for fundamental thoughts and ideas to investigate the effects of hydrogen.

Outside of MPA I got to know many researchers working on the great desire to better understand the effects of hydrogen on materials every day and generously shared their hydrogen experience: Dr.-Ing. Thorsten Michler, Jörg Naumann, Dr. Christopher San Marchi, Prof. Junichiro Yamabe, and Prof. Hisao Matsunaga. When it came to discussions about hydrogen test systems Brendan Davis always lent me his ear.

I also would like to thank my student assistants Stefan Esser, Marc Straubinger and Yannick Frey for primarily performing studies to evaluate new test methodologies.

Finally, major thanks to my family, especially my parents, and my friends. Last but not least I acknowledge the endless patience, the valuable support, and the motivating words of my boyfriend Brian Kagay.

This research was partly funded by the Deutsche Forschungsgemeinschaft (DFG, German Research Foundation) and the Forschungsvereinigung Verbrennungskraftmaschinen e.V. (FVV, Research Association for Combustion Engines eV).

Content

Acknowledgments.....	I
Content	III
List of abbreviations.....	VII
Abstract	XI
Zusammenfassung.....	XIII
1 Introduction	1
2 Background	5
2.1 Physical metallurgy of stainless steel	5
2.1.1 Austenitic stainless steel	5
2.1.2 Martensitic stainless steel	9
2.2 Hydrogen adsorption and diffusivity in steel.....	11
2.3 Hydrogen-assisted cracking mechanisms	14
2.3.1 Hydrogen enhanced decohesion (HEDE)	14
2.3.2 Hydrogen enhanced localized plasticity (HELP)	15
2.3.3 Adsorption-induced dislocation-emission (AIDE).....	15
2.4 Fatigue cracking	15
2.5 Fatigue cracking of austenitic stainless steel under hydrogen influence.....	18
2.6 Fatigue cracking of martensitic stainless steel under hydrogen influence	19
3 Scientific challenge and approach.....	21
4 Characterization of materials	25
4.1 Metastable austenitic stainless steel X2CrNi19-12 ($\approx 1.4306 \approx \text{AISI304L}$)	25
4.2 Martensitic stainless steel X3CrNiMo13-4 (1.4313 $\approx \text{AISI415}$).....	27

5	Experimental procedure	29
5.1	Sample geometry	29
5.2	Specimen extraction from the austenitic stainless steel.....	30
5.3	Specimen extraction from the martensitic stainless steel	31
5.4	Test System	31
5.5	Test method.....	32
5.6	Replica	33
5.7	Direct current potential drop method	34
5.8	Microstructural analysis techniques	35
6	Results and discussion.....	39
6.1	Results Austenitic stainless steel (X2CrNi19-12)	39
6.1.1	Influence of hydrogen on the fatigue short crack sites	39
6.1.2	Crack initiation sites and microstructurally short cracks in austenitic stainless steel under hydrogen influence	45
6.1.3	Strain-induced martensite formation	56
6.1.4	Fractography of austenitic stainless steel	57
6.2	Discussion austenitic stainless steel (X2CrNi19-12)	59
6.3	Results martensitic stainless steel (X3CrNiMo13-4)	63
6.3.1	The influence of hydrogen on the fatigue short crack sites in martensitic stainless steel	63
6.3.2	Crack initiation sites and microstructurally short cracks in martensitic stainless steel under hydrogen influence	69
6.3.3	Fractography of martensitic stainless steel.....	70
6.4	Discussion martensitic stainless steel (X3CrNiMo13-4)	73

7	Summary.....	81
8	Outlook	83
	Appendix.....	85
A1	Tensile curves of the investigated materials.....	85
A2	Tension-tension fatigue properties X2CrNi19-12 of notched specimen	86
A3	Strain softening behavior of the austenitic stainless steel X2CrNi19-12	86
A4	Electric potential of austenitic stainless steel.....	87
A5	Electric potential of the martensitic stainless steel	88
A6	Fractions of classified martensite grain boundaries.....	89
	References	91
	Curriculum vitae	102

List of abbreviations

Abbreviation	Meaning
a_s	Direct crack length between crack tips
a_w	Effective crack length with tortuosity
bcc	Body-centered cubic
C_0	Equilibrium lattice hydrogen concentration
CSL	Coincidence site lattice
D	Diffusion coefficient
DCPD	Direct current potential drop
d	Half the grain size
d_0	Specimen diameter
d_r	Specimen diameter reduced
EBS	Electron backscattered diffraction
E_l	Total Elongation
fcc	Face-centered cubic
f_{dim}	Fractal dimension
G	Shear modulus
HEDE	Hydrogen Enhanced Decohesion
HELP	Hydrogen Enhanced Localized Plasticity
IB	Inter-block boundary crack
IP	Inter-packet boundary crack
IPAG	Inter-prior austenite grain boundary crack

IPF	Inverse Pole Figure
K-S	Kurdjumov-Sachs Relationship
LCF	Low Cycle Fatigue
b	Burgers vector
m	Schmid factor
n	Number of dislocations
N-W	Nishiyama-Wassermann Relationship
P	Gas pressure
PAG	Prior Austenite Grain
RA	Reduction of Area
RRA	Relative Reduction of Area
S	Solubility
SCGI	Short Crack Growth Stage I
SCGII	Short Crack Growth Stage II
SEM	Scanning electron microscope
TB	Trans-block crack
UTS	Ultimate Tensile Strength
YS	Yield Strength
γ_s	Work to make new fracture surface
λ	Angle between the tensile direction and the slip direction
Σ	Reciprocal coincidence site lattice density
τ_c	Critical resolved shear stress
τ_i	Friction shear stress

List of abbreviations

τ_N

Shear stress

ϕ

Angle between the plane normal and the
tensile direction

Abstract

In this study the influence of hydrogen on fatigue short crack behavior in the austenitic stainless steel X2CrNi19-12 and the martensitic stainless steel X3CrNiMo13-4 is evaluated. The microstructural sites for fatigue short crack initiation and propagation in a 10 MPa hydrogen gas atmosphere were compared to those in a 10 MPa helium gas atmosphere. Tension-compression fatigue tests were performed with smooth and electropolished specimen at room temperature and a test frequency of 1 Hz. The specimens were flattened on two opposite sides to enable electron back-scattered diffraction (EBSD) analysis of the fatigue short cracks on the specimen surface.

In the hydrogen gas atmosphere, the fraction of intergranular and transgranular short crack propagation in the austenitic stainless steel shows no significant difference to testing in helium gas. However, in both atmospheres 30 % more crack length was observed along $\Sigma 3$ twin boundaries compared to the bulk microstructure. In addition, the strain-induced α' -martensite was qualitatively compared for short cracks developed in hydrogen versus helium gas atmosphere.

In the case of the martensitic stainless steel the majority of short cracks propagate on prior austenite grain boundaries in hydrogen, whereas in helium short cracks predominately propagate along high misorientation angle ($>47^\circ$) block and packet boundaries. The hydrogen short cracks initiated at prior austenite grain boundaries predominately perpendicular to the tensile stress. The helium short cracks initiated along planes aligned with the maximum shear stress. The short cracks produced in hydrogen gas exhibited a smaller fractal dimension than the short cracks produced in helium gas.

For both materials testing in hydrogen gas atmosphere lead to a significantly smaller amount of initiated fatigue short cracks per specimen than in helium.

Zusammenfassung

Im Rahmen dieser Arbeit wurde das Initiierungsverhalten und das Wachstum von Kurzrissen in Edelstählen unter Einfluss von Druckwasserstoff untersucht. Es wurden zwei Edelstähle mit verschiedenen Mikrostrukturen analysiert: Der metastabile Austenit X2CrNi19-12 und der Weichmartensit X3CrNiMo13-4. Die glatten und elektropolierten Rundproben wurden mittels rein wechselnder Ermüdungsversuche in 10 MPa Wasserstoffatmosphäre bei Raumtemperatur und einer Prüffrequenz von 1 Hz geprüft. Um EBSD-Untersuchungen zu ermöglichen, waren die Proben auf zwei gegenüberliegenden Seiten mit planen Flächen versehen.

Der austenitische Edelstahl zeigt keinen signifikanten Unterschied weder im Falle von interkristallinen und transkristallinen Risslängenanteilen noch bei den beobachteten Initiierungsstellen im Vergleich von Wasserstoff zum Referenzmedium Helium. Jedoch ist für Ermüdungskurzrisse ein höherer Anteil (30 %) an interkristallinem Risswachstum entlang der $\Sigma 3$ Zwillingskorngrenzen zu verzeichnen als im Vergleich zur Ausgangsmikrostruktur. Eine qualitative Analyse der verformungsinduzierten Austenitumwandlung zu Martensit ergibt ebenfalls keinen eindeutigen Einfluß des Wasserstoffs.

Im Falle des martensitischen Edelstahl verlaufen die Kurzrisse, welche in Wasserstoff entstanden sind, zu einem Anteil von mehr als 40 % entlang ehemaliger Austenitkorngrenzen. Die Ermüdungskurzrisse, welche in Helium generiert wurden, verlaufen vorwiegend entlang von Korngrenzen mit hohen Misorientierungswinkeln (47° - 60° , Block- und Paketgrenzen mit großem Misorientierungswinkel). Die Wasserstoffkurzrisse initiieren senkrecht zur Hauptnormalspannungsrichtung, die Heliumkurzrisse wiederum initiieren in einer Ebene parallel zur maximalen Schubspannung.

Bei beiden Werkstoffen ist die Anzahl der initiierten Kurzrisse in Helium um ein Vielfaches größer als in Wasserstoffatmosphäre.

1 Introduction

Our planet earth is a unique and rather vulnerable place to live. Records of average temperatures all over the earth show a clear upwards trend with negative effects on all living creatures. One of the main reasons for this climate change is the increasing intensity of greenhouse gas emissions by human beings since the industrial revolution in the late eighteen hundreds. After an immense strengthening of environmental awareness in society based on broad scientific knowledge the leading heads of many industrial countries assembled in Japan in 1997 to sign the Kyoto protocol, a contract for climate protection by limiting greenhouse emissions. To reconcile a booming economy with limited emissions renewable energy technologies are a promising way forward.

Wind, water, and sunlight can be used to generate electrical energy in a rather environmentally-friendly manner compared to nuclear and coal-fired power plants. As these are all natural sources which are subject to variabilities throughout a day and since the energy demand itself varies, there is a great need to efficiently store the generated energy. One possible medium to store excess electrical energy is hydrogen. At 77 % the efficiency factor for the conversion process from electrical energy to hydrogen is 8 % higher compared to other media such as methane [1]. The hydrogen can directly be used at any time in a fuel cell to produce electric power, for example to run a vehicle. The emission released out of the exhaust pipe is water vapor containing no CO₂ or any other greenhouse gas. Compared to battery electric vehicles all components can be recycled easily. Not limited to transportation applications, hydrogen is a multipurpose fuel that can also be utilized to provide houses with warmth and electricity as demonstrated in Japan where more than 300,000 so-called ene-farms/houses have been deployed as of 2019 [2].

Despite enormous potential as an environmentally friendly energy source, there are two physical challenges that accompany the implementation of hydrogen as a fuel source:

the degrading effect of hydrogen on materials, especially metals and the explosive nature of hydrogen under certain circumstances. Many people have experienced the oxyhydrogen test in school chemistry and therefore know that an oxygen-hydrogen mixture lit by fire may explode. However, this risk is manageable by applying high safety standards for single components, such as valves, and thoughtfully organized structures in terms of redundancy. Regarding the fact that the gasoline we use today is inflammable and also explosive under certain circumstances, the usage of hydrogen as an energy source is definitely feasible. The degrading effect hydrogen has on metals – often referred to as hydrogen embrittlement – must be carefully considered when designing components in contact with hydrogen; if not, early and/or unexpected failures may occur.

Although hydrogen embrittlement has been known for more than 100 years, it is not completely understood. A significant loss in ductility and a reduction of the fatigue performance are the main effects which vary by the material class and the test parameters such as gas pressure, strain rate and temperature. Generally, stainless steels having good ductile properties are favorable for tubing, valves, fasteners, and other smaller components. Gas storage vessels are also usually made out of ductile steels to prevent a sudden failure by fulfilling the leak before fracture concept. Consequently, especially austenitic steels are in focus to be used for hydrogen gas service. Furthermore, the material properties of austenitic stainless steels are normally influenced by hydrogen compared to other material classes such as ferritic steels. Nevertheless, requirements for high strength or magnetizability cannot be satisfied by austenitic stainless steels. Therefore, the material performance of conventional austenitic stainless steels, as well as martensitic stainless steels in contact with hydrogen is of great interest. Understanding of the effect of hydrogen on fatigue crack initiation and propagation is necessary to improve the fatigue performance and to estimate the life-time of metal components in hydrogen environments.

The purpose of this study is to analyze the short fatigue crack behavior of the austenitic stainless steel X2CrNi19-12 and the martensitic stainless steel X3CrNiMo13-4 in a hydrogen gas environment from a metallurgical perspective.

2 Background

2.1 Physical metallurgy of stainless steel

Steels with a high chromium content are referred to as stainless steels. A high chromium content (> 12 wt%) leads to a significant improvement of the corrosion resistance. Stainless steels can be austenitic or martensitic based on their composition and processing. In the following sections, the microstructural characteristics of austenitic and martensitic stainless steels, as well as mechanical behavior, are discussed.

2.1.1 Austenitic stainless steel

Austenitic stainless steel primarily consists of γ -iron with a face-centered cubic (fcc) lattice structure. Austenitic stainless steels for hydrogen applications are normally used in an annealed or strain-hardened polycrystalline form.

The area between two grains – the grain boundary - can be characterized by the misorientation between the two adjacent grains. It is common to use the smallest rotation angle that would cause the coordinate system of one grain to correspond with the coordinate system of the adjacent grain as a characterizing value. Additionally, comparing the lattice orientation of two grains by laying them on top of one another may reveal that some of the atoms are in concordance regarding their place in both lattices, which is called a coincidence site lattice (CSL). A CSL grain boundary can be designated by the reciprocal of the fraction of atoms that are in alignment. For example, if $1/5$ of the atoms align, then the boundary between the two grains is defined as a CSL $\Sigma 5$ boundary.

Grain boundaries are commonly grouped into low-angle and high-angle boundaries with a threshold value of 15° . Low angle boundaries have a lower interfacial energy than high angle boundaries. Additionally, most random high angle boundaries above 15° in a given material have similar interfacial energies as illustrated in Figure 2.1.1a) [3]. In austenitic stainless steels a special form of a grain boundary is a twin boundary. Twin boundaries

have a misorientation angle of 60° about a $\{111\}$ plane and a CSL of $\Sigma 3$. Despite the high misorientation angle $\Sigma 3$ twin boundaries are low energy boundaries, see Figure 2.1.1b). [3,4] In general, there are coherent and incoherent twin boundaries. Coherent twin boundaries have no angle between the boundary and the twinning plane. For incoherent twin boundaries there is a misorientation between the boundary plane and the twinning plane that is accommodated by dislocations. Incoherent twin boundaries have a higher boundary energy than coherent twin boundaries due to the presence of dislocations. In type 304 stainless steel the measured boundary energy for a coherent twin boundary is 19 mJ/m^2 , for an incoherent twin boundary it is 209 mJ/m^2 , and for a high angle grain boundary it is 835 mJ/m^2 . [5] The interfacial energy of the grain boundary can result in a higher concentration of solute atoms at the grain boundary compared to the interior of the grains. A higher concentration of solute atoms may also be present at grain boundaries with a higher interfacial energy. [3]

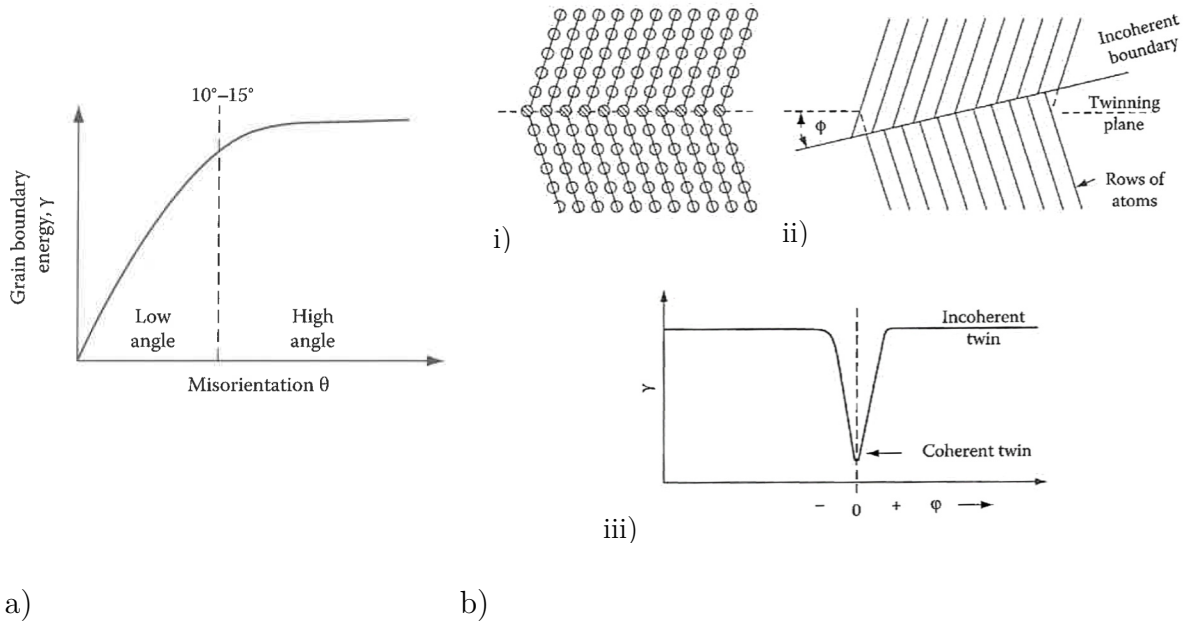


Figure 2.1.1: Grain boundary energies [3] a) low and high angle boundaries b) $\Sigma 3$ twin boundary, i) coherent twin boundary, ii) incoherent twin boundary, iii) energies of coherent and incoherent twin boundaries

To understand the deformation processes in an austenitic steel we look at a single crystal for simplification. There are 4 $\{111\}$ slip planes with 3 $[110]$ slip directions leading to 12 possible slip systems in the austenitic fcc lattice. Slip will occur when the resolved shear stress on a slip plane in one of the possible slip directions reaches a critical value. This transition is called Schmid's law. A value to characterize a grain in terms of the likelihood of dislocation slip due to an applied tensile stress is the Schmid factor m . It is the ratio of the critical resolved shear stress τ_c to the axial stress σ : The Schmid factor m , is a function of ϕ , the angle between the normal slip plane, and λ , the tension direction and the angle between the tensile direction and the slip direction.

$$\tau_N = m\sigma \tag{1}$$

$$m = \cos \phi \cos \lambda \tag{2}$$

ϕ – angle between the normal and the tension direction

λ – angle between the tension and the slip direction

From a mathematical point of view the Schmid factor can only be in the range of 0 to 0.5. [6] The crystallographic orientation of a grain in respect to the tensile axis determines the maximum Schmid factor and therefore the maximum local shear stress of the grain, see Figure 2.2. In terms of crack initiation and short crack growth the local shear stress is a significant value as described in chapter 2.4. The Schmid factor is used for an isostress condition. Assuming an isostrain condition in a polycrystalline material the Taylor factor is applied [7].

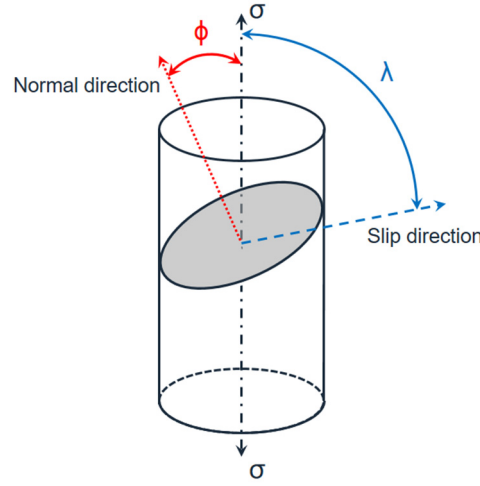


Figure 2.1.2: Schmid factor determination

In general, the austenite phase is thermodynamically unstable at room temperature which is shown in the equilibrium diagram. The austenitic stainless steel investigated here is so-called metastable. The more stable an austenite is the greater deformation is necessary to form strain-induced α' -martensite. Strain-induced martensite is formed at the intersection of deformation bands. The formation causes a volume increase which can lead to a local stress increase. Chemical elements like nickel and manganese improve the austenite stability [8].

A way to quantify this characteristic is the Md30-temperature. The Md30-temperature is defined as the temperature at which 50 % of the microstructure is transformed into martensite by a true tensile strain of 0.3, and is determined by the Angel's equation [9].

$$Md30 = 413 - 462(wt\%C + \%N) - 9.2(wt\%Si) - 8.1(wt\%Mn) - 13.7(wt\%Cr) - 20(wt\%Ni) - 18.5(wt\%Mo) \quad (3)$$

Another value to characterize austenitic stainless steels is the nickel equivalent, which is commonly used in Japan. The nickel equivalent is calculated as follows [10]:

$$Ni_{Eq} = 12.6 wt\%C + 0.35 wt\%Si + 1.05 wt\%Mn + wt\%Ni + 0.65 wt\%Cr + 0.98 wt\%Mo \quad (4)$$

2.1.2 Martensitic stainless steel

Martensite also referred to as α -iron has a body-centered cubic (bcc) lattice and possesses 12 possible slip systems from 6 $\{110\}$ slip planes with 2 possible $[111]$ slip directions each.

Martensite is formed from austenite through a displacive, diffusionless, shear-type phase transformation during rapid cooling of steel. The schematic in Figure 2.1.3 illustrates the physical appearance of lath martensite. Prior austenite grains (PAG) are composed of packets, which are composed of blocks, which are composed of laths. In a PAG, there are several packets but no more than three possible variants each with a different $\langle 111 \rangle$ plane applying the K-S relationship. The packets themselves consist of several blocks with the same habit plane based on six possible variants within each packet. These three classifications (prior austenite grain, packet, and block) can be identified by the misorientation angles of their boundaries. Lath boundaries are the smallest martensite features with a misorientation angle in the range of 1° to 10° . In general, carbon content strongly affects the prior austenite grain size and therefore the packet and block size, which as a whole has an influence on the material strength and toughness [11,12].

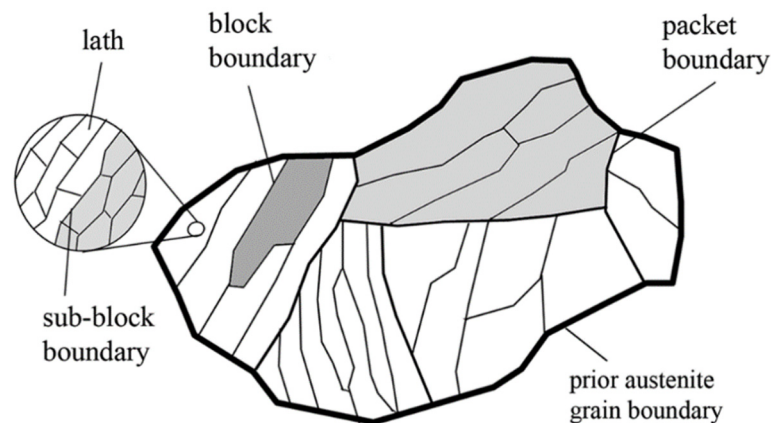


Figure 2.1.3: Typical crystallographic structure of lath martensite consisting of packets, blocks, and laths [13]

The physical appearance described above is based on the martensite transformation process out of the austenite phase. During the austenite to martensite transformation,

the austenite and martensite phases exhibit an orientation relationship and habit plane, which are commonly described by three models in the literature: The Bain distortion [14], the Kurdjumov-Sachs relationship (K-S) [15], and the Nishiyama-Wassermann relationship (N-W) [16]. The Bain distortion is the simplest model but is rarely found in nature. Martensite with a greater amount of alloying elements and at a lower transformation temperature is more likely to form with the N-W relationship [17]. The K-S relationship with its 24 variants is often applied for martensite with low carbon content, and the N-W with its 12 variants is more prevalent for martensite with a higher carbon content. In nature, there seems to be no distinct threshold carbon value as for a single 11 % Cr-steel, blocks of both orientation relationships could be observed. This means that there can be misorientations between blocks resulting from K-S/N-W, N-W/N-W, and K-S/K-S block pairs [18].

Figure 5.8.1 shows a classification of the boundaries in lath martensite based on the boundary misorientation angle. The scale begins at 2° because this is a commonly used threshold value to clean dataset measured with EBSD. Due to the cubic crystal symmetry the maximum achievable misorientation angle is 62° [19]. According to the literature [20] the lath boundaries are in the range from 0° to 10° . The packet boundaries are between 10° to 21° and 47° to 57° , and block boundaries are greater than 50° . In the case of the PAG boundaries there is no specific range over which they occur so PAG boundaries can exhibit any misorientation between 0° and 62° . However, based on the transformation relationships K-S and N-W which determine lath, packet, and block boundaries there is a gap between 21° and 47° in which no lath, packet or block boundaries exist. This means that all measured misorientations in that range are confidently PAG boundaries.

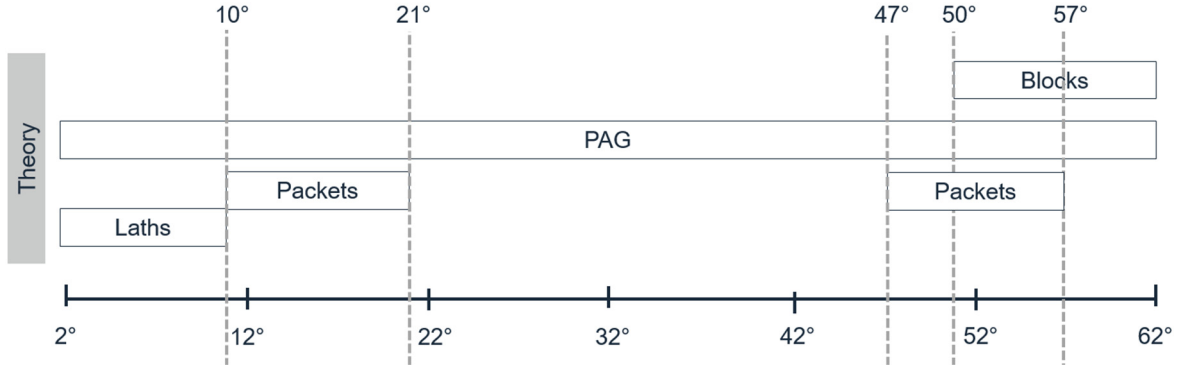


Figure 2.1.4: Classification of boundaries in lath martensite according to the boundary misorientation angle based on [20]

2.2 Hydrogen adsorption and diffusivity in steel

Hydrogen, atomic number one, is the smallest known atom with one proton and one electron. As it is small in size hydrogen can be accommodated in interstitial lattice sites and can diffuse rather rapidly through the lattice of steels even at room temperature. In general, hydrogen can enter a material in two ways: through gas phase or liquid phase. Because only hydrogen entry from the gas phase is relevant for the studies in this thesis, the latter will not be described here.

The basic principles of hydrogen solubility follow Sievert's law. The equilibrium lattice hydrogen concentration C_0 is calculated by the solubility S and the hydrogen gas pressure P .

$$C_0 = SP^{1/2} \quad (5)$$

In the absence of O_2 -molecules and/or other atoms and molecules with a greater metal affinity than hydrogen, hydrogen can be either physically adsorbed as a molecule by Van-der-Waals-forces or dissociatively chemically adsorbed as an atom on the solid metal surface [21,22]. The adsorption mostly reaches the first three to four atom layers of a free surface and results in a high hydrogen concentration directly on the surface. The two main driving forces for adsorption are the gas pressure and the temperature.

The higher the gas pressure and the lower the temperature, the greater is the hydrogen adsorption capacity [22]. After hydrogen is adsorbed on the surface it diffuses deeper into the material.

Within the lattice the solute hydrogen atoms can agglomerate in traps. Traps are classified according to their potential energy as reversible (<30 kJ/mol) or irreversible (>50 kJ/mol) [23]. The potential energy is the activation energy needed to release the atoms from the traps and return them to their mobile solute state.

Figure 2.2.1 gives an overview of possible hydrogen sites in a metal lattice [24]. In this figure, a)-c) are interstitial sites which have a low binding energy and are therefore considered reversible. In cases b) and c) the hydrogen atoms are located on the surface and close to the surface, respectively. Sites d)-f) are lattice defects with a greater binding energy and therefore are considered irreversible. In case d) the hydrogen is agglomerated at a grain boundary. Sites e) and f) are a dislocation and vacancy, respectively. In irreversible traps hydrogen can recombine to form a molecule.

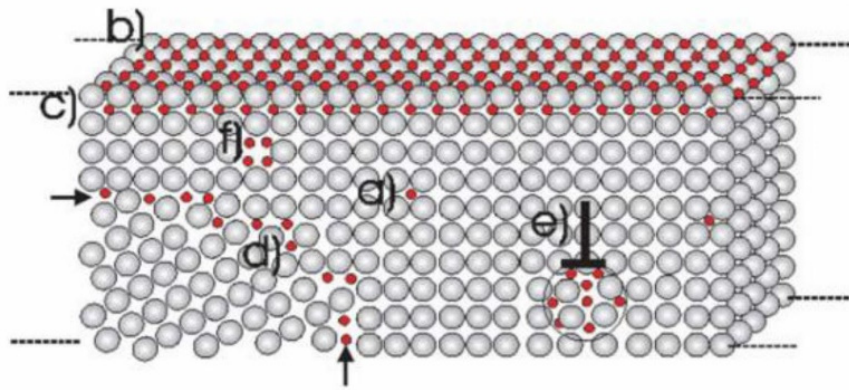


Figure 2.2.1: Hydrogen adsorption and trapping sites a) interstitial, b) on the surface, c) close to the surface, and in irreversible traps: d) grain boundaries, e) dislocations, f) vacancies [24]

A schematic illustration of reversible and irreversible traps with their associated potential energy is shown in Figure 2.2.2 [25]. Interstitial sites have the smallest activation energy E_a required to release the atoms. Other reversible trap sites have an activation

energy E_t , which is the sum of E_a and the binding energy E_b . E_t for reversible trap sites is comparably small to the activation energy, but E_I of irreversible trap sites is much greater than the activation energy due to the greater binding energy of irreversible trap sites.

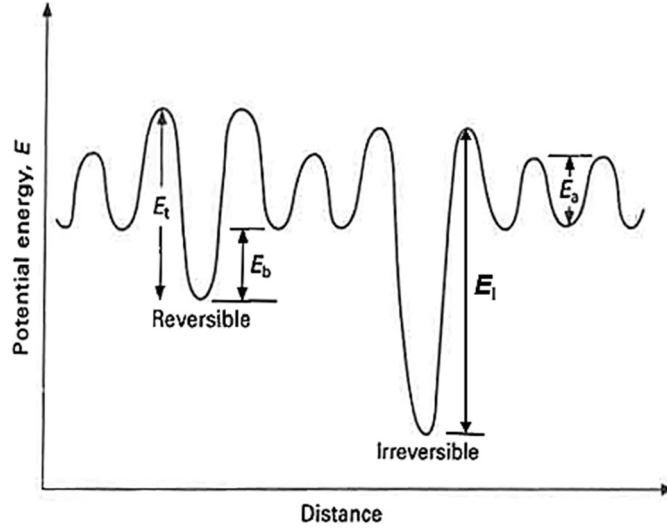


Figure 2.2.2: Schematic illustration of the potential energy associated with interstitial diffusion sites with activation energy E_a , reversible trap sites with binding energy E_b and activation energy E_t , and irreversible traps with a activation energy of E_I , [25] modified

Hydrogen diffusion in metals closely follows Fick's first law. As a result of the high binding energy in the irreversible traps only interstitial hydrogen readily diffuses in the material at room temperature. Generally, diffusivity is dependent on the temperature and the material's crystallographic structure. In Table 2.1 the diffusion coefficients of different types of steels are listed to show the variation with microstructure. The diffusion coefficient D at room temperature, is several orders of magnitude higher in martensite than in austenite due to the close packed fcc structure of austenite. In contrast to the diffusivity is the solubility. Fcc steels have a significantly greater amount of interstitial sites compared to bcc lattice [26], which is why hydrogen solubility is higher in fcc materials.

Table 2.1: Diffusion Coefficients of Hydrogen in Various Types of Steels

Material	Diffusion coefficient D at RT [cm ² /s]	Reference
Pure α -iron	7.5×10^{-5}	[27]
Carbon steel	2.5×10^{-6}	[28]
Ferritic stainless steel	10^{-7}	[29]
Martensitic stainless steel	2×10^{-9}	[30]
Austenitic stainless steel	2.15×10^{-12}	[31]

2.3 Hydrogen-assisted cracking mechanisms

In order to explain the effects of hydrogen inside materials several mechanisms have been proposed in the last few decades. This chapter gives an overview of the most common mechanisms stated in literature and previously well-reviewed by Lynch [32].

Most relevant for the steels investigated here are the hydrogen enhanced decohesion (HEDE), the hydrogen enhanced localized plasticity (HELP), and the adsorption-induced dislocation-emission (AIDE) mechanisms. Each mechanism is capable of explaining one significant effect of hydrogen, but no mechanism has proven sufficient to describe the complexity of the hydrogen influence for bcc or fcc metals. For austenitic stainless steels HELP and AIDE may be more relevant because the effects of hydrogen on dislocation motion may be more severe for materials with more planar slip, whereas in the case of martensitic steels with wavier slip, HEDE might be the more applicable mechanism. [32]

2.3.1 Hydrogen enhanced decohesion (HEDE)

According to the HEDE mechanism, which was proposed by Troiano [33] and further developed by Oriani [34], the binding energy between iron atoms is reduced by the presence of solute hydrogen atoms. The hydrogen itself stays interstitial in the lattice as an H⁺ ion, but the electrons of the hydrogen atoms enter the 3d shell of the iron atoms. The increased electron density then causes an increase of the repulsive force

between the iron atoms. The weakening of interatomic bonds causes tensile separation to become more favorable than dislocation slip.

2.3.2 Hydrogen enhanced localized plasticity (HELP)

The idea of the HELP mechanism was first partly described by Beachem [35] and afterwards promoted by Birnbaum, Sofronis, [36], and Robertson [37] and was based on *in situ* TEM (transmission electron microscopy) observation showing a significant effect of hydrogen on dislocation movement. The applied force during *in situ* tensile testing in a TEM was decreased such that the dislocations simply stopped moving. Subsequently, by adding hydrogen in the TEM chamber the dislocations started moving again [36,37]. This mechanism states that the embrittlement is caused by hydrogen facilitating dislocation movement due to a reduction of the repulsive forces between dislocations at obstacles. Hydrogen is agglomerated in areas with high hydrostatic stresses and at crack tips such that the deformation is localized and crack propagation is facilitated.

2.3.3 Adsorption-induced dislocation-emission (AIDE)

The AIDE mechanism, proposed by Lynch [38], is based on the idea that the dislocation nucleation and movement is facilitated by adsorbed hydrogen. The adsorption of hydrogen promotes the formation of dislocation cores by shearing of planes of atoms which includes breaking and re-forming of interatomic bonds. After facilitated nucleation of dislocations at the crack tip, the dislocations move away from the crack tip to areas in the plastic zone forming nanoscale voids. The actual crack propagation encompasses microvoid-coalescence and cracking due to dislocation emission on slip planes at the crack tip.

2.4 Fatigue cracking

Fatigue is the cyclic application of a load leading to material damage, cracking, and eventually failure. Fatigue cracking in regard to the microstructure is specified as intergranular (between two grains following a grain boundary) or transgranular (across a

grain). The fatigue failure process can be divided into 3 sections: crack initiation, short crack growth, and long crack growth.

In the Low-Cycle Fatigue (LCF) regime cracks initiate almost exclusively at the surface of a component [39]. Application of a fatigue stress causes irreversible plastic deformations which are localized in slip bands. Intrusion and extrusions may eventually form at the intersection of the slip bands and the free surface. Then, one of these intrusions or extrusions may lead to material cleavage and the formation of a crack.

After a crack has nucleated, the subsequent crack propagation can be classified in three categories based on crack length as shown in Figure 2.4.1. [40,41]

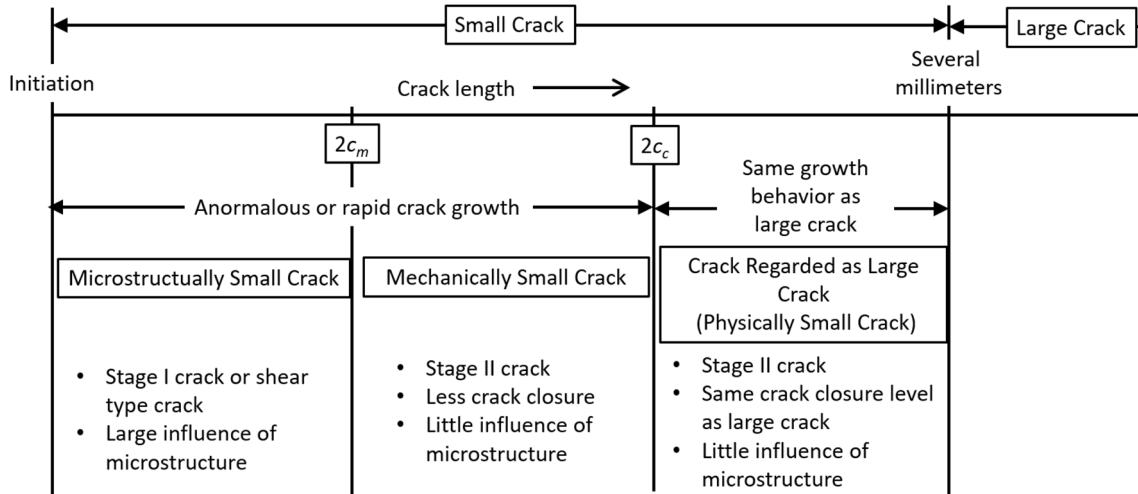


Figure 2.4.1: Three regimes of small fatigue cracks and their corresponding mechanisms and characteristics [40]

The three categories in this approach are microstructurally small cracks (MSSC), mechanically small cracks, and physically small cracks. Sometimes, the three short crack regimes are also grouped as short crack growth stage I (microstructurally small cracks) and short crack growth stage II (mechanically and physically small cracks). $2c_m$ is the transition from microstructurally to mechanically small cracks, whereas $2c_c$ is the transition to physically small cracks. Fatigue cracks with a crack length related to the scale

of the characteristic microstructural dimension such as the grain size are called microstructurally short cracks. In this stage crack propagation is dominated by the global shear stress, which is 45° to the load axis, and leads to crack growth along a favorable slip plane. In fcc materials fatigue crack initiation and the growth of microstructurally short cracks is dependent on the Schmid factor. More information on the Schmid factor is provided in chapter 2.1.1. Mechanically small cracks are fatigue cracks such that the near-tip plasticity is comparable to the crack length or such that the crack is engulfed by the plastic strain field of a notch. The crack path morphology changes and crack growth becomes perpendicular to the load axis and the maximum tensile stress. The crack growth in both stages (microstructural and mechanically short cracks) is highly influenced by crystallographic obstacles such as precipitates or grain boundaries. When a fatigue crack is larger than the scale of local plasticity but smaller than a millimeter or two, it is called physically small.

Figure 2.4.2 illustrates the crack growth rate depending on the crack length. When a crack is long enough or more precisely when the threshold of the stress intensity factor is reached it follows the linear elastic fracture mechanics law of Paris-Erdogan and then is referred to as a long crack. [40,41]

The transition between microstructurally and mechanically small fatigue cracks is dependent on both material properties and testing parameters such as crystallographic structure, grain size, load ratio and the specimen geometry itself. For steels Tokaji and Ogawa observed threshold values $2c_m$ in a range of 45 to 440 μm for testing at a load ratio of $R=-1$ [40].

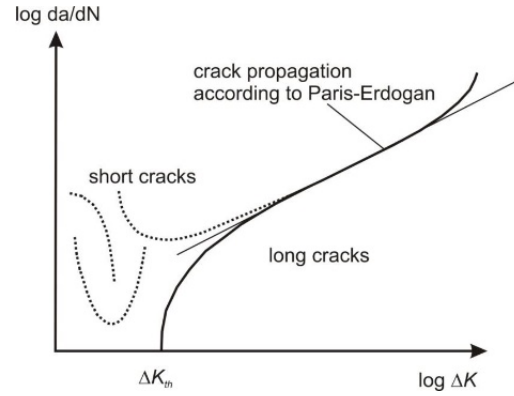


Figure 2.4.2: Short cracks and their crack growth rate [42]

In this thesis the term “short crack” refers to microstructurally and mechanically small cracks. Otherwise, the designations of Figure 2.4.2 will be used.

In general, the fatigue life consists of two main stages: number of cycles to initiate a crack and number of cycles to grow the crack until the final failure occurs due to ductile overload at the very end of the component life-time.

2.5 Fatigue cracking of austenitic stainless steel under hydrogen influence

Much research has been conducted on the fatigue properties of austenitic stainless steel with external and internal hydrogen. This section focuses only on results from fatigue cracking at room temperature. In general, hydrogen reduces fatigue life significantly; therefore, the crack initiation and/or propagation must be influenced by hydrogen. Since crack initiation and short crack propagation is about 80-90 % of the life-time [43], there is a major need to investigate the cracking behavior in regard to short crack propagation. Most investigations on the crack growth rate and the crack path morphology have been performed by the group of Murakami, Matsunaga and Yamabe using artificial notches or indentation, such as blind holes, which function as crack initiation sites. A few studies deal with the comparison of fatigue cracking with and without internal hydrogen [44–46]. In all those studies, an accelerated short crack growth was observed with internal hydrogen. The total number of slip bands at the crack tip was decreased

and the crack path morphology was less tortuous for the specimens with internal hydrogen.

In the scientific community, there are doubts that internal hydrogen causes the exact same effects on materials as a hydrogen gas environment, and the latter is of more industrial relevance. Ogawa et al. [47] conducted fatigue crack growth tests with two metastable austenitic stainless steels (SUS 304 and SUS 316) in a hydrogen-precharged (internal hydrogen) and uncharged condition in air and in an uncharged condition in external hydrogen. This study showed that the fatigue crack growth rate with internal hydrogen was lower than with external hydrogen in spite of a greater hydrogen content in the specimen with internal hydrogen than was estimated for the uncharged specimen tested in external hydrogen. In the same paper the strain-induced α' -martensite formation at the crack tip was evaluated. Less strain-induced α' -martensite with internal hydrogen than with external hydrogen was observed, which was proposed to be due to hydrogen suppressing martensite formation. Two studies have been performed on fatigue testing in hydrogen gas atmosphere using a bending test system with a type SUS 304 steel (0.046 wt% C, 8.7 wt% Ni). One study focused on the fracture surface in the area of short cracks in a range up to physically short cracks. In the presence of hydrogen the fracture surface is rougher than in air and striations are rarely observed [48]. The other study observed an accelerated crack propagation by hydrogen causing a larger striation spacing. Additionally, less cracks were initiated in hydrogen compared to testing in air and nitrogen [49].

All in all, a major lack of studies on fatigue crack propagation sites in hydrogen gas environment without artificial initiation sites could be identified.

2.6 Fatigue cracking of martensitic stainless steel under hydrogen influence

Far fewer studies on the hydrogen influence on fatigue of martensitic stainless steels have been performed than for austenitic stainless steels and even fewer on the actual

fatigue crack nucleation and propagation. Evaluating semi-circular notches in a smooth round specimen, Ogawa et al. observed no difference in the crack growth threshold between air and hydrogen gas [50].

Shakib et al. performed a fractographic investigation of a martensitic stainless steel with much lower carbon and nickel content than the steel evaluated here fatigued in a hydrogen gas atmosphere. The authors considered martensite lath boundaries as significant interfacial hydrogen sinks and proposed that those boundaries play a key role in crack initiation and propagation. Additionally, they state that carbides and secondary phase precipitates acting as hydrogen traps probably heavily affect the cracking behavior. [51]

Only one study by Ohmura et al. conducts nanoindentations on hydrogen-precharged specimens to examine the dislocation grain boundary interactions in a martensitic stainless steel. The results will be described in the discussion chapter 6.4. [52]

In conclusion, only a few studies have been performed on martensitic stainless steels under hydrogen influence and no comprehensive understanding has been achieved so far.

3 Scientific challenge and approach

Most components in hydrogen gas systems fail due to fatigue from the frequent pressurizing and venting cycles. As shown in the previous chapter the effect of hydrogen on fatigue short crack propagation paths in stainless steels is unclear. A better understanding of the relationship between short crack propagation in hydrogen and microstructure would aid in microstructural design and life-time improvement. Therefore, the main research question that will be addressed in this thesis is:

Which microstructural sites in austenitic and martensitic stainless steels
are susceptible to fatigue short crack propagation with and without
external hydrogen?

Answering this question will improve understanding of how hydrogen influences the mechanisms causing fatigue short crack propagation in these steels. The experimental approach to answering this research question is detailed in the following paragraphs.

Despite tension-tension loading during pressurization and depressurization, tension-compression cyclic stresses are present at the notches of components in service; therefore, all tests were conducted with tension-compression fatigue loading.

Applications in the automotive field require a high pressure hydrogen environment, which means a nominal working pressure of 70 MPa. The reason for this high pressure is to store a significant amount of gas on board a vehicle to achieve a reasonable range. Researchers have shown that increasing gas pressure can cause a more severe effect on the storage material. However, the effect of hydrogen on steels is present even at very low gas pressures, as low as 0.011 MPa [53]. The test pressure of 10 MPa used here is a compromise in terms of technical complexity regarding safety and application possibilities. Regarding the hydrogen gas environment, the hydrogen gas purity itself has a greater impact on material response than the hydrogen gas pressure. Even minor oxygen

contents, such as 19 vpm, can eliminate the effect of hydrogen on the material [54] so high purity hydrogen gas was used in this study. All reference testing was performed in inert helium gas to avoid effects due to oxygen and moisture.

A smooth specimen was designed for this study so that the location of cracking could be determined in the crystallographic structure of the particular material. In other words, the specimen itself does not have a notch because the notch would be the crack initiation site and the initial crack propagation would be influenced by the presence of the notch. To enable EBSD analysis a cylindrical specimen was modified with two opposite flat surfaces along the specimen length axis. The specimen surface was electropolished prior to testing to remove the work-hardened layer, enable light-optical inspections of the surface, and so that EBSD could be performed after fatigue testing.

The EBSD method was applied to analyze the material microstructure around the short cracks so that information about the crack path could be acquired, such as identifying intergranular and transgranular cracking, the misorientation angle and coincidence site lattice of cracked grain boundaries, and the slip systems of adjacent grains.

All in all, the greatest challenge for analyzing short cracks is stopping the test having generated only a short crack. Often in hydrogen gas only one crack initiated which could form anywhere on the specimen surface. Several approaches to aid in the interruption of tests once a short crack had formed were evaluated: thermal imaging, microscope camera, replica, and direct current potential drop (DCPD) method. The smallest crack that could have been identified by thermal imaging with the minimum required working distance of 25 cm was 300 μm because of the autoclave. Since an infrared transparent window would have been necessary, the resolution would have been even less. Unfortunately, the space in the autoclave was also too small to fit a camera with a miniature actuator. The best results were achieved by combining the replica method with the

DCPD method. Applying the replica method exclusively was very time consuming as the test had to be frequently interrupted and the vessel had to be vented and opened.

DCPD is commonly performed on notched specimens, such as notched fatigue specimens and compact tension specimens, to measure crack length, see also ASTM Standard E1820 Appendix A18 [55]. For the DCPD technique, a constant current is passed through a specimen and the resulting potential is measured. The voltage signal changes during a test are primarily due to crack propagation causing changes in the electrical resistance of the specimen. Nibur, et al. were able to detect 30 μm cracks in an austenitic stainless steel using the DCPD method on notched specimens in gaseous hydrogen [56].

In this thesis the DCPD method was conducted with smooth specimens. Due to a comparably large surface area and multiple possible crack initiation sites the method was not applicable for crack length measurements itself. Nevertheless, crack initiation could be reasonably assessed. In order to reduce the noise in the signal due to temperature fluctuations a reference probe is often attached to the specimen. Fortunately, the lack of temperature fluctuations within the autoclave resulted in no need for an additional reference probe.

4 Characterization of materials

The focus of this thesis is on the effects of hydrogen on fatigue cracking of a metastable austenitic and martensitic stainless steel. The chemical, mechanical and physical properties of the materials are described in detail below. The results presented in this chapter were obtained from a previous research project [57].

4.1 Metastable austenitic stainless steel X2CrNi19-12 (\approx 1.4306 \approx AISI304L)

The X2CrNi19-12 (X2-12), also known in Europe with the designation 1.4306 is similar to the American AISI 304L and the Japanese SUS 304L but with a higher nickel content. The comprehensive chemical composition is shown in Table 4.1. The material is a special cast by SCHMOLZ + BICKENBACK GUSS GmbH & Co. KG. The cast material was remelted and forged by Saarschmiede GmbH. The carbon content of the austenitic stainless steel investigated here is 0.016 wt% and the nickel content is 12.36 wt%. Due to the high nickel content the material is rather stable among the metastable austenitic stainless steels. After forging the material was solution heat treated at 1040°C for one hour and subsequently quenched in water. At MPA slow strain rate tensile tests with a crosshead velocity of 0.1 mm/min (strain rate $6.67 \cdot 10^{-5}$ 1/s) were performed in hydrogen and helium at 10 MPa gas pressure and at room temperature to characterize the materials. The mechanical properties of the investigated austenitic stainless steel variants are displayed in

Table 4.2. The unique tensile curves are given in the appendix in chapter A1. Testing the materials in hydrogen reveals almost no reduction in the yield strength and a slight reduction of 4 % in the ultimate tensile strength. Furthermore, the total elongation of the X2-12 is only decreased by 3 %. The relative reduction of area (RRA) is considered the most relevant value to assess hydrogen susceptibility from tensile testing and is 0.98, which also indicates a high resistance to hydrogen embrittlement. In Appendix A2

notched fatigue data about the X2CrNi19-11 with an R-ratio of 0.1 in hydrogen gas atmosphere is given.

Table 4.1: Chemical Composition of the Investigated Austenitic Stainless Steel X2CrNi19-12 (wt%) [57]

[wt%]	C	Si	Mn	P	S	Cr	Mo	Nb	Ni	Ti	N
X2-12	0.016	0.48	1.75	0.012	0.008	18.14	0.02	0.01	12.36	0.005	0.017

Table 4.2: Mechanical Properties of the Investigated Austenitic Stainless Steel X2CrNi19-12 at RT (SSRT), Crosshead Displacement Velocity 0.1 mm/min, $p=10$ MPa, [57]

	Medium	YS [MPa]	UTS [MPa]	E_t [%]	RA [%]	RRA
X2-12 (12.36 % Ni)	He	199	531	78.3	84.3	0.98
	H ₂	193	514	76.3	82.9	

Figure 4.1.1 displays the microstructure of the austenitic stainless steel perpendicular to the rolling direction of the semi-finished bar. The X2-12 in Figure 4.1.1 shows the typical austenite microstructure with several annealing twin boundaries, and the average grain size was determined to be 205 μm .

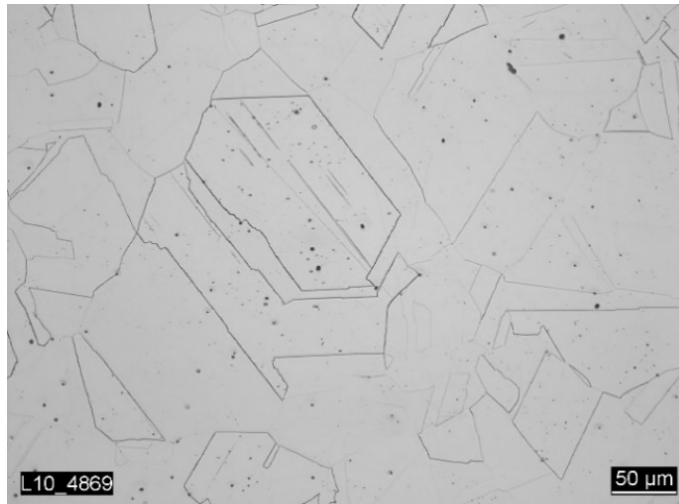


Figure 4.1.1: Light optical micrographs showing the microstructure of the austenitic stainless steel X2CrNi19-12 [57]

By applying equation (3) from chapter 2.1.1 the M_{d30} -temperature of the X2-12 is -111.99°C . Another value to characterize the austenite stability is the nickel equivalent, see equation (44) in the same chapter, which is 26.1 %.

4.2 Martensitic stainless steel X3CrNiMo13-4 (1.4313 \approx AISI415)

X3CrNiMo13-4 martensitic stainless steel is commonly used in compressors. The comprehensive chemical composition of the martensitic stainless steel investigated in this study is provided in Table 4.3.

Table 4.3: Chemical Composition of Martensitic Stainless Steel X3CrNiMo13-4 (wt%) [57]

[wt%]	C	Si	Mn	P	S	Cr	Mo	Nb	Ni	Ti	N
X3	0.023	0.42	0.61	0.018	0.001	12.38	0.368	-	4.41	0.004	-

The mechanical properties of the martensitic stainless steel listed in Table 4.4 were evaluated by performing slow strain rate tensile tests with a crosshead displacement velocity of 0.1 mm/min (strain rate $6.67 \cdot 10^{-5}$ 1/s) in helium and hydrogen gas environment of 10 MPa at room temperature. Neither the yield strength nor the ultimate tensile strength was affected by hydrogen. As for the austenitic stainless steel the most significant differences between the hydrogen and helium environments were observed in the total elongation and reduction in area. In the presence of hydrogen, the total elongation was reduced by 60 % and the reduction of area by 75 % (RRA of 0.25).

Table 4.4: Mechanical Properties of the Martensitic Stainless Steel X3CrNiMo13-4, SSRT, Crosshead Displacement Velocity 0.1 mm/min, p=10 MPa, RT [57]

	Medium	YS [MPa]	UTS [MPa]	E _t [%]	RA [%]	RRA
X3CrNiMo13-4	He	788	853	19.7	79.1	0.25
	H ₂	785	850	8.0	20.1	

The microstructure of the X3 steel is fully martensitic, as shown in the micrograph in Figure 4.2.1. The prior austenite grains have transformed to the typical martensite lath structure arranged in martensite packets and blocks.

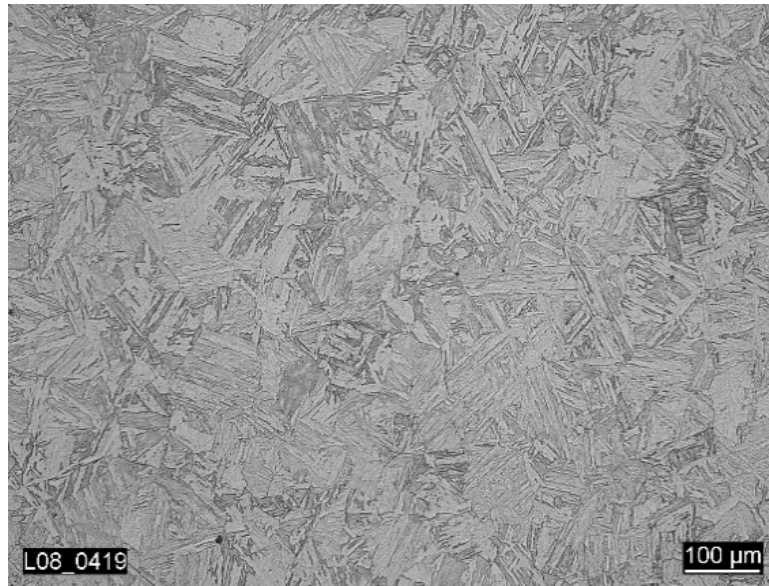


Figure 4.2.1: Light optical micrograph showing the microstructure of the martensitic stainless steel X3CrNiMo13-4 [57]

5 Experimental procedure

5.1 Sample geometry

To study the formation of cracks without a defined initiation point, as is present in specimens with machined notches, a circumferentially smooth fatigue specimen with a diameter of 5 mm was used (according to ASTM E606), as shown in Figure 5.1.1a) and b).

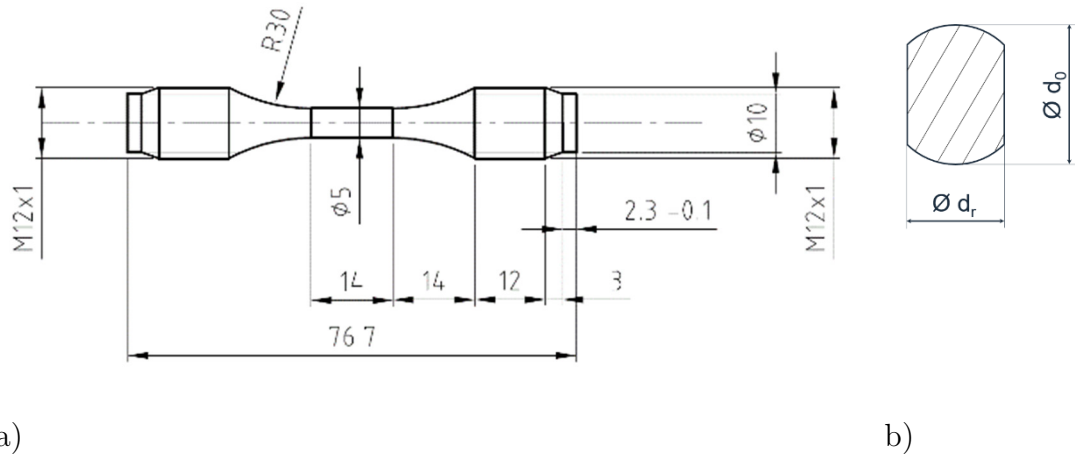


Figure 5.1.1: a) LCF specimen for tension-compression testing, b) sketch of cross section in the middle of the smooth specimen

Additionally, two sides of the smooth specimen were flattened along the specimen axis for EBSD analysis of the crystallographic structure. The flat faces are opposite of each other relative to the specimen (180° rotation), as shown in Figure 5.1.1b). This modification was performed by hand. In the last step, the specimen surface was electropolished to enable surface observations and to remove the work-hardened layer. Figure 5.1.2 displays a sketch of the device that was built to achieve reproducible electropolishing results by ensuring a constant distance between the specimen, the anode, and a metal pipe, the cathode along the length axis of the specimen. The electrolyte used to polish both stainless steels consisted of 600 ml methanol (methyl alcohol), 360 ml ethylene glycol monobutyl ether, and 60 ml perchloric acid. To polish the specimen a current flow of 24 V was applied for 45 s at 20°C .

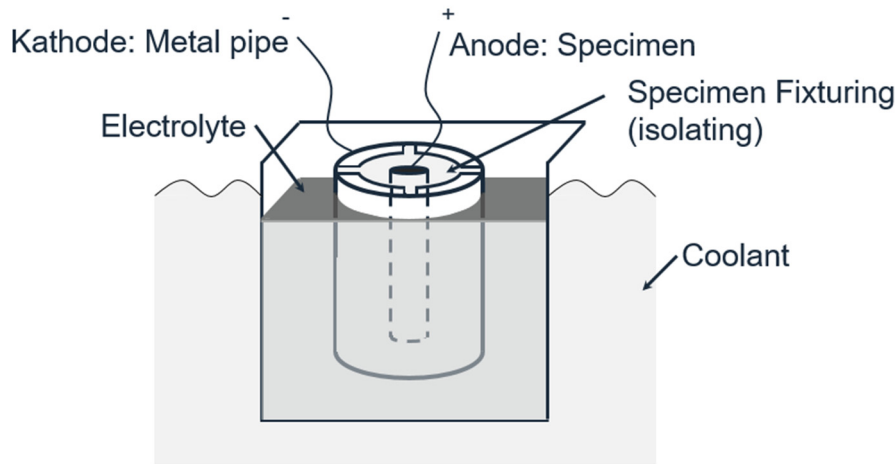


Figure 5.1.2: Electropolishing device

The diameter of the round portions and the distance between the flat surfaces was measured for each specimen to calculate the appropriate force to apply. The reduced diameter was measured with a profile projector and the minimum out of three measurements was used.

5.2 Specimen extraction from the austenitic stainless steel

The raw material was shaped as a bar with a square cross section of 40 mm x 40 mm and a total length of 6 m. Figure 5.3 illustrates the specimen extraction in detail. The bar was cut in 3 parts: Head, middle, and foot. This description refers to the direction how the bar was cast. Specimen blanks were extracted from the head and the foot by wire electrical discharge machining (EDM). All specimens were extracted parallel to the length axis of the bar.

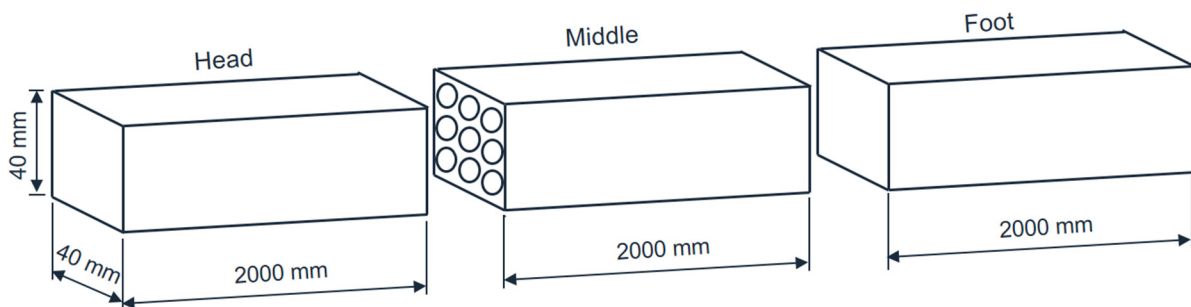


Figure 5.2.1: Illustration of specimen extraction out of the raw material for the austenitic stainless steels

5.3 Specimen extraction from the martensitic stainless steel

The raw material of the martensitic stainless steel X3 is a 70 mm thick disc with a diameter of 500 mm and in a QT900 heat treatment condition. The center of the disc was not used because of impurities of the casting process that may have accumulated there. The specimen blanks were extracted by EDM radial to the center of the disc as shown in Figure 5.3.1. After the extraction the blanks were heat treated to lower the yield stress below 800 MPa by austenitizing at 1000°C for 30 minutes followed by quenching in air and subsequently tempering at 560°C for 4 hours and cooling in air.

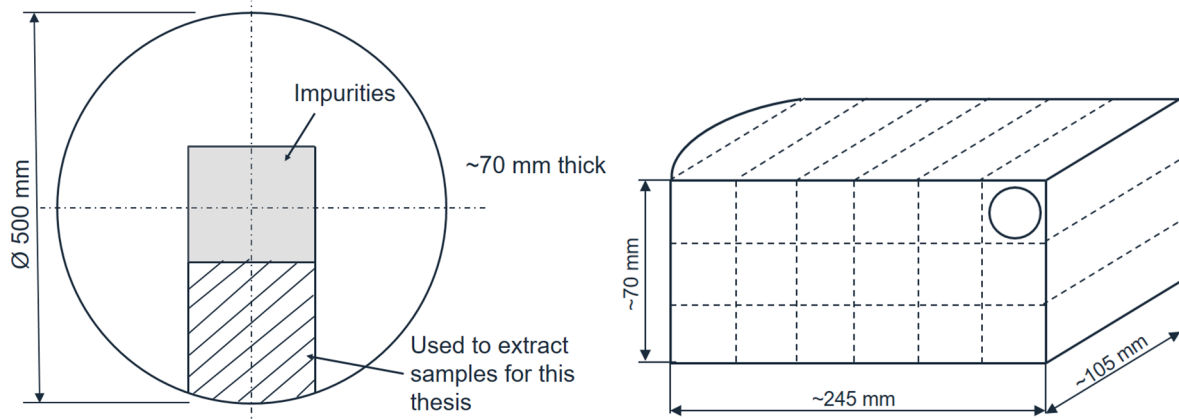


Figure 5.3.1: Schematic of the specimen extraction from the martensitic stainless steel disc

5.4 Test System

The test results shown in this thesis were exclusively generated on the system shown in Figure 5.4.1. The test system consists of a servohydraulic load frame by ZwickRoell GmbH & Co KG combined with a self-constructed and machined autoclave (maximum pressure of 30 MPa). The load cell is connected to the static pull rod outside of the autoclave. With this system tensile tests and fatigue tests both in tension-tension and in tension-compression can be performed. The TestXPert Software R1.7 by ZwickRoell is used to run the tests.

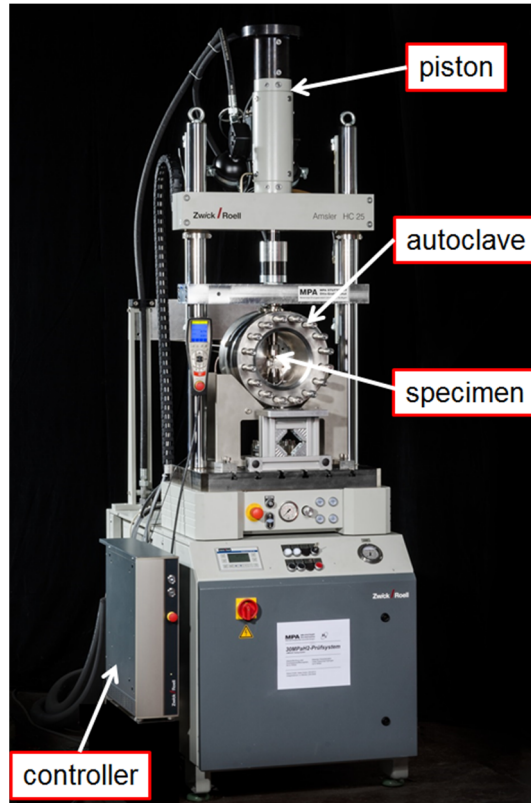


Figure 5.4.1: Servohydraulic Testing System

5.5 Test method

All tests were performed in load controlled mode with an R-ratio of -1, hence a tension-compression mode, and a triangular waveform. The pressure was 10 MPa for both hydrogen and reference testing in helium gas atmosphere. The hydrogen used as source gas had a purity of 99.9999 %. The hydrogen gas quality in the autoclave is analyzed at least once per year to ensure an oxygen content below 1 vppm and a water vapor content below 3.5 vppm (CSA CHMC-1-2014). For reference testing, helium with a purity of 99.999 % was used.

By pressurizing the autoclave the external load cell indicates a load increase because of the pull rods being pushed out of the autoclave. This force is a result of the pressure difference between the pull rod cross section and the specimen cross section. Therefore, developing a compensation method was essential. The value for the load compensation while increasing the pressure to the desired value was determined before testing the

specimens. A specimen with the geometry shown in Figure 5.1.1 was instrumented with 4 equally spaced strain gauges around the smooth surface in the middle of the specimen length. A Wheatstone bridge was also used to minimize temperature influences on the strain gauge measurements. The strain gauges showed a tension load of 6.275 kN just by increasing the gas pressure up to 10 MPa. This was the mean value of three measurements in total. Additionally, a holding time of 30 min at 2 kN and peak pressure was applied to ensure that no temperature changes had influenced the measurement due to adiabatic compression when the gas enters the autoclave.

Each specimen was cleaned with ethanol before inserting it in the autoclave. A permanent pen mark was used to document the exact position of the specimen within the test system. The flat surfaces were always in the same radial position. To verify the absence of bending in the test system the alignment was controlled regularly.

Before each hydrogen test the autoclave was first purged 5 times with helium up to 1 MPa to ensure that the autoclave would not contain an explosive hydrogen-oxygen mixture at any time. The initial helium purges were followed by 5 hydrogen purges up to 1 MPa. The final step was to increase the pressure to 10 MPa while slowly moving the actuator in order to maintain 0 N load on the specimen.

The stress amplitudes for fatigue tests of the two materials were chosen to achieve reasonable testing times in the LCF regime. The X2-12 was tested with a stress amplitude ($\Delta\sigma$) of 240 MPa and the X3 at 685 MPa. Normalized by the UTS this is equivalent to a stress ratio ($\Delta\sigma/UTS$) of 0.45 and 0.8, respectively.

5.6 Replica

For surface inspection of the specimen the replica method was used as exemplified by Figure 5.6.1. The replica method was performed with the specimen still in the fixturings of the testing system and with the autoclave open. The silicone based two component paste *RepliSet-GT1* by Struers was used. It was especially designed for replica of vertical

surfaces. The paste was first applied on one side of the specimen. To get a plain back surface of the replica a small piece of foil was laid on top of the drying paste. After 4 minutes the paste had dried and the replica was carefully removed from the specimen. Another replica on the other side of the specimen was then generated in the same manner. All replicas were taken with an applied tension load of 1 kN to prevent crack closure.



Figure 5.6.1: Exemplary application of the replica paste

5.7 Direct current potential drop method

Four probes, two current and two voltage with a diameter of 0.081 mm (American wire gauge of 28), were connected to the smooth specimen by spotwelding, see Figure 5.7.1. The current probes were attached in the middle of the round sides between the threads and the fillets. The two current probes are rotated 180° apart from each other on each end of the specimen. The voltage probes were spotwelded in the fillet of the specimen between the current probes but not in the cylindrical gage length to avoid crack initiation at the welded spots. The voltage probe positions are rotated 90° from the current probes. For all tests the current was set to 1 A, and the measured voltage signal was normalized by the voltage value at the beginning of each test. Before each test a load controlled stabilization period of 15 min at the target gas pressure was performed to stabilize the DCPD signal due to the temperature change during pressure buildup. The

noise of the signal was small enough that it was not necessary to switch the current direction during the test.

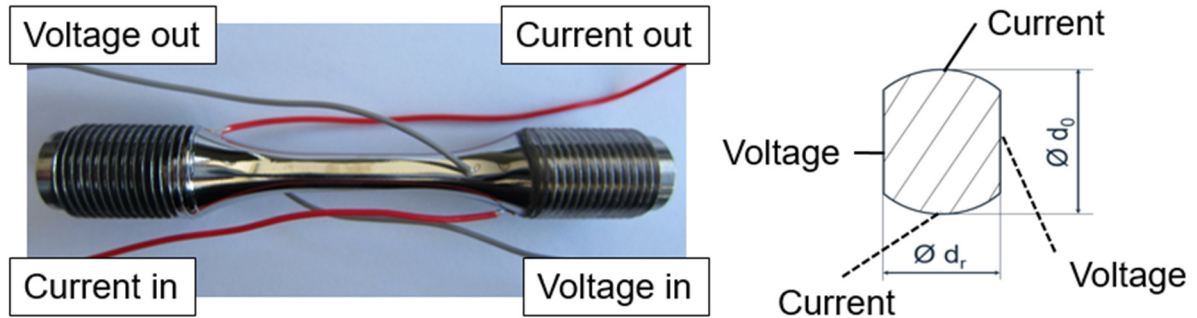


Figure 5.7.1: Instrumented smooth specimen with probes for the direct current potential drop method

The DCPD method was used to identify crack initiation in order to generate short fatigue cracks. In some specimen at least one of the cracks had already propagated long enough to doubtlessly considered as a long crack. Nevertheless, often in the same specimen secondary cracks in a fatigue short crack range (microstructurally or mechanically short) were observed that were also analyzed in this study.

5.8 Microstructural analysis techniques

Surface observations were performed with the light optical stereo microscope Axio Scope.A1 by Zeiss. Crystallographic investigations of the microstructure were conducted in a Carl Zeiss AG field emission SEM AURIGA using an EDAX EBSD camera. EBSD was performed using an accelerating voltage of 25 kV and a working distance of 23 mm. Based on the short crack size, the step size for EBSD was about 1.5 μm for the austenitic stainless steels and 0.7 μm for the martensitic stainless steel. After generating the raw data, further crystallographic analysis, e.g. cleaning up data, plotting grain maps, measuring misorientation angles, was conducted with the EDAX TSL OIM Software Analysis 7. In order to clean the measured dataset a minimum misorientation angle of 2° and a threshold of 7 adjacent pixels with the same orientation was applied using the grain

dilation function. The cleaned pixels are dilated into an adjacent crystallographic condition. The amount of 7 pixels was chosen to remove an artefact from the raw data which would lead to a 30° peak in the misorientation angle distribution for the martensitic microstructure as reported in [20]. In order to be consistent this cleaning method was used for all the IPF maps shown in this thesis.

The physical appearance of the austenite and martensite studied here was described in detail in section 2.1. In the case of the martensite the specific boundaries were introduced in Figure 2.1.4. Based on that theoretical background Figure 5.8.1 was developed in order to analyze the bulk martensitic boundary character in this thesis. When looking at the ranges for the grain boundaries in Figure 5.8.1 there are regions that overlap. To develop an analyzing method overlapping regions were assigned to only one boundary class. The following categories are assessed in this thesis: Trans-block 2° - 10° , low-packet 10° - 21° , PAG 21° - 47° , high-packet 47° - 50° , high-packet/block 50° - 57° and block boundaries 57° - 62° . Consequently, the frequency of the PAG are slightly underestimated here because the ranges between 2° - 21° and 47° - 62° were neglected.

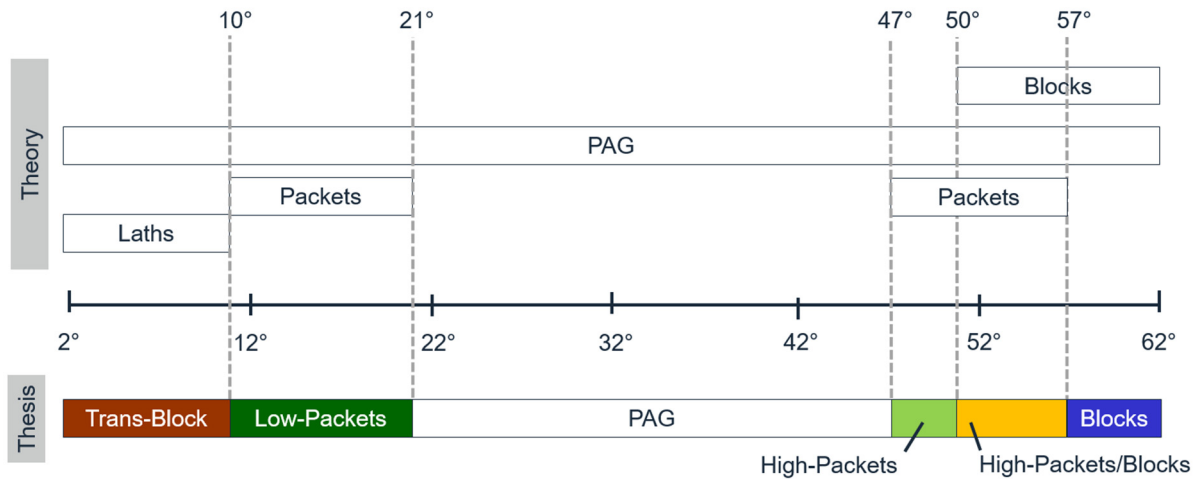


Figure 5.8.1: Classification of boundaries in the bulk lath martensite microstructure used in this thesis based on theory

Due to the respective crystallographic structure of the investigated materials the crack paths were analyzed differently. In the case of the austenitic stainless steel the crack

paths were divided into transgranular and intergranular crack portions. Subsequently, the intergranular crack portions were sub-divided into cracked grain boundary pairs. A cracked grain boundary pair is defined as two adjacent grains sharing the same grain boundary. The misorientation angles across each cracked grain boundary pair, as well as whether the cracked grain boundary pair was a $\Sigma 3$ twin boundary, were recorded. The lengths of the cracked grain boundary pairs and of the transgranular cracks were also recorded.

The target total crack length analyzed in the respective environments and per material was 2000 μm .

In the case of martensite, for which microstructural features are much smaller, the cracks were inspected closely so that accurate measurements of length fraction could be produced. For length fraction plots the crack paths were grouped into trans-block (TB), inter-low angle packet boundary (ILP), inter-prior austenite grain boundary (IPAG), inter-high angle packet boundary (IHP), a mixed section of inter-high angle packet/inter-block boundary (IHP/IB), and inter-block boundary (IB) cracking based on the classification introduced above in Figure 5.8.1. The inspection process was necessary since the misorientation angle of the inter-prior austenite grain boundary cracks overlap with the misorientation angle of the other cracked grain boundary categories. For example a cracked prior austenite grain boundary pair with an angle of 48° would be classified as IHP/IB if the categorization based on measured angle only was used, but if a crack was observed to be composed of several segments, some of which with misorientations between 21° and 47° , then the crack could be easily identified as an inter-prior austenite grain boundary crack. Number fraction plots were also produced by measuring the misorientation angles across the crack with a minimum of one data point per 15 μm .

Several cracks were believed to have initiated at chrome carbides exposed by the electropolishing process. Only one crack with a chrome carbide along the crack path was included in the analysis presented here.

To quantify the non-linearity of a crack path or in other words to describe the tortuosity of a crack the fractal dimension was determined. This mathematical approach is based on the idea that between a straight line with a dimension of 1 and a plane with a dimension of 2 there are fractal dimensions such as 1.2. The fractal dimension $fdim$ is calculated as follows where a_w is the effective crack length with tortuosity and a_s is the crack length measured directly between the two crack tips.

$$fdim = \log(a_w) / \log(a_s) \tag{6}$$

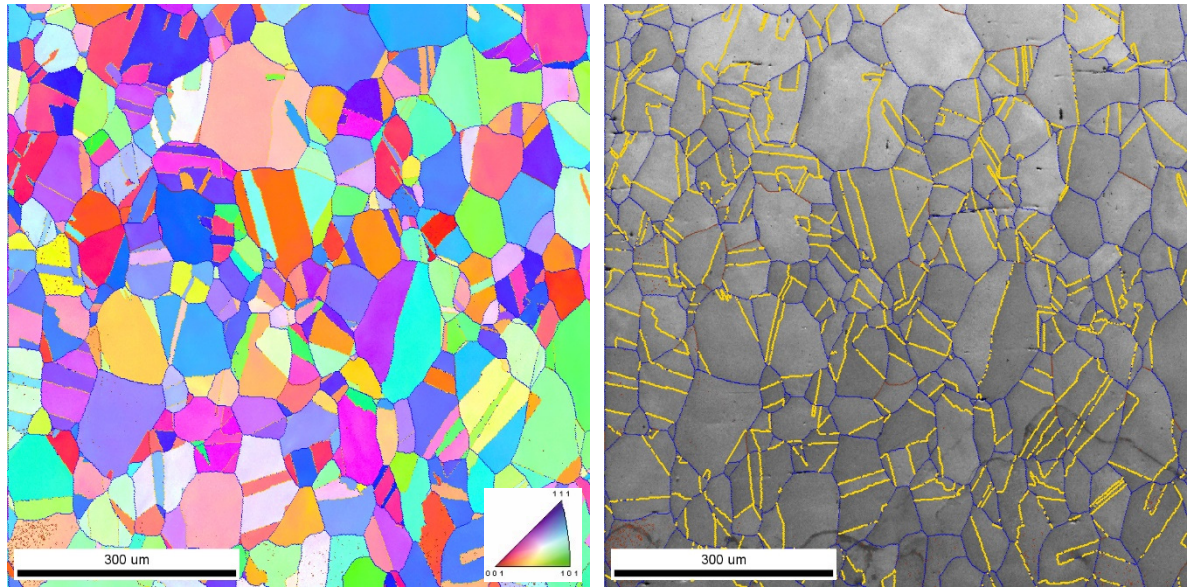
6 Results and discussion

The investigated short cracks in both materials are not necessarily either the longest crack or the first crack formed in each specimen. The term high angle boundaries excludes twin boundaries in case of the austenitic stainless steel.

6.1 Results Austenitic stainless steel (X2CrNi19-12)

6.1.1 Influence of hydrogen on the fatigue short crack sites

As a reference a 780 μm x 780 μm (328,636 data points) area of the bulk microstructure was analyzed by EBSD prior to testing. Figure 6.1.1 shows the undistorted austenite bulk microstructure with highlighted grain boundaries as a) an IPF map and b) an image quality map. Low angle boundaries with a misorientation angle between 0° and 15° are highlighted in red, high energy boundaries with a misorientation greater than 15° are highlighted in blue, and $\Sigma 3$ twin boundaries with a 60° rotation about a $\{111\}$ are highlighted in yellow.



a)

b)

Figure 6.1.1: a) IPF map and b) Image quality map of the austenitic bulk microstructure X2CrNi19-12 with highlighted boundaries: red = low angle grain boundary (0° - 15°), blue = high angle grain boundary (15° - 62°), yellow = $\Sigma 3$ twin boundary (60° around $\{111\}$)

Figure 6.1.2 shows a histogram of the grain boundary misorientation angle distribution in the austenite bulk microstructure as a length fraction. The number of low angle boundaries in the range of 0° to 15° is much lower than that of the high angle boundaries (greater than 15°). A large fraction of 0.48 at 58° - 60° in Figure 6.1.2 is due to the high number of twin boundaries in the X2 austenitic microstructure. More than every third boundary in the X2- steel is a twin boundary (36.6 %), which is typical for annealed austenitic stainless steel.

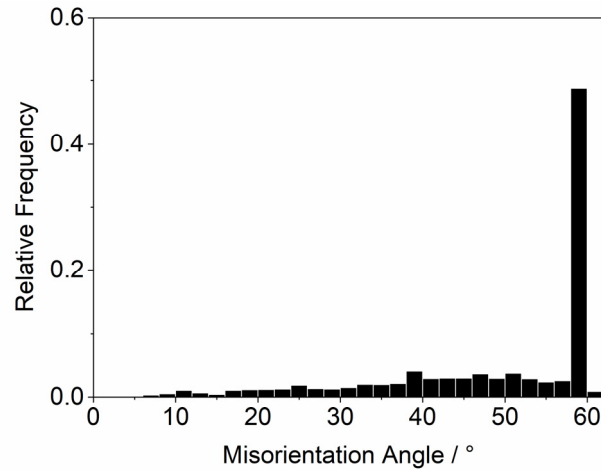


Figure 6.1.2: Misorientation angle distribution of the austenite bulk microstructure X2CrNi19-12

Table 6.1: Grain boundary length fraction of classified grain boundaries in the austenitic stainless steel X2CrNi19-12

	Bulk fraction
Low angle boundary (0° - 15°)	6.7 %
High angle boundary (15° - 62°)	56.7 %
$\Sigma 3$ twin boundary	36.6 %

Total short crack lengths of 2440 μm formed in hydrogen and of 2837 μm formed in helium were analyzed to compare the crack sites in the austenitic stainless steel. These short crack lengths are derived from 14 unique hydrogen and 15 unique helium short

cracks, which consist of 32 and 27 intergranular cracked grain pairs, respectively. The longest investigated hydrogen crack is 545 μm , and the shortest is 48 μm . In the case of the analyzed helium cracks, the longest is 564 μm , and the shortest is 48 μm . The arithmetic average crack length of the hydrogen cracks is 174 μm , and for the helium cracks it is 188 μm .

Figure 6.1.3 shows the fraction of intergranular and transgranular cracking for short cracks in hydrogen and helium gas atmosphere. A slightly greater tendency for transgranular cracking in helium is evident.

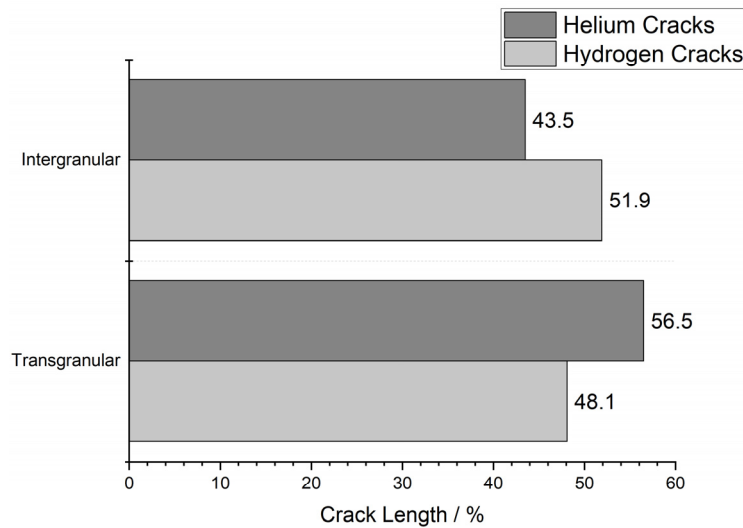


Figure 6.1.3: Transgranular and intergranular short crack lengths of helium and hydrogen cracks in the austenitic stainless steel X2CrNi19-12

Figure 6.1.4 provides the short crack length fractions from intergranular cracking along low angle boundaries, high angle boundaries, and $\Sigma 3$ twin boundaries, as well as the length fractions of those boundaries in the bulk microstructure. Neither the hydrogen nor the helium short cracks followed low angle misorientation boundaries even though 7 % of the grain boundaries in the bulk microstructure are low angle boundaries. In the case of the helium short cracks the percentage of cracking along high angle and $\Sigma 3$ twin boundaries was 30 % and 70 %, respectively. In the case of the hydrogen short cracks, almost the same amount of short cracks (72 %) are along $\Sigma 3$ twin boundaries and 28 %

of cracks follow high angle boundaries (twin boundaries excluded). The short crack lengths, number of cracked grain boundary pairs, and length fractions for both environments are listed in Table 6.2.

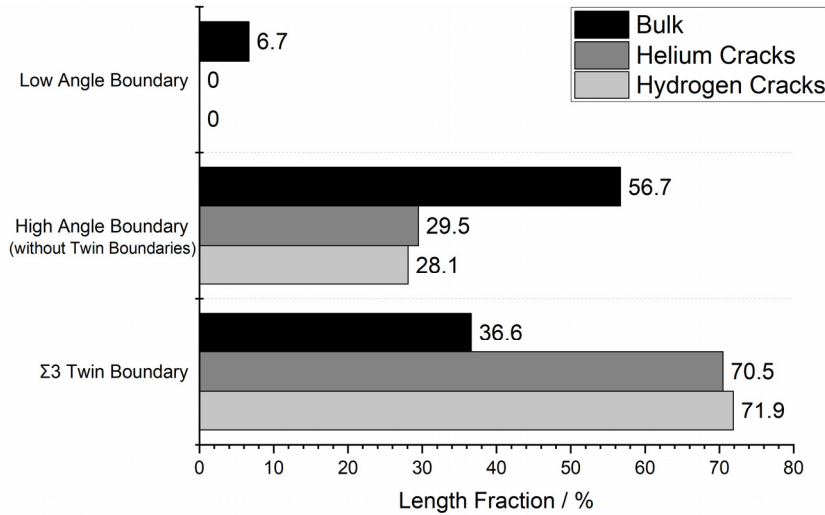


Figure 6.1.4: Length fraction of boundaries in the bulk structure and intergranular short helium and hydrogen fatigue cracks classified as low angle boundaries, high angle boundaries (without twin boundaries), and $\Sigma 3$ twin boundaries in the austenitic stainless steel X2CrNi19-12

Table 6.2: Absolute Values of Short Crack Lengths in the Austenitic Stainless Steel X2CrNi19-12

	Hydrogen			Helium		
	Number	Length [μm]	Fraction [%]	Number	Length [μm]	Fraction [%]
Total cracks	14	2441	100	15	2818	100
Total crack pairs	72	2441	100	75	2818	100
Total crack pairs TG	40	1267	51.9	48	1604	56.9
Total crack pairs IG (without twins)	17	330	13.5	10	358	12.7
Total crack pairs on $\Sigma 3$ twin	15	844	34.6	17	856	30.4

Figure 6.1.5 shows cracked grain boundary misorientation distributions as a comparison between the crack sites in the austenitic stainless steel generated in the a) hydrogen and b) helium gas atmosphere. In both atmospheres intergranular crack pairs form exclusively on high angle misorientation boundaries greater than 20° . However, most of the cracks grow along boundaries very close to 60° . This result is not surprising considering the high fraction of 60° boundaries in the bulk structure. 70 % of the cracked grain pairs formed in hydrogen are on grain boundaries close to 60° and in helium it is 74 %.

It shall be noted that not every grain boundary with a misorientation angle close to 60° is a $\Sigma 3$ twin boundary.

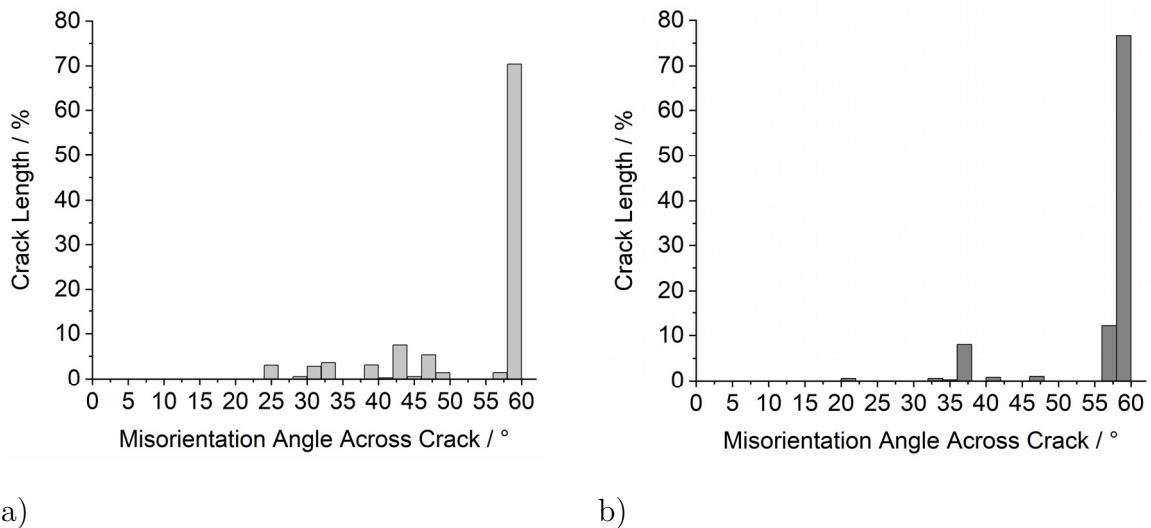


Figure 6.1.5: Misorientation angle distribution across all intergranular crack pairs in the austenitic stainless steel X2CrNi19-12 as length fraction a) in hydrogen and b) in helium gas atmosphere

Figure 6.1.6 shows an IPF map of an exemplary transgranular fatigue short crack developed in helium gas atmosphere. The same crack as a white line is displayed in the upper right corner in an SEM image taken with the forward-scattered electron detector. The color changes of the grains along the crack is a result of the plastic deformation

causing a distortion of the austenite lattice in the cracked grains. In this example the short crack is completely transgranular.

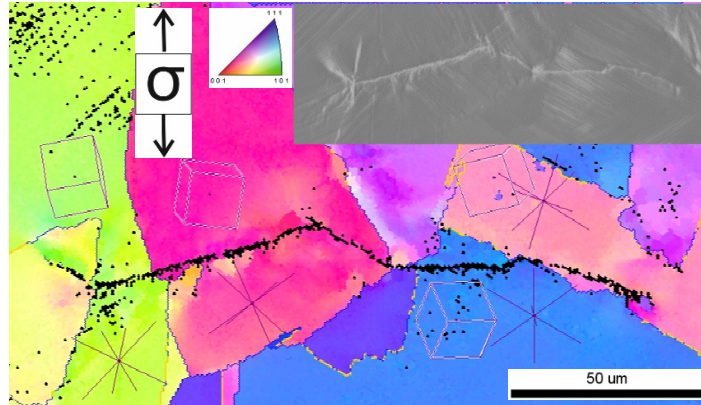


Figure 6.1.6: Exemplary helium fatigue short crack in the metastable austenitic stainless steel X2CrNi19-12. Crack length is 147 μm . IPF and SEM forward-scattered electron detector image indicating the crack in white. Highlighted grain boundaries: blue= 15° - 60° , yellow= $\Sigma 3$ twin boundary and displayed $\{111\}$ slip plane traces

An exemplary IPF image of an intergranular fatigue short crack developed in the hydrogen gas atmosphere is shown in Figure 6.1.7. The SEM image in the upper right corner indicates the crack as a white line. The short crack initiates intergranularly along a $\Sigma 3$ twin boundary. The left crack tip deflected transgranularly away from the grain boundary at an angle perpendicular to the tensile axis.

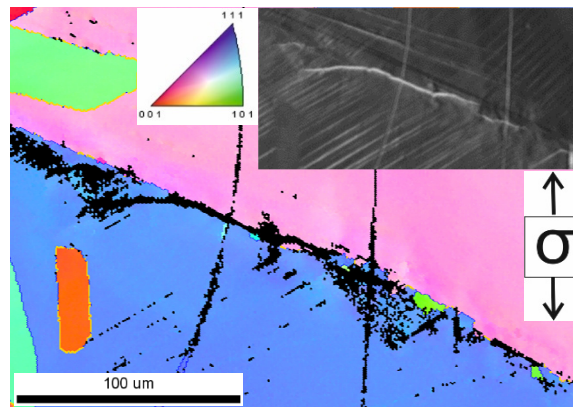


Figure 6.1.7: Exemplary hydrogen fatigue short crack along a $\Sigma 3$ twin boundary in the metastable austenitic stainless steel X2CrNi19-12 with 114 μm , IPF and SEM forward-scattered electron detector image indicating the crack in white, highlighted grain boundaries blue= 15° - 60° and yellow= $\Sigma 3$ twin boundary

After analyzing the intergranular cracking sites the transgranular crack parts are in focus in this paragraph. To gain information as to along which crystallographic planes the cracks grew, plane traces were placed in the grains as indicated by a cross showing how the $\{111\}$ slip planes exit the free grain surface, which can be seen in Figure 6.1.6.

In order to quantify the crack path on the smooth specimen surface the fractal dimension for the hydrogen and helium cracks was calculated as described in chapter 5.8. The average fractal dimension of the hydrogen fatigue short cracks in the austenitic stainless steel is 1.0078 and the average fractal dimension of the helium short cracks is 1.0041. This means that at least in the short crack growth regime, no significant quantitative difference in the tortuosity of the crack paths could be identified.

6.1.2 Crack initiation sites and microstructurally short cracks in austenitic stainless steel under hydrogen influence

This section focuses on the crack initiation sites and microstructurally short cracks; therefore, only cracks shorter than 100 μm are analyzed here.

Figure 6.1.8 displays an exemplary microstructurally short fatigue crack developed in helium gas atmosphere. The SEM image in the upper right corner shows the short crack as a black line. The helium cracks often form within a grain close to a grain boundary triple point. Surprisingly, the short cracks do not predominately initiate on the slip plane closest to the maximum shear stress. Multiple persistent slip bands are visible in the surroundings of the helium cracks due to the plastic deformation of the material.

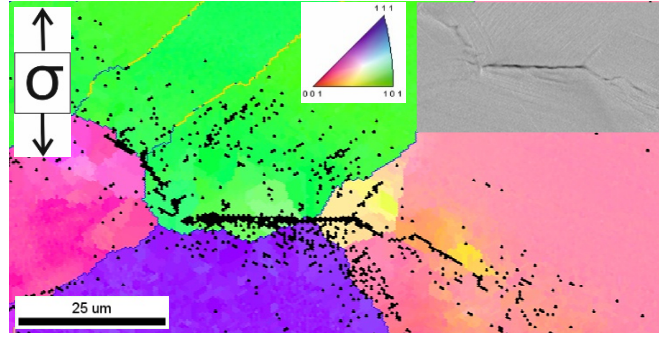


Figure 6.1.8: Microstructurally short fatigue crack formed in helium gas atmosphere, IPF and SEM image with 48 μm ; highlighted grain boundaries blue= 15° - 60° and yellow= $\Sigma 3$ twin boundary

No significant difference in the frequency of intergranular and transgranular cracking was observed between hydrogen and helium; however, microstructurally short cracks tended to initiate along $\Sigma 3$ twin boundaries in the hydrogen gas environment as shown in Figure 6.1.9. After 56 μm of cracking along the twin boundary, the crack propagated transgranularly at the left crack tip. The green area left of the crack is strain-induced α' -martensite.

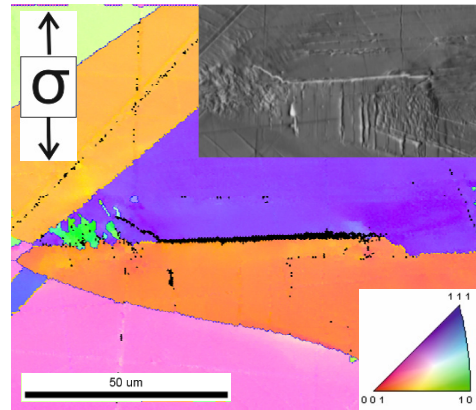


Figure 6.1.9: Microstructurally short fatigue crack formed in hydrogen gas atmosphere, IPF and SEM forward scattered electron detector image with 70 μm ; highlighted grain boundaries blue= 15° - 60° and yellow= $\Sigma 3$ twin boundary

In Figure 6.1.10 a more quantitative analysis of the $\Sigma 3$ twin boundary fraction of each individual crack sorted by the crack length is given. However, no substantial evidence of exclusive crack initiation along $\Sigma 3$ twin boundaries is present.

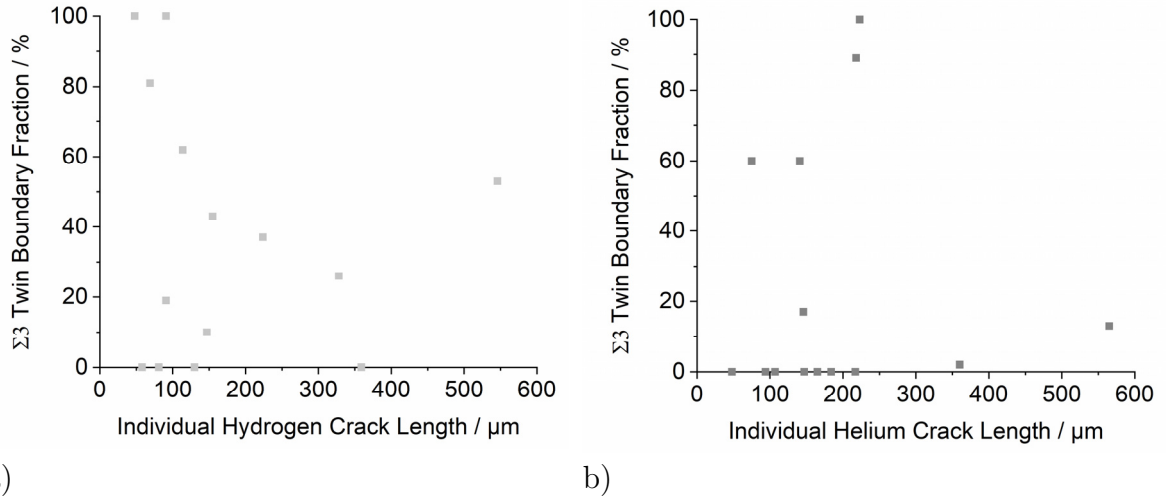


Figure 6.1.10: $\Sigma 3$ twin boundary fraction of the individual fatigue short crack lengths in the metastable austenitic stainless steel X2CrNi19-12 for a) hydrogen and b) helium gas atmosphere

For ductile materials the critical resolved shear stress can have a significant influence on crack initiation, as described in chapter 2.4. To identify the magnitude of the resolved shear stress for the slip system that is most favorably oriented for slip in each individual grain the Schmid factor is assessed. An evaluation of the Schmid factors of grains along intergranular cracks is displayed in Figure 6.1.11. The minimum measured Schmid factor was 0.34, and therefore, the number fractions from 0.34 to the maximum Schmid factor of 0.5 were binned into 17 classes. Figure 6.1.11a) and b) is a comparison of all intergranular cracks developed in hydrogen and helium respectively. Similar to the misorientation angle analysis above no evidence for a hydrogen influence depending on the Schmid factor is observed in terms of crack initiation and crack propagation sites. No significant influence of neither the hydrogen nor the $\Sigma 3$ twin boundaries can be observed, Figure 6.1.11c) and d). Regarding intergranular crack paths not following $\Sigma 3$ twin boundaries in helium no trend is present in Figure 6.1.11e) whereas for hydrogen cracks Figure 6.1.11f) the boundaries with a high Schmid factor are more susceptible to hydrogen-induced cracking.

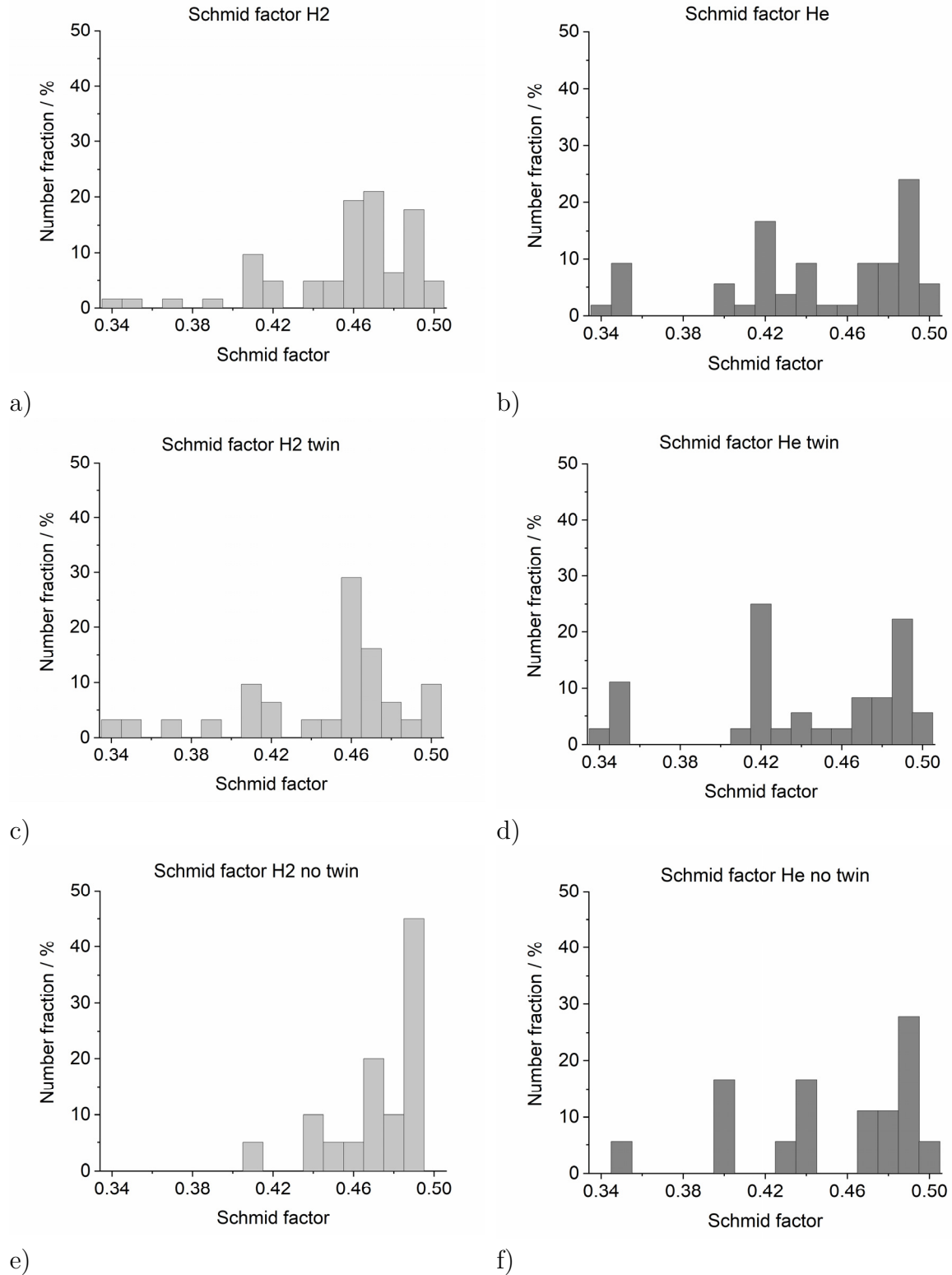


Figure 6.1.11: Schmid factor of individual grains adjacent to intergranular crack pairs in austenitic stainless steel X2CrNi19-12 a) all hydrogen crack pairs, b) all helium crack pairs, c) hydrogen crack pairs along $\Sigma 3$ twins, d) helium crack pairs along $\Sigma 3$ twins, e) hydrogen crack pairs along grain boundaries that are not $\Sigma 3$ twins, f) helium crack pairs along grain boundaries that are not $\Sigma 3$ twins

Studies of austenitic stainless steel without hydrogen have shown that not only the Schmid factor of the grains adjacent to the crack path but also the Schmid factor mismatch across the cracked grain boundary may play an important role for fatigue crack initiation and propagation [58]. Therefore, in a second step the Schmid factor mismatch across intergranular cracks as a number fraction is investigated, see Figure 6.1.12. Figure 6.1.12a), c), and e) refer to crack pairs developed in hydrogen whereas Figure 6.1.12b), d) and f) refer to crack pairs developed in helium gas atmosphere. In the upper row, Figure 6.1.12a) and b), show the result of all intergranular cracks and in the middle row, c) and d) are the result from cracking only on $\Sigma 3$ twin boundaries. At last the lower row Figure 6.1.12e) and f) illustrate the Schmid factor along random grain boundaries. In hydrogen e) only cracking on boundaries with a low Schmid factor mismatch is observed. All figures show the majority of cracking occurs between grains with a rather small Schmid factor mismatch of up to 0.08. This result is somewhat surprising as a high Schmid factor mismatch is known to cause microstructural strain and stress localization and is therefore believed to facilitate crack propagation. The comparison of non $\Sigma 3$ twin boundaries reveals a significant difference such that in hydrogen almost all crack pairs occur on grain boundaries with a low Schmid factor mismatch. A more detailed discussion can be found in chapter 6.2.

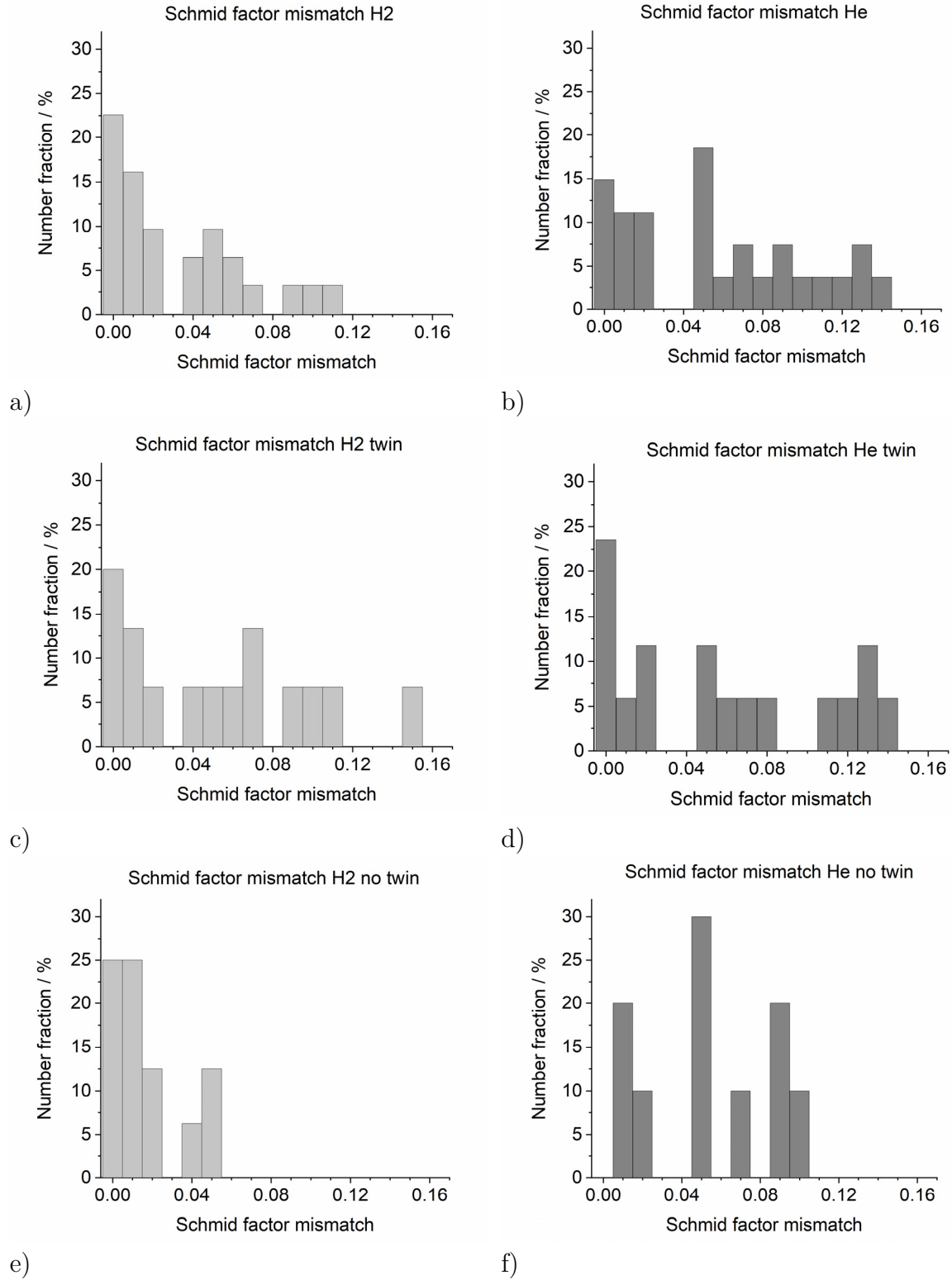


Figure 6.1.12: Schmid factor mismatch across intergranular crack pairs in austenitic stainless steel X2CrNi19-12, number fraction a) all hydrogen crack pairs, b) all helium crack pairs, c) hydrogen crack pairs along $\Sigma 3$ twins, d) helium crack pairs along $\Sigma 3$ twins, e) hydrogen crack pairs along grain boundaries that are not $\Sigma 3$ twins, f) helium crack pairs along grain boundaries that are not $\Sigma 3$ twins

As an analysis in number fraction is rather superficial and the length of each crack pair is not taken into account a Schmid factor mismatch analysis in length fraction was performed, see Figure 6.1.13. For simplified comparison the same binning as in Figure 6.1.12 was applied. Figure 6.1.13a), c), and e) show the results from the hydrogen cracks and Figure 6.1.13b), d), and f) show the helium crack results. Moreover, Figure 6.1.13c) and d) exclusively focus on $\Sigma 3$ twin boundaries. In case of the crack pairs developed in helium most cracking of the intergranular crack length was observed between grains with a Schmid factor mismatch greater than 0.08. As well as for the number fraction the length fraction plot for non $\Sigma 3$ twin boundaries in hydrogen, Figure 6.1.13e), show most cracking occurs along grain boundaries with a low Schmid factor mismatch. Possible explanations for these results and how these findings can come to an agreement is stated in the discussion chapter 6.4.

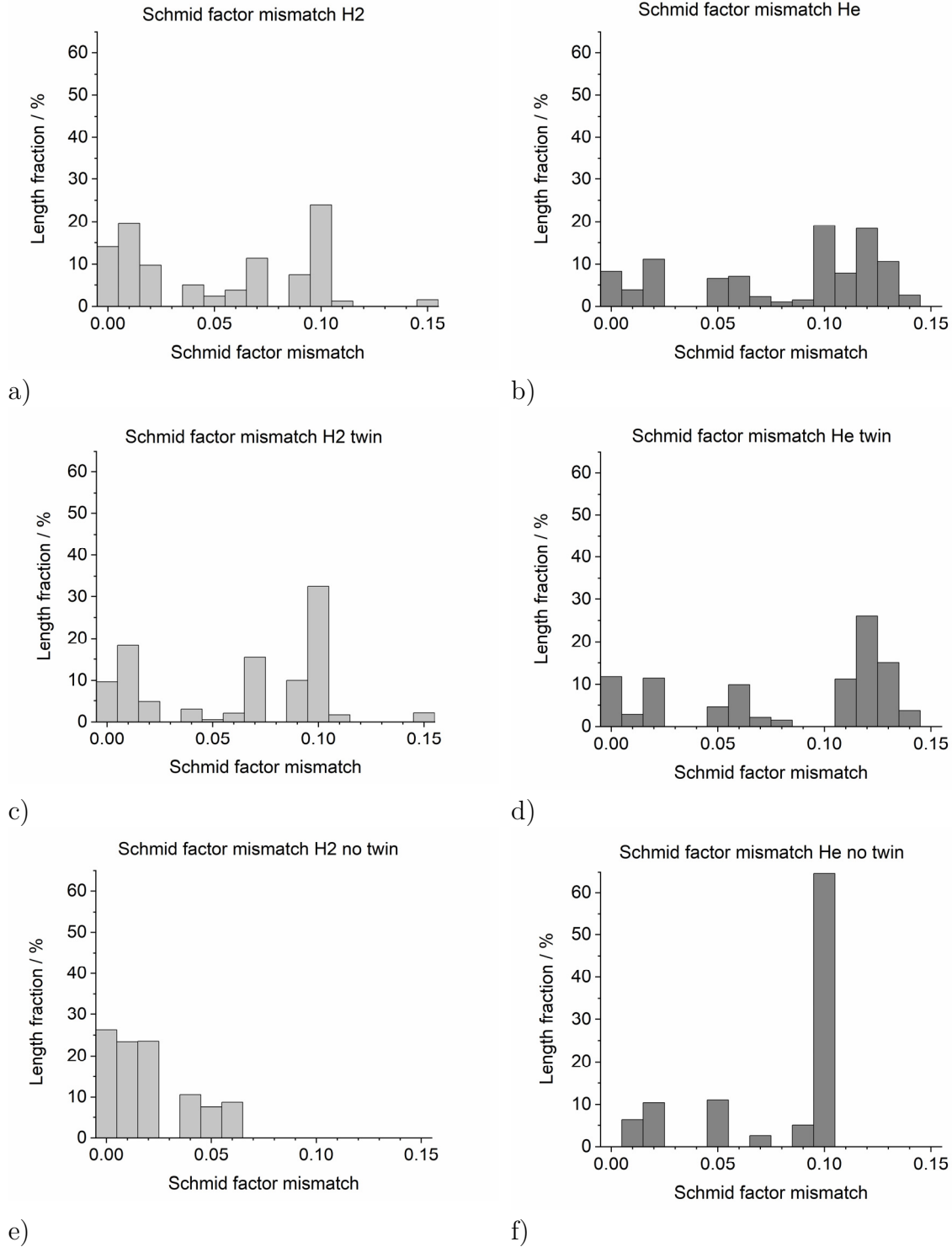


Figure 6.1.13: Schmid factor mismatch across intergranular crack pairs in austenitic stainless steel X2CrNi19-12, length fraction a) all hydrogen crack pairs, b) all helium crack pairs, c) hydrogen crack pairs along $\Sigma 3$ twins, d) helium crack pairs along $\Sigma 3$ twins, e) hydrogen crack pairs along grain boundaries that are not $\Sigma 3$ twins, f) helium crack pairs along grain boundaries that are not $\Sigma 3$ twins

Whereas the Schmid factor mismatch describes the stress compatibility the Taylor factor mismatch indicates strain compatibility across a grain boundary and was helpful to explain intergranular cracking elsewhere [7,58–60]. Therefore, additional evaluation of the crack pairs in terms of the Taylor factor of the adjacent individual grains was performed as presented in Figure 6.1.14. To evaluate hydrogen influence (Figure 6.1.14b), d), and f)) in comparison to the helium atmosphere (Figure 6.1.14a), c), and e)) the Taylor factor mismatch between the minimum and the maximum measured values is assessed as a number fraction. The Taylor factor does not have a distinct effect on fatigue short crack propagation neither in hydrogen nor in helium. No influence on cracking on terms of the grain boundary character could be observed.

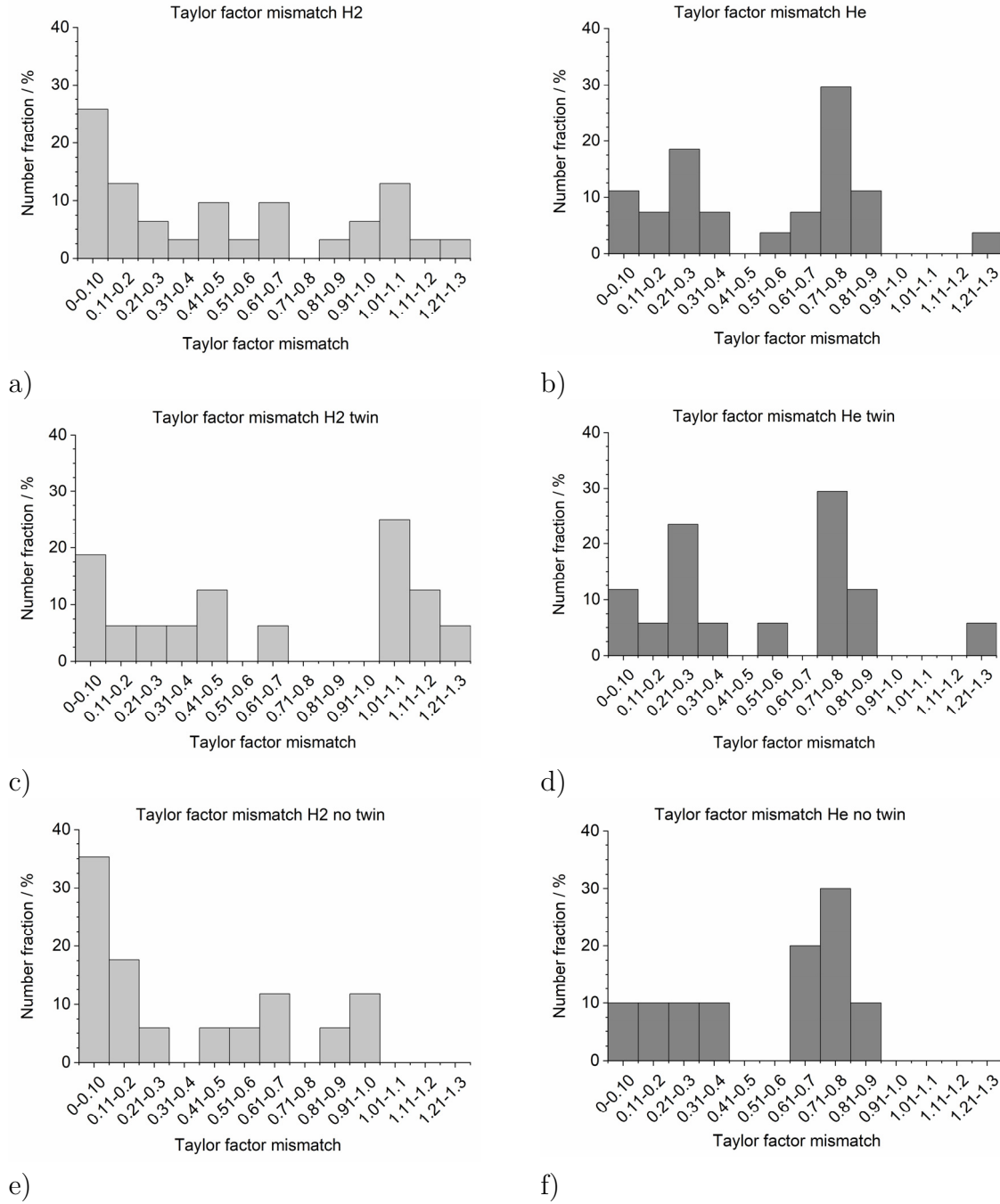


Figure 6.1.14: Taylor factor mismatch across intergranular crack pairs in austenitic stainless steel X2CrNi19-12, number fraction a) all hydrogen crack pairs, b) all helium crack pairs, c) hydrogen crack pairs along $\Sigma 3$ twins, d) helium crack pairs along $\Sigma 3$ twins, e) hydrogen crack pairs along grain boundaries that are not $\Sigma 3$ twins, f) helium crack pairs along grain boundaries that are not $\Sigma 3$ twins

To develop a more comprehensive evaluation the Taylor factor mismatches for the fatigue short cracks were also analyzed by length fraction, as shown in Figure 6.1.15. In

the same manner as the figures shown previously, Figure 6.1.15a), c), and e) show the Taylor factor mismatches of the cracks developed in hydrogen versus that for the cracks developed in helium in Figure 6.1.15b), d) and f). Figure 6.1.15 c) and d) refer only to $\Sigma 3$ twin boundaries.

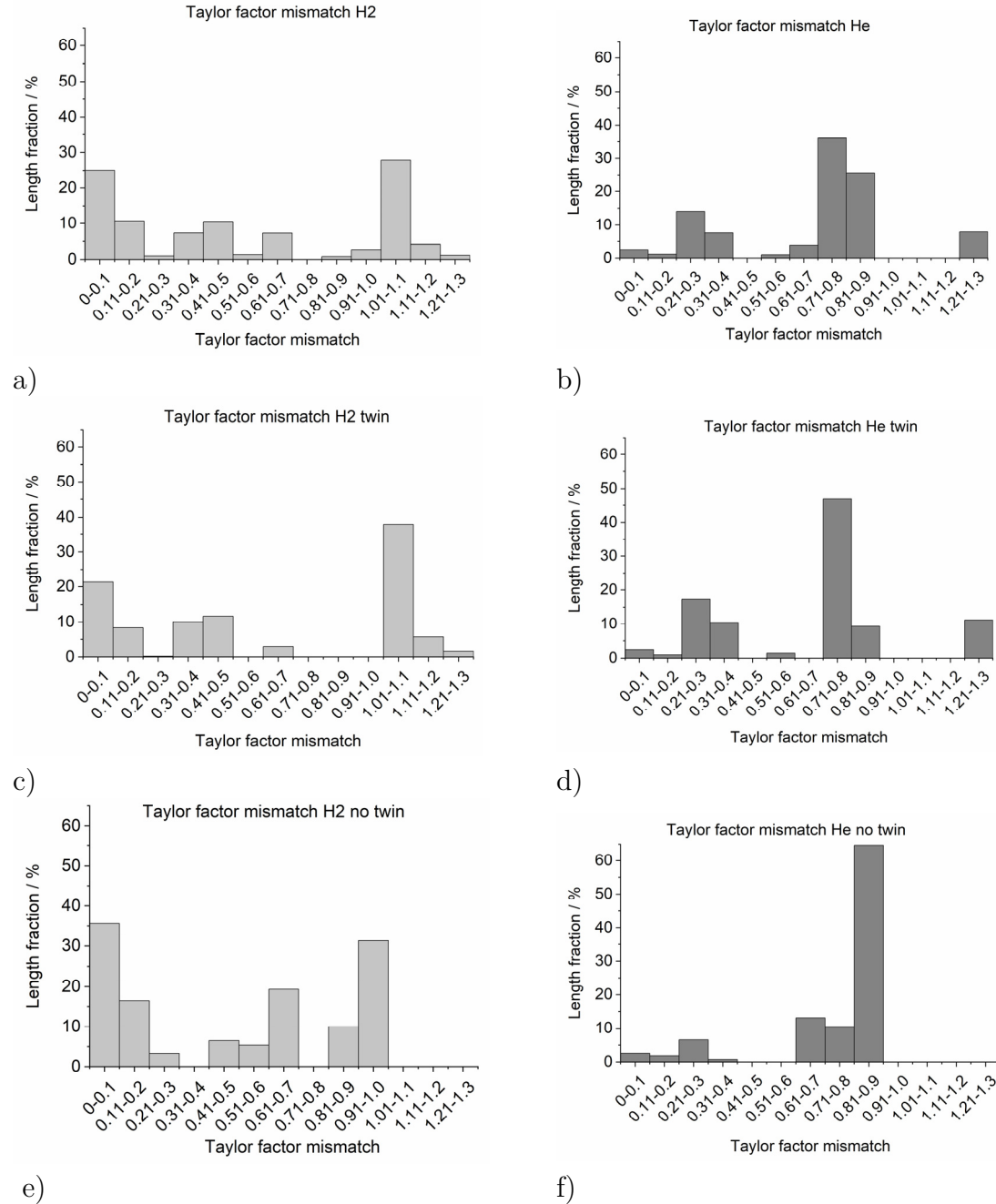


Figure 6.1.15: Taylor factor mismatch across intergranular crack pairs in austenitic stainless steel X2CrNi19-12, length fraction a) all hydrogen crack pairs, b) all helium crack pairs, c) hydrogen crack pairs along $\Sigma 3$ twins, d) helium crack pairs along $\Sigma 3$ twins, e) hydrogen crack pairs along grain boundaries that are not $\Sigma 3$ twins, f) helium crack pairs along grain boundaries that are not $\Sigma 3$ twins

6.1.3 Strain-induced martensite formation

As the metastable austenitic stainless steel with 12 % nickel has a Md30-temperature of -111.99°C and a nickel equivalent of 26.1 %, it is already a rather stable material so a minimal amount of strain-induced martensite would be expected to form during fatigue testing. Nevertheless, a qualitative analysis of the hydrogen influence on the austenite-martensite phase transformation is given in this section.

Figure 6.1.16 and Figure 6.1.17 show the phase maps of short fatigue cracks in the metastable austenitic stainless steel formed in hydrogen and helium gas, respectively. The γ -austenite is marked in red and the α' -martensite is highlighted in green. The crack itself and persistent slip bands are black. The strain-induced martensite can be detected predominately very close to the cracks, which is typical. A major influence of the hydrogen on the amount of strain-induced martensite cannot be observed.

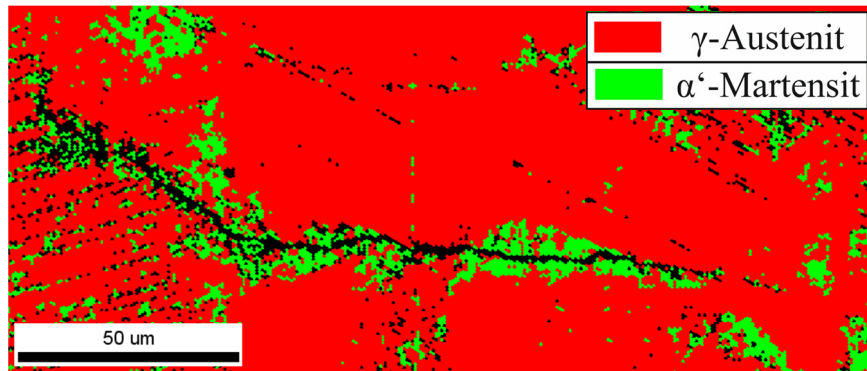


Figure 6.1.16: Phase map of a short helium fatigue crack in the austenitic stainless steel X2CrNi19-12

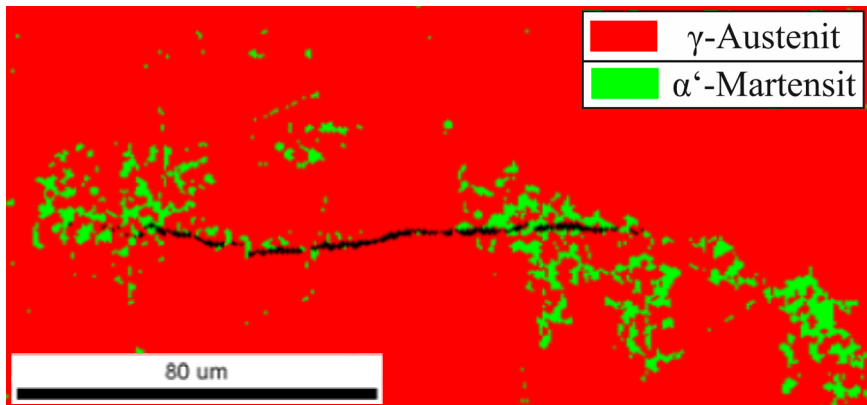


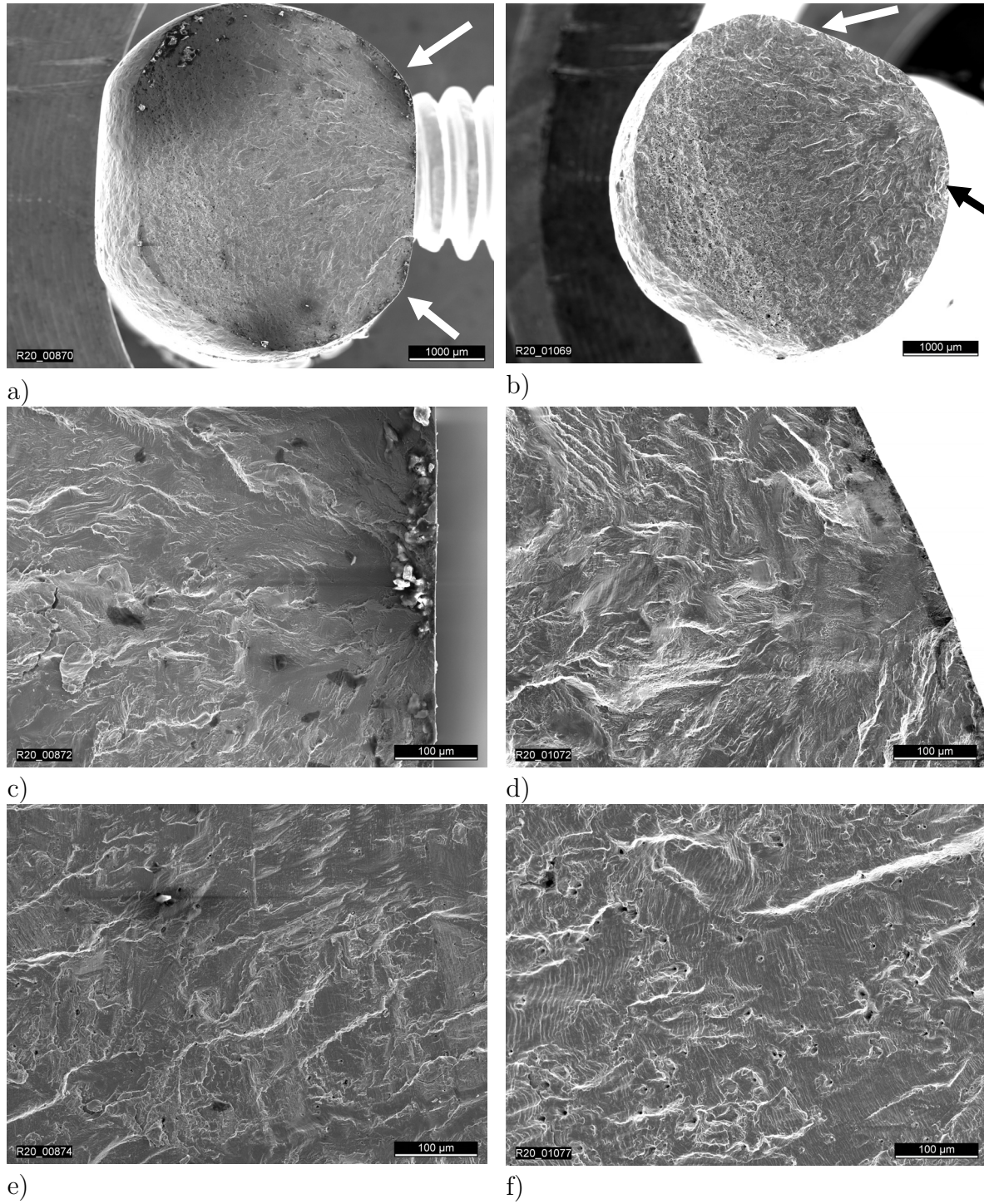
Figure 6.1.17: Phase map of a short hydrogen fatigue crack in the metastable austenitic stainless steel X2CrNi19-12

6.1.4 Fractography of austenitic stainless steel

Almost all specimen for this study were stopped after developing short cracks and subsequently modified to analyze them such that no further testing could be conducted. The specimen displayed in this chapter were fatigued until failure without analyzing any short cracks on the specimen surface.

The fact that crack growth is not a two-dimensional process belies the need to examine the fatigue fracture surface. In Figure 6.1.18 SEM images of a fatigue fracture surface tested in hydrogen gas a), c), e) and helium gas b), d), f) are displayed. An overview of the entire fatigue fracture surface is shown in a) and b). In the bottom left of the images the area of the ductile overload can be identified. The crack initiation sites are shown in Figure 6.1.18c) and d) and regions of long crack growth are shown in Figure 6.1.18e) and f).

The first general observation is a smoother fracture surface in the case of the specimen tested in the hydrogen gas atmosphere. In both specimens there are multiple crack initiation sites visible. For the specimen tested in hydrogen a) the initiation sites are indicated by arrows. Small secondary cracks are present only in the specimen tested in hydrogen as in c). Besides these secondary cracks no distinct facets which usually accompany a brittle fracture manner are observable neither close to the initiation sites nor in the long crack range in e) and f). In f) the helium long crack growth shows more distinct striations than the hydrogen long crack growth in e).



Hydrogen

Helium

Figure 6.1.18: Fatigue fracture surface of the austenitic stainless steel tested with 1 Hz at $R=-1$ at room temperature in hydrogen and helium gas at 10 MPa, a) overview H₂ surface, b) overview He surface, c) initiation site H₂, d) initiation site He, e) long crack growth area H₂, f) long crack growth area He

6.2 Discussion austenitic stainless steel (X2CrNi19-12)

The austenitic stainless steel X2CrNi19-12 exhibited no significant influence of hydrogen on the transgranular and intergranular short fatigue crack fractions. The RRA value from tensile testing in hydrogen and helium gas environment, which is close to one, also indicates minimal susceptibility to hydrogen for this material. Both in helium and in hydrogen the fractions of cracking for each grain boundary class (low angle, high angle without twins, and $\Sigma 3$ twin boundaries) are not in accordance with the fraction of grain boundaries in the bulk microstructure; about 30 % more cracking along $\Sigma 3$ twin boundaries was observed compared to the bulk microstructure.

The order in the discussion below will follow the structure of the results chapter. First, the high amount of twin boundary cracking will be evaluated. An evaluation of the Schmid and Taylor factor of the grains adjacent to cracks will follow. Finally, the effect of hydrogen on α' -martensite formation will be discussed briefly.

As already shown in literature the nickel content has a significant effect on the materials properties in hydrogen gas atmosphere [61–64] and the relatively high nickel content of 12 wt.% may be why no difference in the crack sites in this thesis for the austenitic stainless steel was observed. However, the fact that in helium and hydrogen the cracked sites show no particular difference in this study does not mean that hydrogen has no influence on the fatigue cracking. The fatigue properties of austenitic stainless steels can still be affected by hydrogen gas atmosphere. For example, Aoki et al. observed a higher crack growth rate for a 304L austenitic stainless steel with 0.043 wt.% C and 8.7 wt.% Ni [49]. Additionally, twin boundaries were previously reported to be favorable for growth of long fatigue cracks under hydrogen influence in a 304L austenitic stainless steel with a low nickel content of 8 wt.% by Ueki et al. [65]. In a hydrogen pre-charged small-scale CT specimen twin boundary separation preceded quasi-cleavage fracture and the crack propagated along the twin boundary. In the uncharged specimen the crack

deflected from the twin boundary and propagated transgranularly. The authors concluded that hydrogen reduced the interatomic bonding energy. [65] The results of Ueki et al. indicate that hydrogen can shift the microstructural location of crack growth in lower nickel content austenitic steels; therefore, the higher nickel content of the austenitic stainless steel in this thesis may prevent activation of different short crack growth sites by hydrogen.

To gain a better understanding of the experimental results numerical studies are a beneficial tool. Lacking detailed numerical studies on the hydrogen influence on intergranular cracking of grain boundaries in austenitic steels results from simulations of pure nickel, which also has an fcc lattice structure, are considered. Many numerical studies (first-principle and MD simulations) about hydrogen influence on various grain boundaries are available for pure nickel [66–71]. It was observed that hydrogen diffusion is significantly facilitated along a $\Sigma 3$ twin boundary compared to a random grain boundary of 43° [72]. However, just the fact that hydrogen diffuses faster along special grain boundaries does not explain why those boundaries would be favorable sites for cracking, and the results in this thesis indicate that any differences in diffusion rate between twin boundaries and random grain boundaries has minimal effect on the sites for short crack growth in hydrogen environments.

The susceptibility of $\Sigma 3$ twin boundaries to cracking in both environments may be more related to the function of the boundaries as an obstacle to dislocation motion. $\Sigma 3$ twin boundaries oriented perpendicular to the tensile axis would have 3 active slip systems for both grains adjacent to the boundary. Therefore, significant dislocation motion through the grain is facilitated and lead to a larger pile-up at the $\Sigma 3$ twin boundary such that the generated micro-stress is localized.

For evaluating intergranular cracking Schmid and Taylor factor analyses were conducted. These analyses revealed that crack propagation along non $\Sigma 3$ twin boundaries

in hydrogen is facilitated by a high Schmid factor of the adjacent grains and this is consequently accompanied by a low Schmid factor mismatch, which was not observed for non $\Sigma 3$ twin boundaries in helium. Though hydrogen did not alter the fraction of cracking occurring on random grain boundaries compared to twin boundaries, there may be an influence of hydrogen on the random grain boundaries which are susceptible to cracking.

In terms of strain localization at a grain boundary, as indicated by the Taylor factor mismatch, no significant trend was observed.

In the case of an irradiated 316L in an annealed condition the Taylor factor distribution was divided into three groups, low (L), medium (M), and high (H) Taylor factors by West et al. to analyze all grain boundaries, twins and non-twins [73,74]. It was then shown that grains with high Schmid and low Taylor factors showed multiple activated slip systems whereas grains with a low Schmid factor and a high Taylor factor exhibited only one set of slip traces. In the latter less slip systems are orientated favorably having a high and similar shear stress. Therefore, slip discontinuity was observed along grain boundaries between grains with low Schmid factors and high Taylor factors which act as crack initiation sites. In grains with a low Schmid factor and a high Taylor factor with one or few active slip systems slip cannot be easily transferred through the grain boundary which causes dislocations to pile up and leads to intergranular cracking. Especially, grain boundaries with a high Taylor factor mismatch LM and LH due to their slip discontinuity are susceptible to cracking. [73,74]

In terms of the Schmid factors of grains adjacent to cracks, the results in this thesis correspond to those of West, et al. for the cracking of random grain boundaries in specimens tested in helium but not for specimens tested in hydrogen. For specimens tested in inert environments short crack growth may require grains with one or few

active slip systems and boundaries across which slip cannot be easily transferred. Hydrogen may allow for cracking on boundaries that do not meet this requirement. The stresses at dislocation pile-ups at boundaries with multiple active slip systems could be relieved through cross-slip, but by restricting cross-slip hydrogen may cause cracking to occur despite the presence of multiple active slip systems.

No significant difference in α' -martensite due to hydrogen was observed. The main reason is the rather high nickel content that leads to greater austenite stability so that even with hydrogen no α' -martensite was formed. Pegues et al. showed that α' -martensite formation is predominately dependent on the crack length [58]. The α' -martensite increase is related to the growing plastic zone at the crack tip causing austenite-martensite formation [75]. Researchers have also studied the hydrogen distribution at twin boundaries in austenitic stainless steel by scanning Kelvin probe force microscopy with hydrogen pre-charged specimens. Only in the presence of α' -martensite was an accelerated hydrogen diffusion rate observed. [76] In the case of testing in external hydrogen, accelerated diffusion of hydrogen through α' -martensite likely plays an especially minor role because unlimited hydrogen is available for diffusion at the exposed specimen surface.

Based on the results presented here it is possible that an improvement of the fatigue life-time could be achieved by reducing the fraction of twin boundaries. The fraction of twin boundaries can be reduced by reducing the grain size. For tensile testing of a high Mn TWIP steel with internal hydrogen Bai et al. show grain refinement reduces the hydrogen influence [66]. In addition, grains with a low Schmid factor would have a beneficial effect on the fatigue lifetime as well. This could be achieved by applying a texture, e.g. by cold-working.

6.3 Results martensitic stainless steel (X3CrNiMo13-4)

6.3.1 The influence of hydrogen on the fatigue short crack sites in martensitic stainless steel

As a reference for the bulk martensitic microstructure an area of $550\text{ }\mu\text{m} \times 550\text{ }\mu\text{m}$ (624,938 data points) was analyzed with EBSD prior to testing. The undistorted lath martensite bulk microstructure is displayed in Figure 6.3.1 with indexed boundaries as an a) IPF map and b) image quality map. The boundaries are highlighted referring to the scheme in Figure 5.8.1 where PAG boundaries are white, low angle packet boundaries are dark green, high angle packet boundaries are light green, boundaries in the range of 50° to 57° are yellow, block boundaries are blue, and lath boundaries are red.

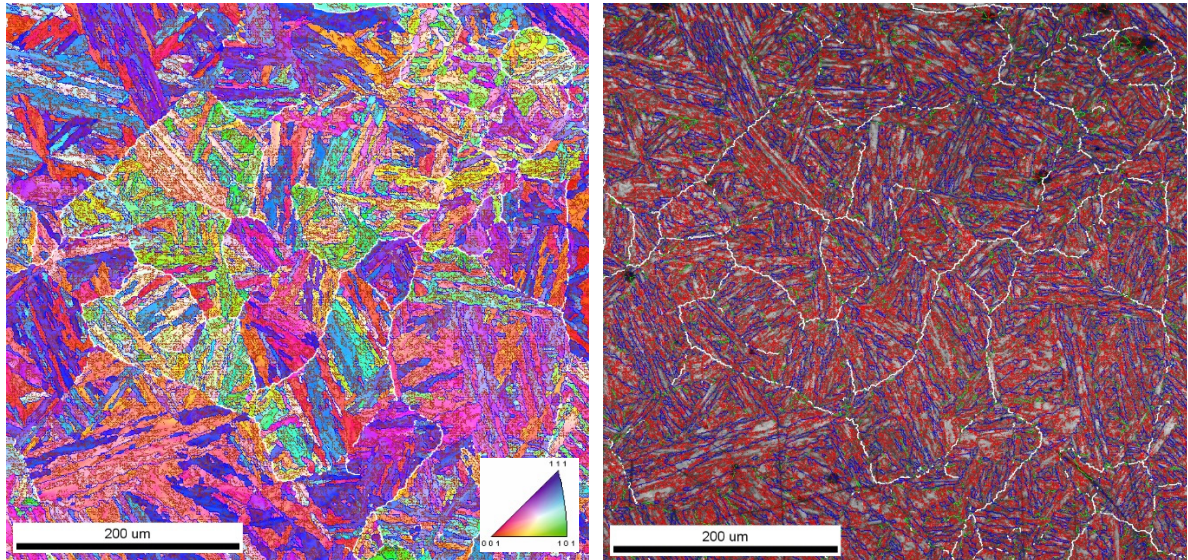


Figure 6.3.1: Martensitic bulk microstructure with indexed boundaries prior to testing: white = PAG boundary, dark green = low angle packet boundary, light green = high angle packet boundary, blue = block boundary, red = lath boundary a) IPF map, b) Image quality map

To analyze the bulk martensitic boundary microstructure a grain boundary misorientation angle distribution as a length fraction was generated and is shown in Figure 6.3.2. The lack of data for the 0° to 2° range is due to the cleaning of the raw data as described in chapter 5.8. Obviously, the greatest amount of boundaries are lath boundaries in the range between 2° to 10° . There are only a few boundaries in the low angle (10° - 21°) and the high angle (47° - 50°) range of the packet boundaries. The amount of boundaries in

the mixed high angle packet/block boundary range (50° - 57°) and block boundaries (57° - 62°) is significantly greater than the amount of low angle and high angle packet boundaries but not as numerous as the lath boundaries. The PAG boundaries in a range of 21° to 47° are by far the least.

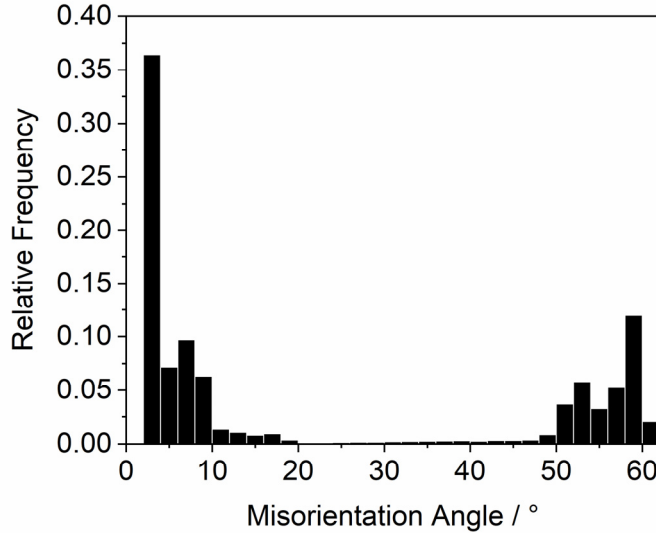


Figure 6.3.2: Grain boundary misorientation angle distribution as a length fraction of the martensite bulk microstructure prior to testing

Total crack lengths of 1945 μm formed in hydrogen and of 2051 μm formed in helium were analyzed to compare the crack sites in the martensitic stainless steel. These crack lengths are derived from 9 unique hydrogen and 13 unique helium short cracks and form the basis of the short crack investigation. The longest analyzed crack formed in hydrogen is 372 μm , and the shortest is 27 μm . In helium the longest investigated crack is 310 μm , and the shortest is 65 μm . The arithmetic average length of the hydrogen cracks is 218 μm and is 158 μm for the helium cracks.

An overview of the relative length fraction of the classified cracks in the martensitic stainless steel is given in Figure 6.3.3. The amount of trans-block cracks formed in hydrogen (over 40 %) is much greater than for helium cracks (25 %). In the case of intergranular cracking the fraction on low angle packet boundaries is the least in both environments. Only in helium were 2.4 % of cracks observed on these boundaries,

whereas in hydrogen no cracking could be observed on the low angle packet boundaries. Significant differences are observed for the non-random high angle packet and block boundaries in the range of 47° to 62° and inter-prior austenite grain boundary cracking between the two environments. 43 % of the total crack length in hydrogen is along prior austenite grain boundaries whereas the majority of the crack length in helium with 53 % is formed along non-random high angle packet and block boundaries. Only 15 % of the total crack length formed in hydrogen was determined to be on high angle packet and block boundaries.

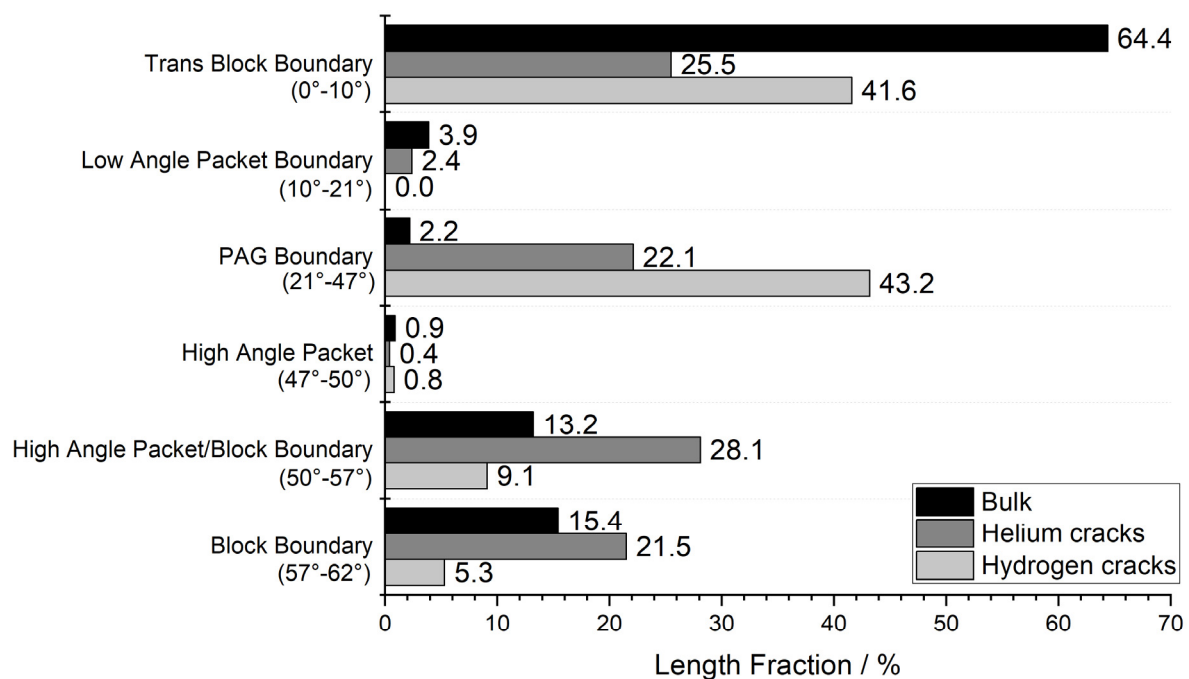


Figure 6.3.3: Boundary length fractions for the bulk microstructure and the short crack length fraction in the martensitic stainless steel X3CrNiMo13-4 based on inspection. Trans-block includes lath boundaries in the case of the bulk, according to Figure 5.8.1

Figure 6.3.4 focuses on the high misorientation angle packet and block boundaries and shows the relative total crack length for hydrogen and helium cracks. The fewest cracks for these types of boundaries follow high angle packet boundaries between 47° and 50° . About 2 % more of the hydrogen fatigue short cracks are on high angle packet bound-

aries than helium short cracks. The uncertain misorientation angle range that is dedicated to high angle packet and block boundaries shows a similar amount of cracking for the helium and hydrogen environments, 56 % and 60 %, respectively. For both environments, this is a higher ratio than the amount of high angle packet/block boundary in the bulk (45 %). Inter-block boundary cracking appears more often for helium cracks with 43 % than for hydrogen cracks with 35 %, whereas 52 % of the grain boundaries in the bulk microstructure are block boundaries. In comparison to the bulk microstructure it indicates that in both atmospheres more cracking may occur along packet boundaries than block boundaries. The actual lengths which are the basis for the relative investigation are listed in Table 6.3.

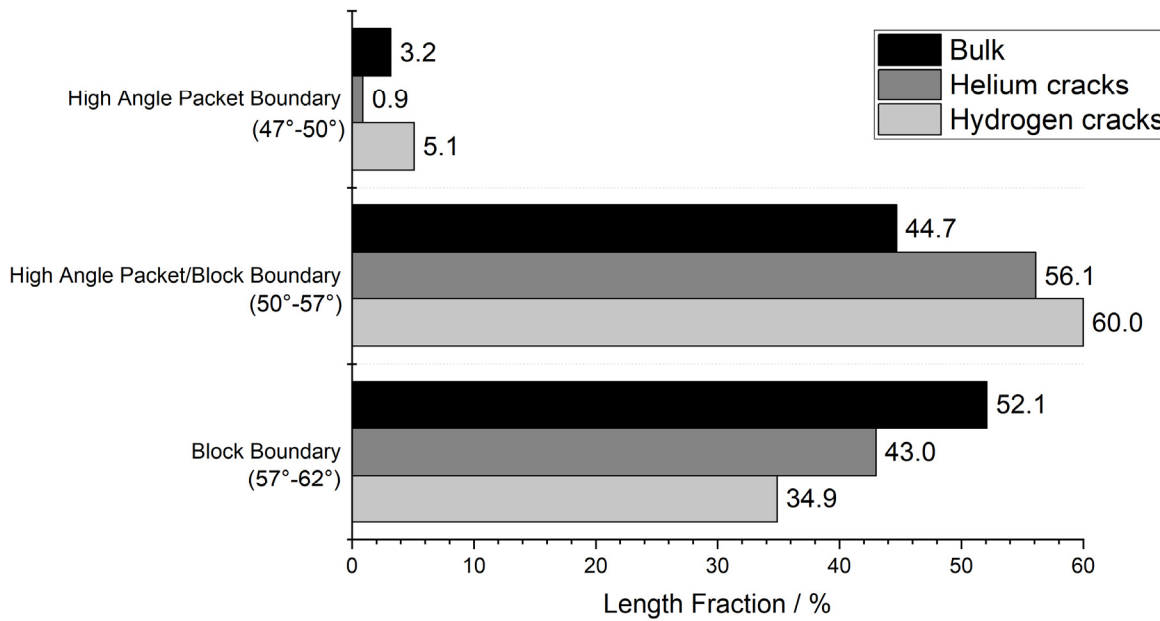


Figure 6.3.4: Boundary length fractions of the bulk microstructure and short fatigue crack length fraction in the martensitic stainless steel X3CrNiMo13-4

Table 6.3: Absolute Values of the Bulk Microstructure and the Investigated Short Crack Lengths in the Martensitic Stainless Steel X3CrNiMo13-4

	Bulk		Hydrogen		Helium	
	mm	%	µm	%	µm	%
Total crack length	-	-	1945	100	2051	100
Total length lath boundary / Trans-block cracks	149	64.4	809	41.6	523	25.5
Total length low packet boundary /ILP cracks	9.18	3.9	0	0.0	49	2.4
Total length prior austenite grain boundary / cracked length IPAG	5.13	2.2	841	43.2	453	22.1
Total length high packet boundary / cracked length IHP	2.21	0.9	15	0.8	9	0.4
Total length high packet/block boundary / cracked length IHP/IB	30.6	13.2	177	9.1	489	28.1
Total length block boundary / cracked length IB	35.7	15.4	103	5.3	527	21.5

Figure 6.3.5 illustrates a comparison of the short crack sites of the martensitic stainless steel formed in a) hydrogen and b) helium gas atmosphere by the respective grain boundary misorientation angle distribution. Generally, both bar graphs indicate that cracking occurs at any misorientation angle. In helium the highest peaks in the cracked grain boundary misorientation angle distribution with 9 % of the total cracks is in the inter-block range close to 60° . In hydrogen the short cracks grow more in a trans-block or inter-lath manner indicated by a high peak about 10 % in the 2° to 4° range. Furthermore, more PAG boundary cracking occurred in hydrogen than helium.

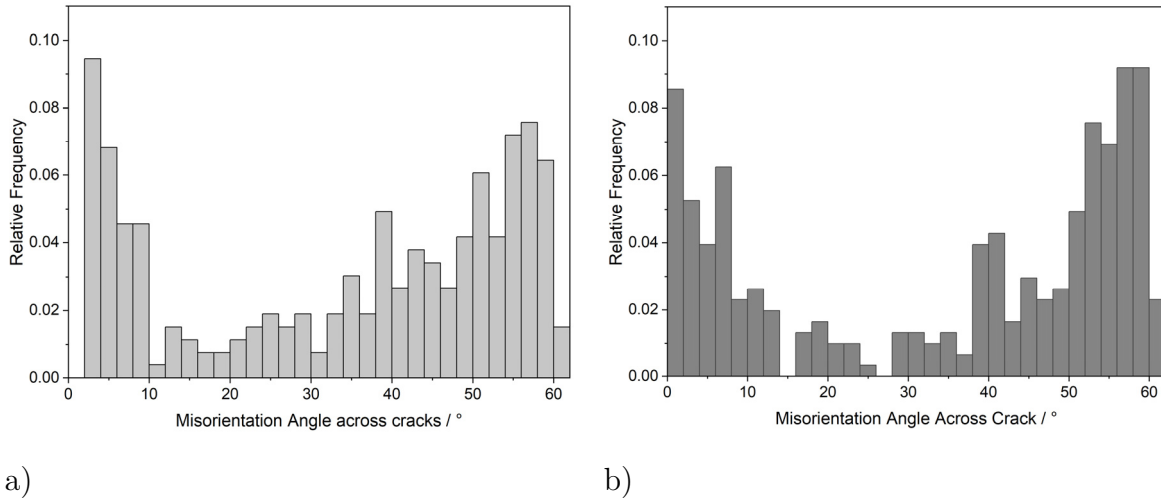


Figure 6.3.5: Misorientation angle distribution across all short cracks in the martensitic stainless steel as number fraction a) in hydrogen gas atmosphere, b) in helium gas atmosphere

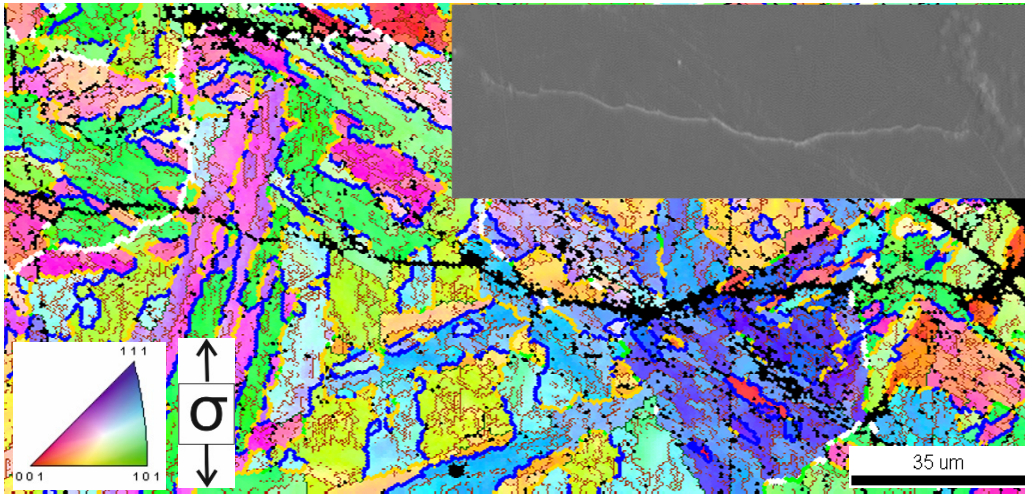


Figure 6.3.6: Exemplary hydrogen short fatigue crack in the martensitic stainless steel X3CrNiMo13-4 with 195 µm as an IPF map and SEM image of the forward-scattered electron detector; Boundaries: white = PAG boundary, dark green = low angle packet boundary, light green = high angle packet boundary, blue = block boundary, red = lath boundary

Figure 6.3.6 illustrates an exemplary hydrogen short fatigue crack in the martensitic stainless steel. For only a short length fraction it follows a prior austenite grain boundary here.

Analysis of the crack paths in the martensitic stainless steel concerning the linearity by the average fractal dimension gives a value of 1.002 for the hydrogen fatigue short cracks

and a value of 1.014 for the helium fatigue short cracks. As the fractal dimension of the hydrogen cracks is closer to one, the hydrogen cracks are more linear than the helium cracks. This linearity difference is due to the increased intergranular cracking behavior for testing in the helium gas atmosphere.

6.3.2 Crack initiation sites and microstructurally short cracks in martensitic stainless steel under hydrogen influence

One significant difference in crack initiation is the amount of initiated microstructurally short cracks per specimen. In hydrogen gas atmosphere sometimes only one crack initiated per specimen, whereas in the helium gas atmosphere numerous fatigue short cracks >100 per specimen initiated. The hydrogen cracks predominately started at the edge between the round and the plane surface areas in the gauge section and almost exclusively propagated in the round part of the specimen. The mean average of cracks per specimen for testing in the hydrogen gas atmosphere is 2.75. Almost all helium cracks initiate with an angle close to the maximum shear stress (45° to the tensile axis). In the IPF map of a microstructurally short helium crack in Figure 6.3.7 the white arrows point to cracks that have initiated along block boundaries which make an angle of close to 45° with respect to the tensile axis.

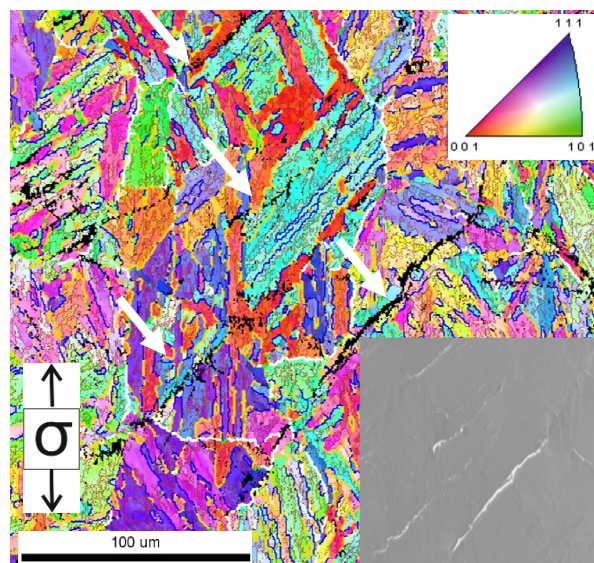


Figure 6.3.7: Microstructurally short helium fatigue cracks initiating with an angle to the tensile axis of close to 45° , IPF and SEM forward scattered electron detector, highlighted boundaries according to the classification in chapter 5.8

In contrast, the microstructurally short hydrogen fatigue cracks initiate predominantly perpendicular to the tensile axis as in Figure 6.3.8. In the previous section it was shown that a remarkable 43 % of the crack length in hydrogen is intergranular cracking along PAG boundaries. Moreover, the microstructurally short cracks in this study appear to exclusively initiate on PAG boundaries. This observation is supported by the fact that all 9 investigated short cracks, not only the microstructurally short cracks, include at least one cracked part along a PAG boundary. No other cracking site (trans-block, inter low packet, etc.) was present in every short crack.

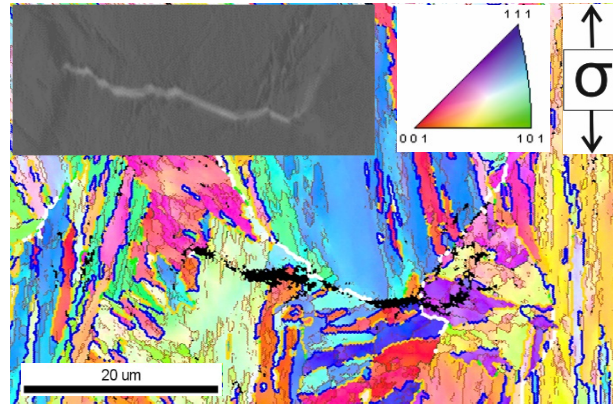


Figure 6.3.8: Example hydrogen microstructurally short fatigue crack in the martensitic stainless steel with a crack length of 28 μm , IPF and SEM forward scattered electron detector image, highlighted boundaries according to the classification in chapter 5.8; boundaries: white = PAG boundary, dark green = low angle packet boundary, light green = high angle packet boundary, blue = block boundary, red = lath boundary

A quantitative analysis approach is displayed in chapter A4 in the appendix. The cracking classes according to 5.8 vs. the individual crack lengths of each short crack are shown for hydrogen and helium cracks, respectively.

6.3.3 Fractography of martensitic stainless steel

Observing the cracks only at the surface of the smooth specimen does not capture the processes underneath the surface. To gain a better insight on the cracking within the martensitic stainless steel the fracture surfaces were evaluated in the SEM. Figure 6.3.9 provides SEM images at different magnifications of the fracture surface generated by

testing in hydrogen a), c), e) and helium gas atmosphere b), d), f). An overview of the entire fatigue fracture surface is shown in a) and b). The crack initiation sites are shown in Figure 6.3.9c) and d) and regions of long crack growth are shown in Figure 6.3.9e) and f)

The overview of the specimen tested in helium, Figure 6.3.9 b), clearly shows multiple crack initiation sites on the specimen surface indicated by arrows. On the other hand, the fracture surface of the specimen tested in hydrogen, Figure 6.3.9 a), shows only one crack initiation site on the specimen surface, which is close to the three o'clock position. Shortly, before the overload area in the hydrogen fracture surface Figure 6.3.9 a) a large secondary crack is clearly visible. Branching secondary cracks were exclusively observed in the hydrogen fracture surface and predominately in the range of a long crack and not in the short crack length scale. A brittle fracture mode with larger facets is shown in the hydrogen long crack growth region e) while a more ductile fracture mode is present for the helium long crack growth region in f). It should be mentioned that unlike for the helium long crack region no striations can be observed in the hydrogen long crack region which indicates a rapid crack growth rate in the long crack range.

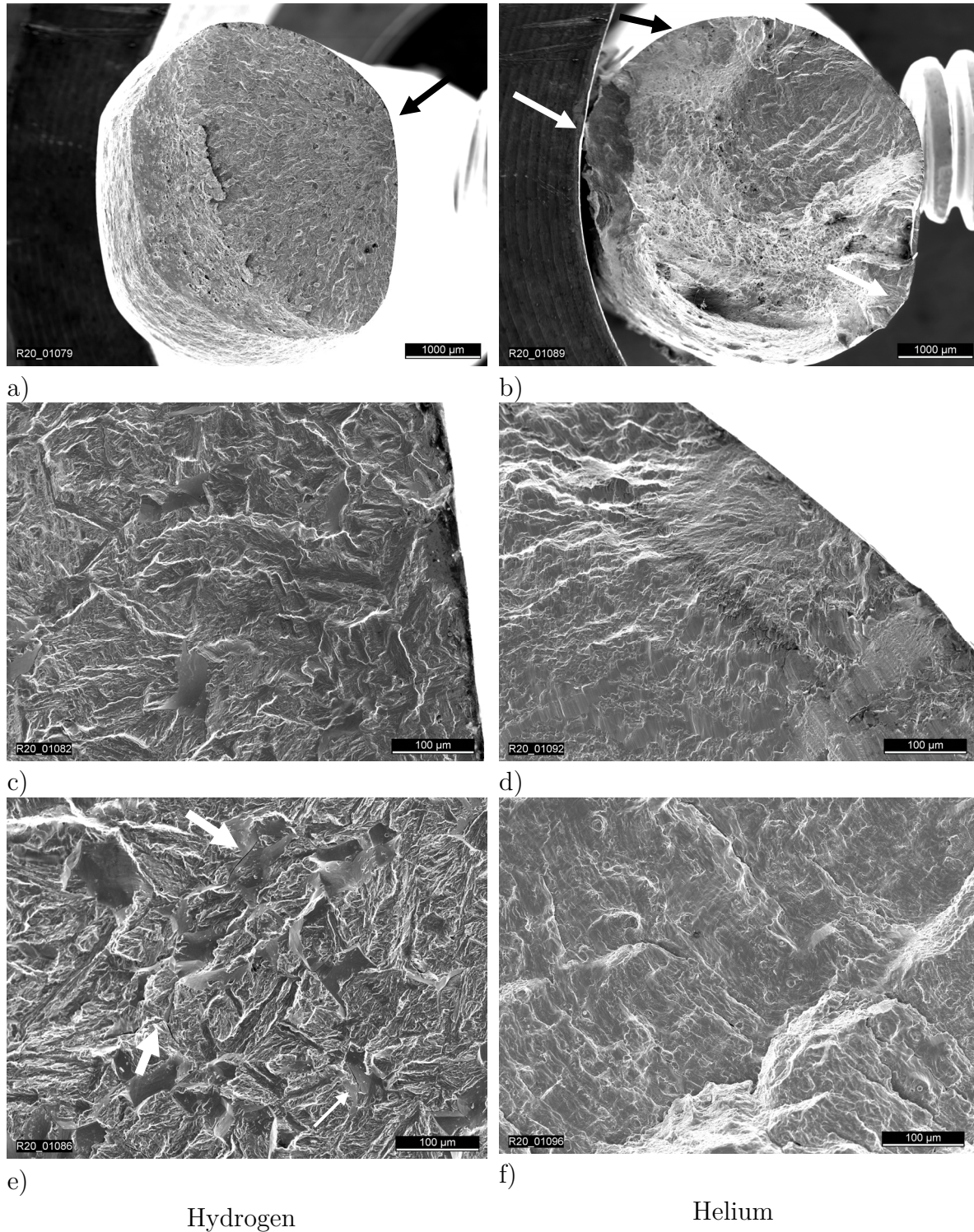


Figure 6.3.9: SEM images of the fatigue fracture surface of the martensitic stainless steel X3 tested with 1 Hz at $R=-1$ at room temperature in hydrogen and helium gas at 10 MPa, a) overview H2 surface, b) overview He surface, c) initiation site H2, d) initiation site He, e) long crack growth area H2, white arrows indicate secondary cracks, f) long crack growth area He

6.4 Discussion martensitic stainless steel (X3CrNiMo13-4)

The majority of the fatigue short cracks in hydrogen in the martensitic stainless steel followed the prior austenite grain boundaries. In contrast the helium fatigue short cracks predominately propagated on high misorientation angle ($>47^\circ$) packet and block boundaries. In both environments more cracking on PAG boundaries than block boundaries relative to the bulk microstructure was observed. Compared to the high number of low angle lath boundaries in the microstructure, minimal transgranular cracking across blocks was observed. Regarding the high angle misorientation boundaries, in both hydrogen and helium gas atmospheres the ratio of short cracks on high angle packet boundaries to short cracks on block boundaries was greater than the ratio of those boundaries in the bulk microstructure. In comparison to the bulk microstructure the susceptibility to grain boundary cracking in helium and hydrogen increased in the following order: lath, block/packet, PAG.

In general, the sequence leading to intergranular cracking in brittle materials is as follows: First, cyclic straining causes dislocations to pile-up along slip planes at the grain boundary. Second, a crack is nucleated on the grain boundary due to the shear stress at the head of the dislocation pile-up. [6] Crack nucleation is mostly dependent on the number of dislocations in the pile-ups and the grain boundary energy, or more precisely the cohesive forces of the grain boundary. Therefore, the following discussion will focus on these two aspects. It shall be noted here that the discussion will not distinguish between crack nucleation and short crack propagation specifically. According to Tetelman [77] the criterion for crack nucleation (Eq. 7) and initial crack growth (Eq. 8) are very similar. τ_N and τ_i are the shear stress and the shear stress caused by friction respectively. n is the number of dislocation in a slip plane whereas b is the burgers vector. The work to generate a new fracture surface is defined as γ_s , the microstructural unit is represented by half the grain size, and G is the shear modulus.

$$(\tau_N - \tau_i)nb \cong 2\gamma_s \quad (7)$$

$$nb \cong (\tau_N - \tau_i) \frac{d}{G} \quad (8)$$

Equation 7 basically states that the crack will nucleate when the energy due to the applied shear stress acting on the piled-up dislocations reaches the cohesive energy of the boundary. Hence, intergranular cracking can be facilitated by increasing the number of piled-up dislocations at a grain boundary or by weakening the cohesive forces of the boundary itself. The major difference to Eq. 8 is the dependency on half of the grain size $2d$. Both equations reveal the importance of the dislocation-grain boundary interaction.

Based on the mechanisms for plasticity-induced crack initiation and growth, it is important to understand the interplay between dislocation slip and grain boundaries in martensitic steel. In terms of grain boundary character Ohmura et al. investigated the dislocation grain boundary interactions in martensitic steel through *in situ* nanoindentation in a transmission electron microscope in the absence of hydrogen. A low angle grain boundary (probably a lath boundary) and a high angle/block boundary were compared. The emitted dislocations beneath the indenter first piled up and then upon exceeding a critical stress were emitted in the adjacent grain for the low angle grain boundary. In the case of the high angle block boundary the dislocations were absorbed. [52]

Shibata et al. analyzed the dislocation mobility across block boundaries in the absence of hydrogen [78]. The authors bend tested micro-sized cantilevers-beam specimen including a block boundary with only subblock material. In the vicinity of the block boundary no slip band localization was observed.

According to Morsdorf et al. the deformation response in martensite is a superposition of slip system orientation, interface orientation and initial yield strength distribution due to lath size, defect density and carbon distribution variations. In air Morsdorf et al.

observed significant strain localization especially at high angle block and packet boundaries in tensile and bending tests. This result is in agreement with results from Du et al. who also showed that significant plasticity occurs at the investigated lath, sub-block, and block boundaries by performing uniaxial micro-tensile tests [79]. It shall be noted here that Morsdorf et al. identified no specific strain localization at prior austenite grain boundaries. Therefore, the authors propose that flat interfaces are favored for interface plasticity. [80]

The work to generate a new fracture surface γ_s , in Eq. 7 is inversely related to the grain boundary energy. In other words, a grain boundary with a greater interfacial energy normally requires less work for fracture. The grain boundary energy is commonly considered to be based on the misorientation angle as shown in Figure 2.1.1. Especially, in the case of lath martensite the relationship between misorientation angle and grain boundary energy appears to be more complex. This presumption is supported by a numerical study by Ratanaphan et al. calculating grain boundary energies in bcc metals using the embedded atom method [81]. The authors could show no dependency of the grain boundary energy either on the misorientation angle or Σ , the inverse density of the coincident lattice sites. Subsets of the data lead to the hypothesis that the grain boundary energy is dependent on the index plane such that two adjacent low index planes result in a low grain boundary energy. These results support the hypothesis by Rohrer that the grain boundary energy is the total energy of the adjoining surfaces subtracting the binding energy [82,83]. The block boundary is between two blocks sharing one common low index $\{110\}$ habit plane and therefore has a low grain boundary energy, which explains the lower incidence of cracking of the block boundaries for both environments compared to the number of bulk boundaries in the bulk microstructure.

The following paragraphs focus on studies with the effects of hydrogen on martensite. Nagao et al. investigated intergranular PAG cracking in a lath martensite with internal hydrogen [84]. TEM observations on FIB micrographs obtained from underneath the

fracture surface revealed intense plastic deformation along lath boundaries and indicated cracking along PAG boundaries. The authors state that intergranular cracking of PAG boundaries is caused by two complementary mechanisms: First, piled-up dislocations impose a stress concentration at the boundary and second a high amount of accumulated hydrogen along the high angle misorientation boundaries reduces the cohesive atomic bonding. These findings are comparable to hydrogen increasing the number of piled-up dislocations n and decreasing the cohesive force of the grain boundary, thereby decreasing γ_s , according to Eq. 7.

For in situ tensile testing in gaseous hydrogen only one source has shown both quasi-cleavage cracking and numerous secondary cracks along PAG boundaries in the fracture surface [85]. PAG boundary cracking has been observed with internal hydrogen [50,84,86]. A study by Singh et al. concerning internal hydrogen defined all PAG boundaries as grain boundaries with a misorientation angle greater than 15° . The authors observed in a bainite-ferrite structure a mixed intergranular-transgranular cracking up to a crack length of 5 to 6 grains, which can be considered fatigue short cracks. Longer cracks predominately showed transgranular cracking; however, in the short crack range PAG cracking was prevalent. Inclusions also appeared to be favored crack initiation sites. [86]

For PAG boundaries (there defined as grain boundaries $>15^\circ$) a hydrogen trap binding energy of 47.4 kJ/mol [87] has been reported as well as a hydrogen trap binding energy in the range of 16.7 to 36.4 kJ/mol for lath boundaries (there defined as grain boundaries $<15^\circ$) [23,88–91]. Nagao et al, determined the hydrogen trap binding energies for PAG boundaries and lath boundaries for his investigated materials (A500, A550, B500, B550, B600) to be 57.4 and 25.7 kJ/mol, respectively. These values are in good agreement with a qualitative analysis by Ishikawa using silver particles to mark hydrogen within the material [92]. However, the conclusions drawn from these studies are too superficial to explain the results presented in this thesis because no distinction is made between

the different grain boundaries categories in martensite with misorientations greater than 15° (block, high/low-angle packet or an actual PAG boundary). As mentioned above in the results gained by Nagao et al. block boundaries which have the greatest misorientation angle would be expected to be the favored intergranular cracking sites in hydrogen.

In the present study it was shown that the frequency of observed crack sites shifts from block boundaries to PAG boundaries in the hydrogen environment. This finding evokes the question: What is special about a PAG boundary that increases susceptibility to fatigue cracking in hydrogen if it is not the misorientation angle?

Generally, hydrogen decreases the repulsive forces between dislocations which leads to relatively more dislocations piled-up at the boundary and the dislocations in the pile-ups will facilitate cracking at a boundary. Activation of slip on the other side of a grain boundary can allow for slip transfer and additional plasticity without further increasing the number of dislocations the pre-existing pile-up. Additionally, the bcc lattice with its 48 possible slip systems may normally offer at least one favored slip system to transfer the slip from one grain through the grain boundary to the adjacent grain, but if hydrogen localized slip onto a fewer number of active slip systems, then slip transfer may be restricted. This phenomenon is illustrated schematically for prior austenite and block boundaries in hydrogen and helium environments in Figure 6.4.1.

Focusing on the hydrogen effect and assuming that the dislocation movement is facilitated along the active slip plane, the slip transfer through the PAG boundary seems to be impeded compared to the block boundary. More dislocations are piled-up and the resulting shear stress increase at the head of the pile-up leads to intergranular cracking at the PAG boundary. The reason for this behavior is definitely not the misorientation angle as PAG boundaries can have any misorientation angle up to the maximum crystallographically possible.

Slip transfer may be easier for boundaries that were formed in the austenite-martensite transformation process such as block boundaries. Adjacent blocks share common habit planes, which is assumed to be being beneficial for slip transfer through the block boundary; therefore, dislocations would be less piled-up at the block boundary and lead to less shear stress and less cracking at the block boundary.

Unlike all other martensitic boundaries, the PAG boundaries are outstanding due to the curved boundary interface which is not developed in the austenite-martensite transformation. As the PAG boundary is curved and therefore a three-dimensional defect it probably affects the dislocation movement different than the flat boundaries developed during the martensite formation. Due to the either convex or concave interface the activation of a slip plane in the adjacent grain could be impeded.

Finally, the only boundary in the martensitic microstructure that was not formed in the austenite-martensite transformation process is the PAG boundary. In general, it is the primary location in the microstructure where impurities segregate which can aid in crack nucleation and propagation by weakening the grain boundary.

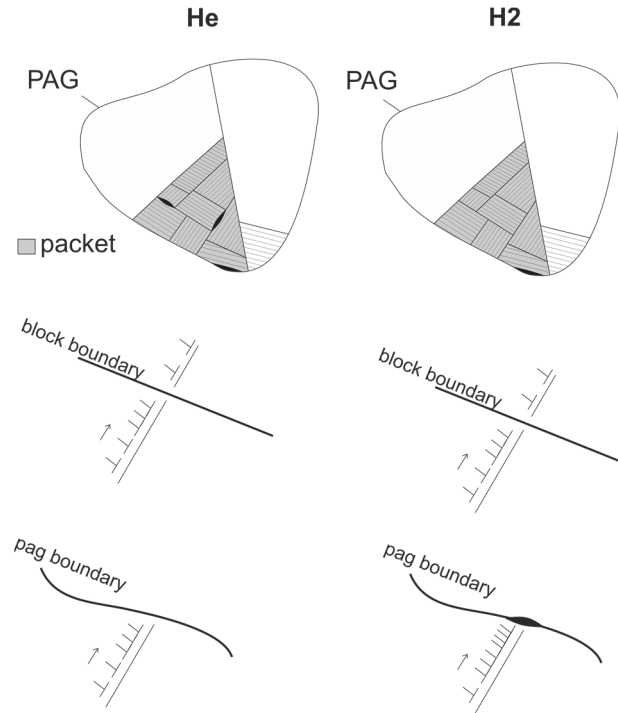


Figure 6.4.1: Schematic of fatigue cracking sites for helium and hydrogen gas atmosphere

To improve fatigue properties of martensitic steel exposed to hydrogen grain boundary engineering may be applied. Increasing the amount of PAG and thereby decreasing the prior austenite grain size would reduce the slip band length and decrease the concentration of impurities. This assumption is in good accordance with experimental results from tensile tests in gaseous hydrogen using two materials only differing in grain size. The specimen with the coarse PAG condition was less resistant to hydrogen-induced fracture than the specimen with the smaller PAG size. [13,85]

As a consequence of the grain refinement the number of packet and block boundaries are increased which leads to an increase in total grain boundary area. Subsequently, dislocation movement is impeded by the numerous grain boundaries which has a strengthening effect on the material in accordance with the Hall-Petch relationship. [11, 93–98]

7 Summary

This study evaluates the influence of a 10 MPa hydrogen gas atmosphere on the fatigue short crack initiation and propagation in two stainless steels with different microstructures: a metastable austenitic stainless steel X2CrNi19-12 and a martensitic stainless steel X3CrNiMo13-4. The reference medium was helium with a gas pressure of 10 MPa. The low cycle fatigue tests were performed with smooth specimens at room temperature with a frequency of 1 Hz and an R-ratio of -1. To enable surface inspection the specimen was flattened on two opposite sides and electropolished. The direct current potential drop method was applied to detect the presence of short cracks so that the experiments could be stopped before final failure. The path of short cracks with a range of lengths from 25 to 564 μm were evaluated by electron backscattered diffraction in a scanning electron microscope.

The austenitic stainless steel showed no significant difference in the fraction of cracking on $\Sigma 3$ twin boundaries and random grain boundaries when comparing the short cracks from the hydrogen and helium atmospheres. For both hydrogen and helium environments a higher ratio of cracking on $\Sigma 3$ twin boundaries to cracking on random grain boundaries was observed than for the ratio of those boundaries in the bulk microstructure. Cracks on random grain boundaries formed in the hydrogen environment grew along grains with a higher Schmid factor and smaller Schmid factor mismatch than cracks formed in the helium environment. No difference in the amount of α' -martensite along short cracks was detected between the hydrogen and helium environments. The high nickel content of this austenitic stainless steel may prevent hydrogen from activating cracking at different microstructural sites.

The amount of short cracks initiated in the hydrogen gas atmosphere per specimen (~ 2) was significantly lower than in helium (> 100). This difference indicates that the fatigue short crack propagation in hydrogen is substantially driven by the hydrogen at the

crack tip. In the specimen tested in helium numerous persistent slip bands were observed whereas in the specimen tested in hydrogen very few were visible.

In the martensitic stainless steel the majority of the hydrogen fatigue short cracks propagated on prior austenite grain boundaries, whereas the helium short cracks predominately grew along packet and block grain boundaries. The hydrogen short cracks initiated at prior austenite grain boundaries predominately perpendicular to the tensile stress and appeared with a smaller fractal dimension. The helium short cracks initiated at a plane close the plane of maximum shear stress. The effect of hydrogen on microstructural short crack sites was related to differences in dislocation accumulation and slip transmissibility at block and prior austenite grain boundaries.

8 Outlook

As the investigated austenitic stainless steel X2CrNi19-12 with a nickel content of 12.36 wt% showed no significant influence of the hydrogen gas atmosphere on the fatigue short crack growth, performing similar tests with an austenitic stainless steel with a lower nickel content that is more susceptible to hydrogen would be valuable. More information about the influence of hydrogen on the fatigue crack initiation and propagation could be achieved with a more susceptible steel. Furthermore, a lower nickel content would lead to less austenite stability and therefore the effect of hydrogen on strain-induced martensite formation during short fatigue crack propagation could be better evaluated. Differences in the amount and morphology of α' -martensite may provide a better understanding of the localization of plasticity due to hydrogen.

In the case of the martensitic stainless steel surprisingly minimal information about the different grain boundary energies could be found in literature. Only two experimental studies about dislocation movement across block vs. low angle boundaries could be found and only one computational study on the energetics of other boundaries such as packet or lath boundaries could be found. By testing specially designed micro specimens containing one or a few boundaries of a specific type could lead to a better understanding of the grain boundaries in air.

Furthermore, a more quantitative evaluation on microstructurally short cracks only would be valuable. Therefore, a different specimen geometry might be best. Due to the necessity of a smooth surface, an hourglass specimen might be a good choice. Reducing the area where a crack initiates such that the DCPD probes can be attached closer to the forming crack in order to improve the resolution of the electric resistance measurement and detect a crack at a small scale would aid in this analysis. For microstructurally small cracks, EBSD analyses can be performed on round specimens because when the

crack is very short and the curvature is minimal and would lead to a negligible deviation of the measured orientations in the SEM.

All investigations of the short cracks were performed on the specimen surface. However, crack propagation is not only a two dimensional process. The microstructure underneath the surface influences the crack propagation especially in the short crack regime. The investigation will be challenging to break open the short cracks or by removing material from the surface in a plain manner and with knowledge about the depth of the removed surface.

In this study almost all tests were stopped after detecting a short crack by DCPD and then the specimens were modified for further analysis by, for example, removing the threads, such that no further testing on those specimens could be performed. Only a few specimens were tested until failure. More comprehensive information about the crack propagation of long cracks and a detailed analysis of the fatigue life with regards to the fraction of the different crack stages could be gained by performing fatigue tests until failure.

Appendix

A1 Tensile curves of the investigated materials

The data shown here are all derived from a former research project [57].

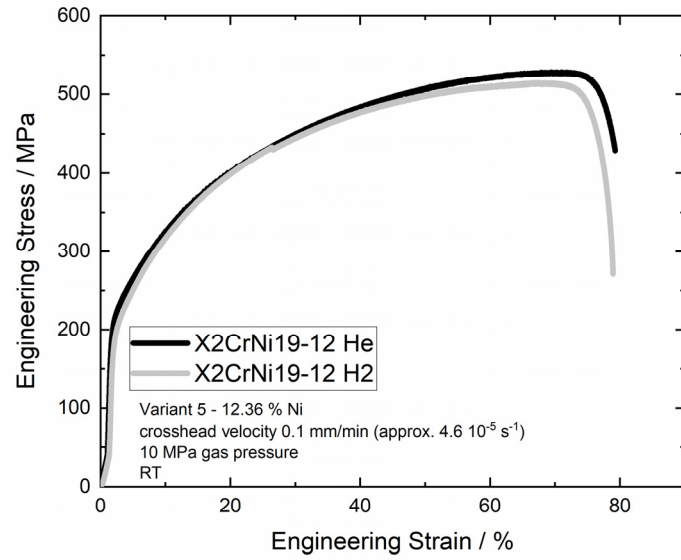


Figure A1.1: Stress strain curve of the metastable austenitic stainless steel X2CrNi19-12 in 10 MPa hydrogen and helium gas atmosphere at room temperature

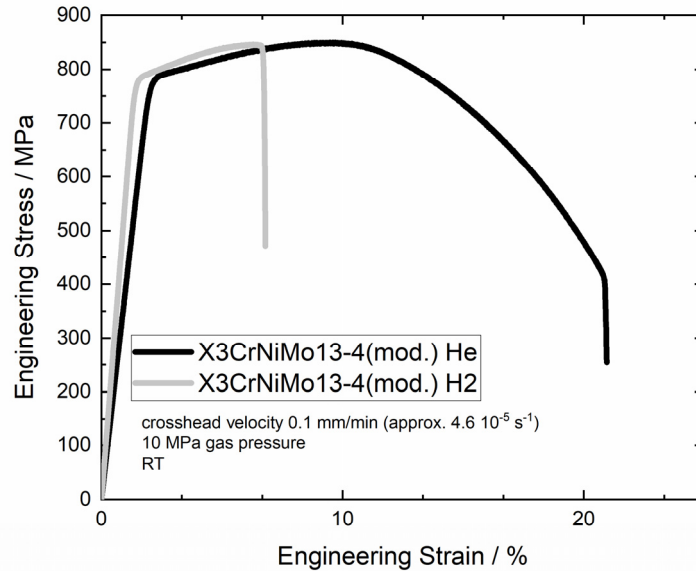


Figure A1.2: Stress strain curve of martensitic stainless steel X3CrNiMo13-4 (mod.) in 10 MPa hydrogen and helium gas atmosphere at room temperature

A2 Tension-tension fatigue properties X2CrNi19-12 of notched specimen

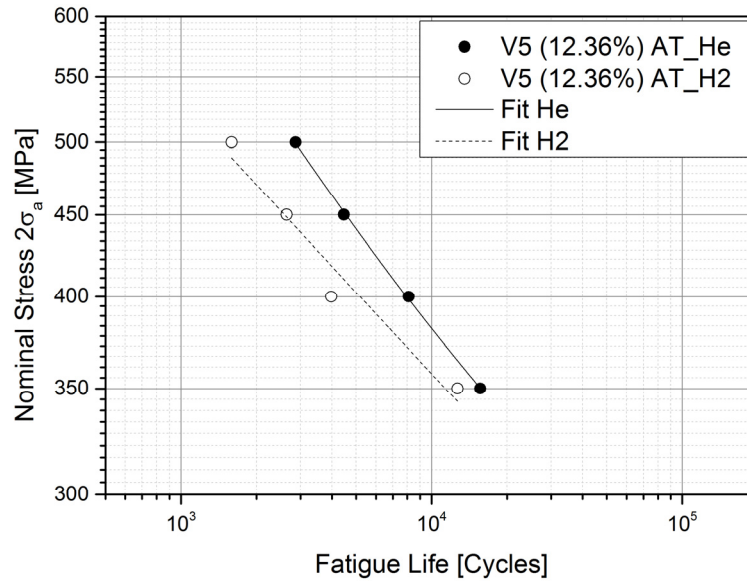


Figure A2.1: Notched fatigue life properties of the metastable austenitic stainless steel X2CrNi19-12 at ambient temperature, frequency 1 Hz, $R=0.1$, gas pressure 10 MPa [57]

A3 Strain softening behavior of the austenitic stainless steel X2CrNi19-12

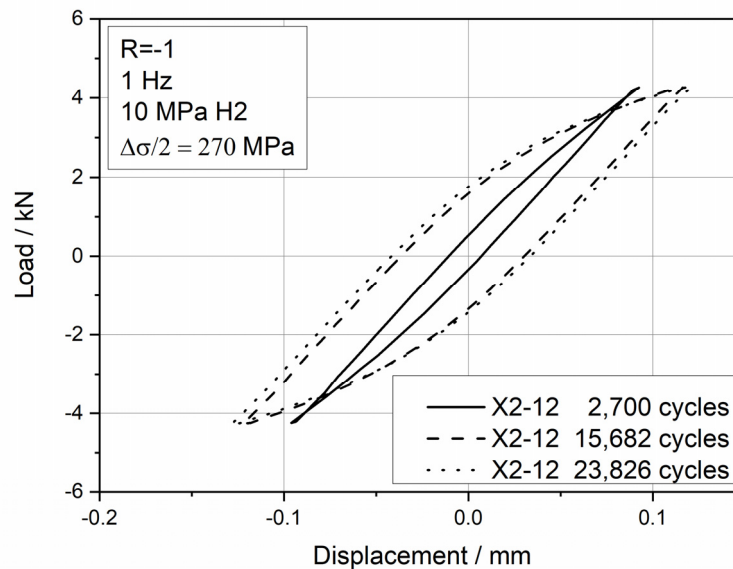


Figure A3.1: Load displacement change during the fatigue test duration of the metastable austenitic stainless steel X2CrNi19-12 at room temperature in 10 MPa hydrogen gas atmosphere at a constant stress amplitude of 270 MPa in tension-compression mode

A4 Electric potential of austenitic stainless steel

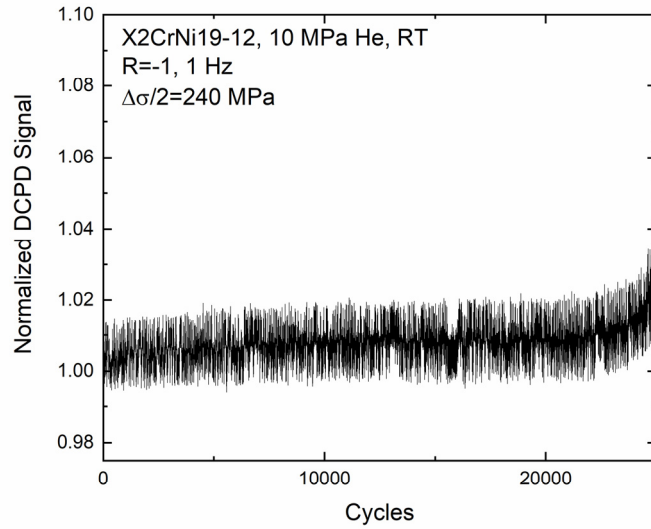


Figure A4.1: Electric potential of an austenite specimen during a fatigue test until failure in helium gas atmosphere with 10 MPa gas pressure, a test frequency of 1 Hz, a stress amplitude of $\sigma_a = 240$ MPa, and stress ratio of $R = -1$

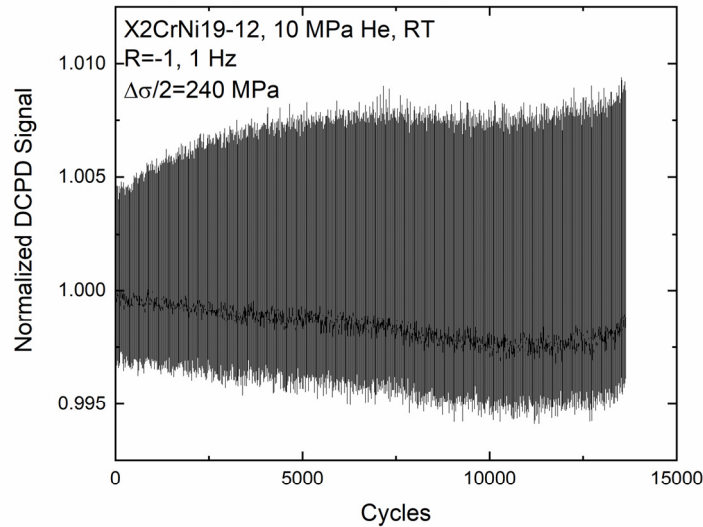


Figure A4.2: Electric potential of an austenite specimen during a fatigue test in helium gas atmosphere with 10 MPa gas pressure, a test frequency of 1 Hz, a stress amplitude of $\sigma_a = 240$ MPa, and stress ratio of $R = -1$, interrupted due to crack propagation

A5 Electric potential of the martensitic stainless steel

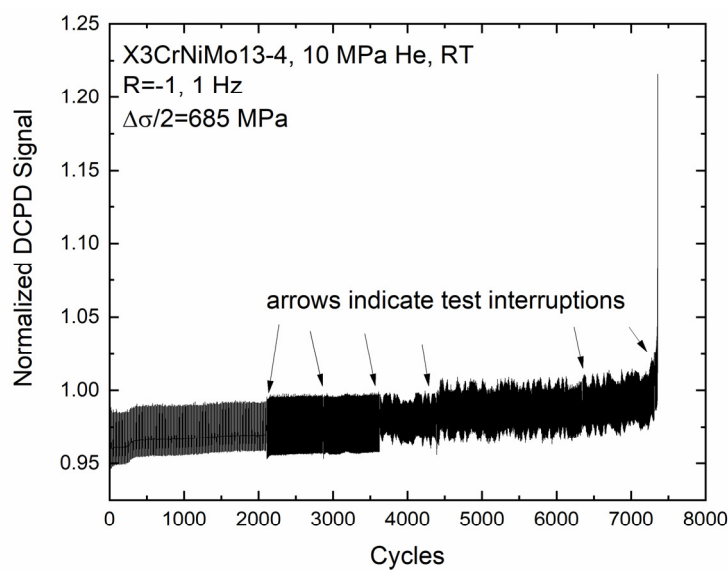


Figure A5.1: Electric potential of a martensite specimen during a fatigue test until failure in helium gas atmosphere with 10 MPa gas pressure, a test frequency of 1 Hz, a stress amplitude of $\sigma_a = 685$ MPa, and stress ratio of $R = -1$

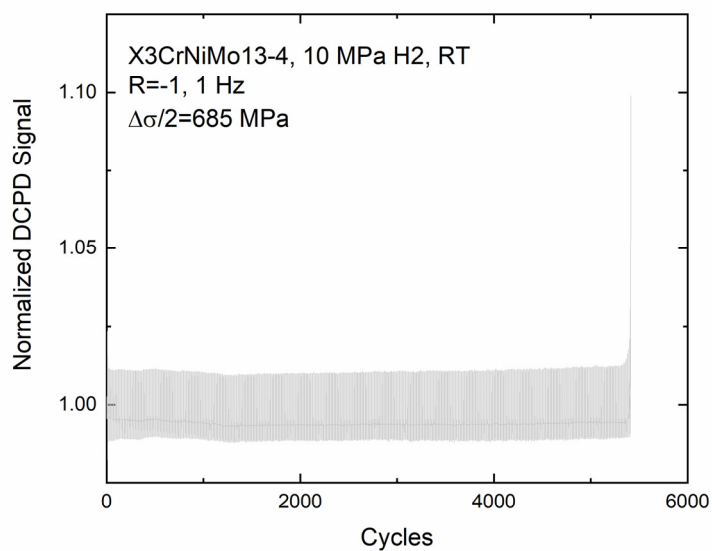


Figure A5.2: Electric potential of a martensite specimen during a fatigue test until failure in hydrogen gas atmosphere with 10 MPa gas pressure, a test frequency of 1 Hz, a stress amplitude of $\sigma_a = 685$ MPa, and stress ratio of $R = -1$

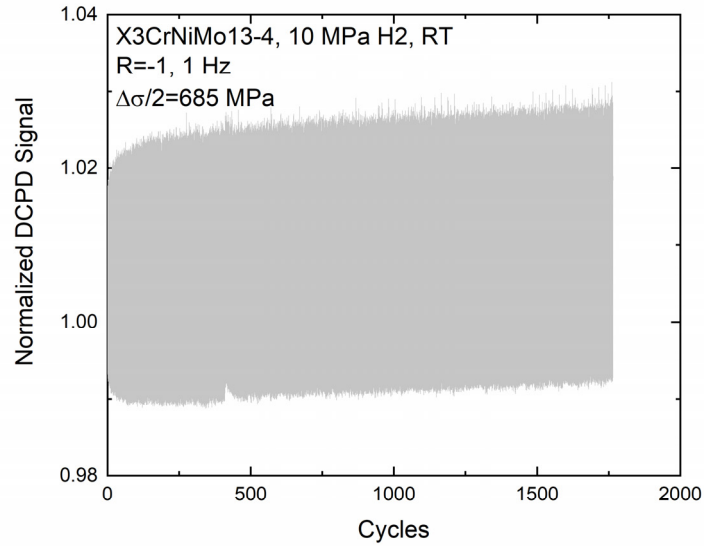


Figure A5.3: Electric potential of a martensite specimen during a fatigue test until failure in hydrogen gas atmosphere with 10 MPa gas pressure, a test frequency of 1 Hz, a stress amplitude of $\sigma_a = 685$ MPa, and stress ratio of $R = -1$

A6 Fractions of classified martensite grain boundaries

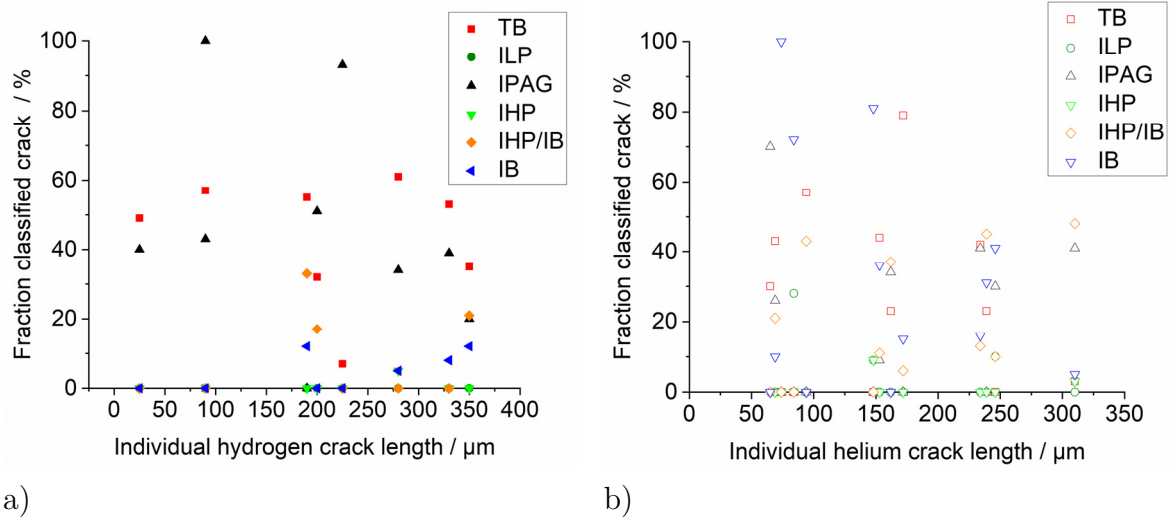


Figure A6.1: Fraction of each classified boundary crack in martensite for the X3CrNiMo13-4 in dependency of the individual crack length in compression tension at 1 Hz for a) hydrogen and b) helium gas atmosphere

References

- [1] M. Sterner, M. Jentsch, U. Holzhammer: Energiewirtschaftliche und ökologische Bewertung eines Windgas-Angebots Fraunhofer-Institut für Windenergie und Energiesystemtechnik (IWES) (2011).
- [2] Fuel Cell Works: FCW Exclusive: Tokyo Fell Cell Expo 2019 - 300,000 Ene-Farms, In Fuel Cell Works, retrieved May 21st 2020.
- [3] D.A. Porter, K.E. Easterling: Phase transformations in metals and alloys, 2nd ed., Chapman & Hall, London, 1997.
- [4] R. Abbaschian, L. Abbaschian, R.E. Reed-Hill: Physical metallurgy principles, ©2010, (2015)
- [5] L.E. Murr: Interfacial phenomena in metals and alloys, Addison-Wesley, London, (1975)
- [6] G.E. Dieter: Mechanical Metallurgy, 3rd ed., Mc Graw Hill Education, (2013)
- [7] G.I. Taylor: Twenty-Eighth May Lect, J. Inst. Met. (1938) 307–324.
- [8] E. Roos, K. Maile, M. Seidenfuß: Werkstoffkunde für Ingenieure: Grundlagen, Anwendung, Prüfung, 6th ed., Springer Vieweg, Berlin, Germany.
- [9] T. Angel: J Iron Steel Inst (1954) 165.
- [10] T. Hirayama, M. Origima: J., J. Jpn. Inst. Met. (1970) 507.
- [11] T. Inoue, S. Matsuda, Y. Okamura, K. Aoki: The Fracture of a Low Carbon Tempered Martensite, Trans. JIM 11 (1970) 36–43.
- [12] S. Morito, H. Tanaka, R. Konishi, T. Furuhashi, T. Maki: The morphology and crystallography of lath martensite in Fe-C alloys, Acta Materialia 51 (2003) 1789–1799.

-
- [13] J. Hidalgo, M.J. Santofimia: Effect of Prior Austenite Grain Size Refinement by Thermal Cycling on the Microstructural Features of As-Quenched Lath Martensite, *Metall and Mat Trans A* 47 (2016) 5288–5301.
- [14] L. Sandoval, H. M Urbassek, P. Entel: The Bain versus Nishiyama–Wassermann path in the martensitic transformation of Fe, *New J. Phys.* 11 (2009) 103027.
- [15] G.V. Kurdjumov, G. Sachs: Über den Mechanismus der Stahlhärtung, *Z Phys* (1930) S.325-43.
- [16] Z. Nishiyama: X-ray investigations of the mechanism of the transformation from face-centered cubic lattice to body-centered cubic, *Sci Rep Tohoku Imp Univ* (1934) S.637-64.
- [17] H. Schuhmann: Einführung in die Theorie der Gittertransformationen metallischer Werkstoffe, VEB Deutscher Verlag für Grundstoffindustrie, Leipzig, (1980) S.165.
- [18] B. Sonderegger, S. Mitsche, H. Cerjak: Martensite laths in creep resistant martensitic 9–12% Cr steels — Calculation and measurement of misorientations, *Materials Characterization* 58 (2007) 874–882.
- [19] J.K. MacKenzie: Second paper on statistics associated with the random disorientation of cubes, *Biometrika* (1958) 229–240.
- [20] T. Karthikeyan, M.K. Dash, S. Saroja, M. Vijayalakshmi: Estimation of martensite feature size in a low-carbon alloy steel by microtexture analysis of boundaries, *Micron* (Oxford, England 1993) 68 (2015) 77–90.
- [21] C. Borchers, T. Michler, A. Pundt: Effect of Hydrogen on the Mechanical Properties of Stainless Steels, *Advanced Engineering Materials* (2008) 11–23.
- [22] A.A. Pisarev: Hydrogen adsorption on the surface of metals, In: *Gaseous hydrogen embrittlement of materials in energy technologies*, Vol2 (2012) 3–26.

- [23] R.A. Oriani: The diffusion and trapping of hydrogen in steel, *Acta Metallurgica* 18 (1970) 147–157.
- [24] A. Pundt, R. Kirchheim: Hydrogen in metals: Microstructural Aspects, *Annu. Rev. Mater. Res.* 36 (2006) 555–608.
- [25] A. Turnbull: Hydrogen diffusion and trapping in metals, in: *Gaseous hydrogen embrittlement of materials in energy technologies Vol2* (2012) 89–128.
- [26] F.G. Wei, K. Tsuzaki: Hydrogen trapping phenomena in martensitic steels, In: *Gaseous hydrogen embrittlement of materials in energy technologies, Vol1* (2012) 493–525.
- [27] T. Zakroczymski: Electrochemical determination of hydrogen in metals, *Journal of Electroanalytical Chemistry* 475 (1999) 82–88.
- [28] J.S. Georgiev, L.A. Anestiev: Influence of the surface processes on the hydrogen permeation through ferritic steel and amorphous Fe₄₀Ni₄₀Mo₄B₁₆ alloy specimens, *Journal of Nuclear Materials* 249 (1997) 133–141.
- [29] P. Olsson, A. Delblanc Bauer, H. Eriksson: Duplex stainless steels, *Proc. of the 5th World Conference* (1997)
- [30] T. Boellinghaus, H. Hoffmeister: Numerical Model for Hydrogen-Assisted Cracking, *Corrosion* 56 (2000) 611–622.
- [31] L. Smith, M. Celant, A. Pourbaix: A guideline to the successful use of duplex stainless steels for flowlines, (2000)
- [32] S.P. Lynch: Metallographic and fractographic techniques for characterising and understanding hydrogen-assisted cracking of metals, In: *Gaseous HE of materials in energy technologies*, (2012), 329–339.
- [33] A.R. Troiano: The role of hydrogen and other interstitials in the mechanical behavior of metals, *Trans. ASM* (1960) 54–80.

-
- [34] R.A. Oriani: A mechanistic theory of hydrogen embrittlement of steels, *Ber. Bunsenges. Phys. Chem.* 76, (1972) 848-857
- [35] C.D. Beachem: A new model for hydrogen-assisted cracking, *Metall. Trans.* (1972) 437–451.
- [36] H.K. Birnbaum, P. Sofronis: Hydrogen-enhanced localized plasticity-a mechanism for hydrogen related fracture, *Materials Science and Engineering: A* (1994) 191–202.
- [37] P.J. Ferreira, I.M. Robertson, H.K. Birnbaum: Hydrogen effects on the interaction between dislocations, *Acta Materialia* 46 (1998) 1749–1757.
- [38] S.P. Lynch: Environmentally assisted cracking: Overview of evidence for an adsorption-induced localised-slip process, *Acta Metallurgica* 36 (1988) 2639–2661.
- [39] C. Bathias, L. Drouillac, P. Le François: How and why the fatigue S–N curve does not approach a horizontal asymptote, *International Journal of Fatigue* 23 (2001) 143–151.
- [40] K. Tokaji, T. Ogawa: The Growth Behaviour of Microstructurally Small Fatigue Cracks in Metals, *Short Fatigue Cracks*, ESIS 13(Edited by K.J. Miller and E.R. de los Rios) (1992) 85–99.
- [41] S. Suresh, R.O. Ritchie: Propagation of short fatigue cracks, *International Metals Reviews* 29 (1984) 445–475.
- [42] D. Kujawski, F. Ellyin: A microstructurally motivated model for short crack growth In Miller, K.J., de los Rios, E.R. (eds.): *Short fatigue crack growth*, ESIS 13. Mechanical Engineering Publications, London, (1992), S. 391-405.
- [43] H.A. Richard, M. Sander: *Ermüdungsrisse: Erkennen, sicher beurteilen, vermeiden*, 2nd ed., Vieweg+Teubner Verlag, Wiesbaden, (2012)

- [44] T. Kanezaki, C. Narazaki, Y. Mine, S. Matsuoka, Y. Murakami: Effects of hydrogen on fatigue crack growth behavior of austenitic stainless steels, *International Journal of Hydrogen Energy* 33 (2008) 2604–2619.
- [45] Y. Murakami, T. Kanezaki, Y. Mine, S. Matsuoka: Hydrogen Embrittlement Mechanism in Fatigue of Austenitic Stainless Steels, *Metall and Mat Trans A* 39 (2008) 1327–1339.
- [46] S. Matsuoka, H. Tanaka, N. Homma, Y. Murakami: Influence of hydrogen and frequency on fatigue crack growth behavior of Cr-Mo steel, *Int J Fract* 168 (2011) 101–112.
- [47] Y. Ogawa, S. Okazaki, O. Takakuwa, H. Matsunaga: The roles of internal and external hydrogen in the deformation and fracture processes at the fatigue crack tip zone of metastable austenitic stainless steels, *Scripta Materialia* 157 (2018) 95–99
- [48] Y. Oda, H. Noguchi: Observation of hydrogen effects on fatigue crack growth behaviour in an 18Cr-8Ni austenitic stainless steel, *Int J Fract* 132 (2005) 99–113.
- [49] Y. Aoki, K. Kawamoto, Y. Oda, H. Noguchi, K. Higashida: Fatigue characteristics of a type 304 austenitic stainless steel in hydrogen gas environment, *Int J Fract* 133 (2005) 277–288.
- [50] Y. Ogawa, H. Matsunaga, J. Yamabe, M. Yoshikawa, S. Matsuoka: Fatigue limit of carbon and Cr Mo steels as a small fatigue crack threshold in high-pressure hydrogen gas, *International Journal of Hydrogen Energy* 43 (2018) 20133–20142.
- [51] J.I. Shakib, H. Ullmaier, E.A. Little, R.G. Faulkner, W. Schmitz, T.E. Chung: PII: 0022-3115(94)90126-0, *Journal of Nuclear Materials* (1994) 579–583.
- [52] T. Ohmura, A.M. Minor, E.A. Stach, J.W. Morris: Dislocation–grain boundary interactions in martensitic steel observed through in situ nanoindentation in a transmission electron microscope, *Journal of Materials Research* 19 (2004) 3626–3632

-
- [53] T. P. Perng, C. J. Altstetter: Comparison of hydrogen gas embrittlement of austenitic and ferritic stainless steels, *Metall Mater Trans A* 18 (1987) 123–134.
- [54] P. Deimel, H. Leonhard, E. Sattler: Characterization of the influence of high-pressure hydrogen gas on the ductility of the steel 15 MnNi 6 3, *International Journal of Hydrogen Energy* 18 (1993) 313–318.
- [55] ASTM, Standard Test Method for Measurement of Fracture Toughness (E1820-18a).
- [56] K.A. Nibur, P.J. Gibbs, J.W. Foulk, C. San Marchi: Notched Fatigue of Austenitic Alloys in Gaseous Hydrogen, in: X.-K. Zhu, M. Brongers, H. Qian (Eds.), *Proceedings of the ASME Pressure Vessels and Piping Conference - 2017: Presented at the ASME 2017 Pressure Vessels and Piping Conference, July 16-20 (2017) Waikoloa, Hawaii, USA, The American Society of Mechanical Engineers, New York, N.Y., 2017.*
- [57] P. Deimel, E. Sattler: Untersuchungen zum Wasserstoffeinfluss auf im Kompressorbau eingesetzte Werkstoffe, *FKM* (2007).
- [58] J.W. Pegues, M.D. Roach, N. Shamsaei: Influence of microstructure on fatigue crack nucleation and microstructurally short crack growth of an austenitic stainless steel, *Materials Science and Engineering: A* 707 (2017) 657–667.
- [59] M.D. Roach, S.I. Wright: Investigations of twin boundary fatigue cracking in nickel and nitrogen-stabilized cold-worked austenitic stainless steels, *Materials Science and Engineering: A* 607 (2014) 611–620.
- [60] S.I. Wright, D.P. Field: Recent studies of local texture and its influence on failure, *Materials Science and Engineering: A* (1998) 165–170.
- [61] C. San Marchi, T. Michler, K.A. Nibur, B.P. Somerday: On the physical differences between tensile testing of type 304 and 316 austenitic stainless steels with

- internal hydrogen and in external hydrogen, *International Journal of Hydrogen Energy* 35 (2010) 9736–9745.
- [62] M. Schwarz, E. Sattler, S. Zickler, S. Weihe: Tensile and Fatigue Behaviour of an austenitic stainless CrNi steel in 10 MPa hydrogen gas atmosphere, *ASME PVP Proc, Waikoloa* (2017) 65988.
- [63] T. Michler, C. San Marchi, J. Naumann, S. Weber, M. Martin: Hydrogen environment embrittlement of stable austenitic steels, *International Journal of Hydrogen Energy* 37 (2012) 16231–16246.
- [64] T. Michler, J. Naumann: Hydrogen environment embrittlement of austenitic stainless steels at low temperatures, *International Journal of Hydrogen Energy* 33 (2008) 2111–2122.
- [65] S. Ueki, Y. Mine, K. Takashima: Crystallographic study of hydrogen-induced twin boundary separation in type 304 stainless steel under cyclic loading, *Corrosion Science* 129 (2017) 205–213.
- [66] Y. Bai, Y. Momotani, M.C. Chen, A. Shibata, N. Tsuji: Effect of grain refinement on hydrogen embrittlement behaviors of high-Mn TWIP steel, *Materials Science and Engineering: A* (2016) 935–944.
- [67] A. Oudriss, J. Creus, J. Bouhattate, C. Savall, B. Peraudeau, X. Feaugas: The diffusion and trapping of hydrogen along the grain boundaries in polycrystalline nickel, *Scripta Materialia* 66 (2012) 37–40.
- [68] A.-M. Brass, J. Chêne: Hydrogen uptake in 316L stainless steel: Consequences on the tensile properties, *Corrosion Science* 48 (2006) 3222–3242.
- [69] D. Di Stefano, M. Mrovec, C. Elsässer: First-principles investigation of hydrogen trapping and diffusion at grain boundaries in nickel, *Acta Materialia* 98 (2015) 306–312.

-
- [70] J. Chen, A.M. Dongare: Role of grain boundary character on oxygen and hydrogen segregation-induced embrittlement in polycrystalline Ni, *J Mater Sci* 52 (2017) 30–45.
- [71] J.E. Angelo, N.R. Moody, M.I. Baskes: Trapping of hydrogen to lattice defects in nickel, *Modelling Simul. Mater. Sci. Eng.* (1995) 289.
- [72] Z.X. Ma, X.L. Xiong, L.N. Zhang, Z.H. Zhang, Y. Yan, Y.J. Su: Experimental study on the diffusion of hydrogen along individual grain boundaries in nickel, *Electrochemistry Communications* (2018) 24–28.
- [73] E.A. West, G.S. Was: A model for the normal stress dependence of intergranular cracking of irradiated 316L stainless steel in supercritical water, *Journal of Nuclear Materials* 408 (2011) 142–152.
- [74] E.A. West, G.S. Was: Strain incompatibilities and their role in intergranular cracking of irradiated 316L stainless steel, *Journal of Nuclear Materials* 441 (2013) 623–632.
- [75] I. Roth, M. Kübbeler, U. Krupp, H.-J. Christ, C.-P. Fritzen: Crack initiation and short crack growth in metastable austenitic stainless steel in the high cycle fatigue regime, *Procedia Engineering* 2 (2010) 941–948.
- [76] Z. Hua, D. Wang, Z. Liu, Y. Zhang, S. Zhu: Hydrogen distribution at twin boundary in austenitic stainless steel studied by scanning Kelvin probe force microscopy, *Materials Letters* 234 (2019) 175–178.
- [77] A.S. Tetelman, A.J. McEvily: *Fracture of Structural Marterials*, John Wiley & Sons, Inc., (1967)
- [78] A. Shibata, T. Nagoshi, M. Sone, Y. Higo: Micromechanical characterization of deformation behavior in ferrous lath martensite, *Journal of Alloys and Compounds* 577 (2013) S555-S558.

- [79] C. Du, J.P.M. Hoefnagels, R. Vaes, M.G.D. Geers: Plasticity of lath martensite by sliding of substructure boundaries, *Scripta Materialia* 120 (2016) 37–40.
- [80] L. Morsdorf, O. Jeannin, D. Barbier, M. Mitsuhashi, D. Raabe, C.C. Tasan: Multiple mechanisms of lath martensite plasticity, *Acta Materialia* 121 (2016) 202–214.
- [81] S. Ratanaphan, D.L. Olmsted, V.V. Bulatov, E.A. Holm, A.D. Rollett, G.S. Rohrer: Grain boundary energies in body-centered cubic metals, *Acta Materialia* 88 (2015) 346–354.
- [82] G.S. Rohrer: Grain boundary energy anisotropy: a review, *J Mater Sci* 46 (2011) 5881–5895.
- [83] G.S. Rohrer: Measuring and Interpreting the Structure of Grain-Boundary Networks, *Journal of the American Ceramic Society* 94 (2011) 633–646.
- [84] A. Nagao, M. Dadfarnia, B.P. Somerday, P. Sofronis, R.O. Ritchie: Hydrogen-enhanced-plasticity mediated decohesion for hydrogen-induced intergranular and “quasi-cleavage” fracture of lath martensitic steels, *Journal of the Mechanics and Physics of Solids* 112 (2018) 403–430.
- [85] L. Cho, P.E. Bradley, D.S. Lauria, M.L. Martin, M.J. Connolly, J.T. Benzing, E.J. Seo et al.: Characteristics and mechanisms of hydrogen-induced quasi-cleavage fracture of lath martensitic steel, *Acta Materialia* 206 (2021) 116635.
- [86] R. Singh, V. Singh, A. Arora, D.K. Mahajan: In-situ investigations of hydrogen influenced crack initiation and propagation under tensile and low cycle fatigue loadings in RPV steel, *Journal of Nuclear Materials* 529 (2020) 151912.
- [87] K. Takai, N. Abe: Identification of hydrogen desorption peak temperatures, binding energies, and occupation ratios at vacancies, dislocations and grain boundaries in iron and steel (2013) 29–36.
- [88] C.M. Sturges, A.P. Miodownik: The interaction of hydrogen and dislocations in iron, *Acta Metallurgica* (1969) 1197–1207.

-
- [89] J.P. Hirth: Effects of hydrogen on the properties of iron and steel, *Metall. Trans. A* (1980) 1501–1511.
- [90] P. Novak, R. Yuan, B.P. Somerday, P. Sofronis, R.O. Ritchie: A statistical, physical-based, micro-mechanical model of hydrogen-induced intergranular fracture in steel, *Journal of the Mechanics and Physics of Solids* 58 (2010) 206–226.
- [91] W.Y. Choo, J.Y. Lee: Thermal analysis of trapped hydrogen in pure iron, *Metallurgical Transactions A* (1982) 135–140.
- [92] N. Ishikawa, H. Sueyoshi, A. Nagao: Hydrogen Microprint Analysis on the Effect of Dislocations on Grain Boundary Hydrogen Distribution in Steels, *ISIJ International* 56 (2016) 413–417.
- [93] T. Furuhashi, K. Kikumoto, H. Saito, T. Sekine, T. Ogawa, S. Morito, T. Maki: Phase Transformation from Fine-grained Austenite, *ISIJ Int.* (2008) 1038–1045.
- [94] T. Hanamura, S. Torizuka, S. Tamura, S. Enokida, H. Takechi: Effect of Austenite Grain Size on Transformation Behavior, Microstructure and Mechanical Properties of 0.1C–5Mn Martensitic Steel, *ISIJ Int.* 53 (2013) 2218–2225.
- [95] W. Hui: Microstructure Refining and Strengthening of Martensitic Steel, in: Y. Weng (Ed.), *Ultra-fine grained steels*, Metallurgical Industry Press, Beijing, (2010) pp. 300–349.
- [96] J.W. Morris Jr.: Comments on the Microstructure and Properties of Ultrafine Grained Steel, *ISIJ Int.* (2008) 1063–1070.
- [97] E.O. Hall: *Proc. Phys. Soc.* vol. 643, p. 747 (1951).
- [98] N.J. Petch: *J. Iron Steel Inst.* vol.173, p.25 (1953).

Curriculum vitae

Martina Manuela Schwarz
 Imkerstr. 7
 70439 Stuttgart
 Staatsangehörigkeit: deutsch
 Geb: 28.01.1989

Since 01.12.2014	Junior Researcher, Materials Testing Institute University of Stuttgart
------------------	--

Research stay Sandia National Laboratories, Livermore, USA
 (01.07. – 31.10.2019)

01.10.2012 26.08.2014	Master of Science Mechanical Engineering, University of Stuttgart
--------------------------	---

Master's thesis: „Development of a model describing the cyclic impact wear of a flow control valve in a petrol injection system” at Robert Bosch GmbH (01.03. – 26.08.2014)

Internship, Walter AG, Tübingen, R&D PVD Coatings (01.09. – 31.12.2013)

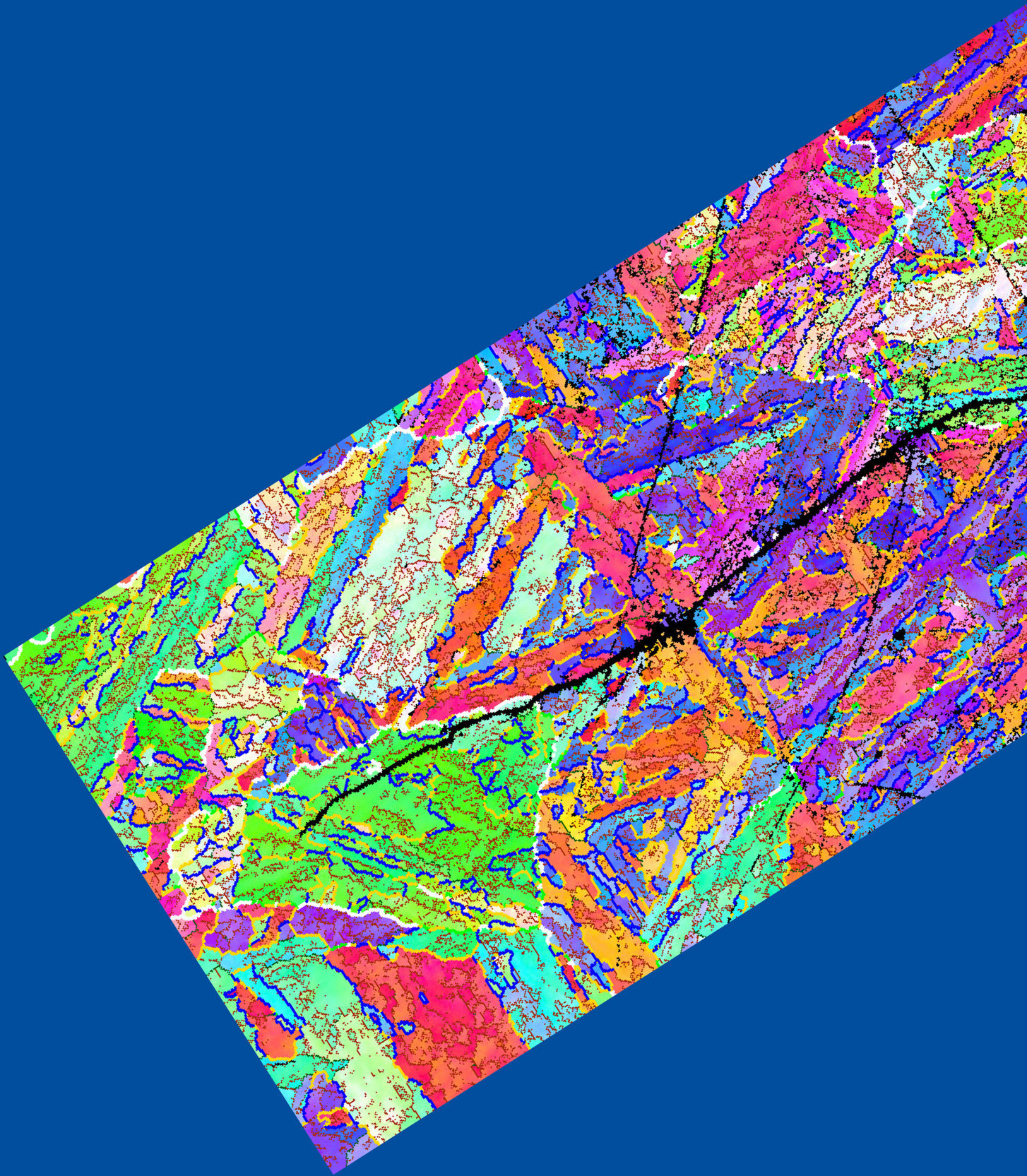
Student Employee at Institute for Materials Testing, Material Science and Strength of Materials (IMWF), University of Stuttgart, Molecular dynamic-Simulations (01.08.2012 – 31.07.2013)

01.10.2008 25.09.2012	Bachelor of Science Mechanical Engineering, University of Stuttgart
--------------------------	---

Bachelor's thesis: “Monte-Carlo and Molecular Dynamics Simulations on the Anisotropic Tensile Behavior in the -Fe/Cu/Ni-System at Different States of Thermal Ageing”

Semester abroad, NTNU, Trondheim, Norway (01.08. – 21.12.2011)

01.09.1999 23.06.2008	Eschbachgymnasium, Stuttgart-Freiberg Degree: Allgemeine Hochschulreife
--------------------------	--



Universität Stuttgart

ISBN: 978-3-946789-11-6